

THE INFLUENCE OF MICROSTRUCTURE ON STRESS
CORROSION CRACKING OF MILD STEEL IN SYNTHETIC
CAUSTIC-NITRATE NUCLEAR WASTE SOLUTION

A THESIS

Presented to

The Faculty of the Division of Graduate
Studies and Research

By

Peter Gregory Sarafian

In Partial Fulfillment

of the Requirements for the Degree

Doctor of Philosophy in the School of Nuclear Engineering

Georgia Institute of Technology

December 1975

22-a
D-254

THE INFLUENCE OF MICROSTRUCTURE ON STRESS
CORROSION CRACKING OF MILD STEEL IN SYNTHETIC
CAUSTIC-NITRATE NUCLEAR WASTE SOLUTION

Approved:

G. G. Eichholz, Chairman

M. R. Louthan, Jr.

J. A. Donovan

M. V. Davis

R. F. Hochman

Date approved by Chairman: 12/12/75

DEDICATION

To Anne

ACKNOWLEDGEMENTS

This paper was prepared while the author was a recipient of a Graduate Laboratory Participation Grant administered by Oak Ridge Associated Universities under Contract No. AT(07-2)-1 with the U. S. Energy Research and Development Administration at the Savannah River Laboratory, Aiken, SC, operated by E. I. du Pont de Nemours & Co. By acceptance of this paper, the publisher and/or recipient acknowledges the U. S. Government's right to retain a nonexclusive, royalty-free license in and to any copyright covering this paper, along with the right to reproduce and to authorize others to reproduce all or part of the copyrighted paper.

The author expresses his sincere gratitude to his thesis advisor, Dr. G. G. Eichholz, for his encouragement, patience and assistance in the course of this effort. He also thanks Drs. M. V. Davis, J. A. Donovan, R. F. Hochman and M. R. Louthan, Jr. for reviewing the work.

The author gratefully acknowledges the assistance of Drs. M. R. Louthan, Jr. and J. A. Donovan and their continuing interest and many helpful discussions during the experimental program at Savannah River Laboratory. Special appreciation is expressed to the entire staff of the E. I. du Pont de Nemours & Co., Savannah River Laboratory, Aiken, SC, for their aid, cooperation and gracious hospitality.

Last, the author thanks all the many friends and relatives who shared the difficulties and helped to lighten the burden, especially Andrea and Andrew and most of all Anne.

LIST OF TABLES

Table	Page
1. ASTM Specification A 516 Grade 70 (Reference 129). . . .	178
2. Bethlehem Steel Corp. Test and Analysis of A 516 Grade 70.	179
3. Heat Treatment Schedule.	180
4. Composition of H-Area Purex Waste (Reference 5).	181
5. Tensile Properties of A 516 Grade 70 at 370°K, $\dot{\epsilon}_0 = 8.3 \times 10^{-5} \text{s}^{-1}$	182, 183
6. Tensile Properties of A 516 Grade 70 at 370°K, $\dot{\epsilon}_0 = 8.3 \times 10^{-6} \text{s}^{-1}$	184, 185
7. Temperature Dependence of Tensile Properties of A 516 Grade 70 at $\dot{\epsilon}_0 = 8.3 \times 10^{-6} \text{s}^{-1}$	186, 187
8. CT Specimen SCC Properties in H-Purex at 370°K, $K_I = 49.4 \text{ MPa(m)}^{1/2}$	188
9. Powder X-ray Diffraction of SCC Surface Oxides.	189
10. CT Specimen SCC Properties in 5M NaNO ₃ at pH 6.0, 370°K, $K_I = 49.4 \text{ MPa(m)}^{1/2}$, TL Orientation.	190
11. K_{SCC} of WOL Specimens in 5M NaNO ₃ at pH 6.0 and pH 13.7, 368°K.	191
12. K_{SCC} of WOL Specimens in 5M NaNO ₃ at pH 6.0, 368°K. . .	192

LIST OF ILLUSTRATIONS

Figure	Page
1. Polarization Diagram for Typical Passivating Metal.	10
2. Dependence of Stress Corrosion Crack Velocity on Stress Intensity Factor and Nitrate Concentration.	17
3. Effect of Additives on Corrosion and Cracking.	29
4. Conditions for Metastable Passivity.	32
5. Transverse Section of Test Weld Showing Thermal Effects. . .	51
6. Upper Weld Bead (Top, Central Region of Figure 5).	51
7. Massive Grains (Adjacent to Weld Bead in Figure 5).	52
8. Intermediate Grain Size (Between Weld Bead and Light Band Across Plates in Figure 5).	52
9. Refined Grains (Light Band Across Plates in Figure 5). . . .	53
10. Feathery Pearlite (Dark Band Across Plates in Figure 5). . .	53
11. Unaffected Base Metal of Unknown Heat (Welded Plates in Figure 5).	55
12. Heat 518X0796; Hot-Rolled Condition.	55
13. Heat 518X0796; Normalized Condition.	57
14. Heat 518X0796; Quenched Condition.	57
15. Heat 518X0796; Quenched Condition.	58
16. Heat 518X0796; Quenched Condition.	58
17. Heat 518X0796; Spheroidized Condition.	59
18. Heat 518X0796; Spheroidized Condition.	59
19. Heat 518X0796; Spheroidized Condition.	61
20. Heat 518X0796; Hot Rolled and Spheroidized Condition. . . .	61
21. Heat 518X0796; Normalized and Spheroidized Condition. . . .	62

LIST OF ILLUSTRATIONS (Continued)

Figure	Page
22. Heat 518X0796; Quenched and Spheroidized Conditions.	62
23. Grain Size of Heat 518X0796; Polarized Light, Dark Field Contrast.	64
24. ASTM Crack Plane Orientation Code for Rolled Plate (Reference 130).	64
25. Round Bar Tensile Specimen.	65
26. Compact Tensile Specimen.	68
27. Constant Load Creep Testing Machine Used for Stress Corrosion Studies.	71
28. Constant Load Test Cell and Controls.	72
29. Wedge Opening Loaded Specimen (Reference 131).	75
30. Pyrex Reaction Kettle with Flanged Lid.	79
31. Temperature Regulated Oil Baths.	79
32. Electrochemical Polarization Test Cell (Reference 135). . .	81
33. Polarization Experiment Schematic Diagram.	82
34. Representative Engineering Stress-Strain Curves at 370°K, $\dot{\epsilon}_0 = 8.3 \times 10^{-5} \text{s}^{-1}$	86
35. Representative True Stress-True Strain Curves at 370°K, $\dot{\epsilon}_0 = 8.3 \times 10^{-5} \text{s}^{-1}$	87
36. Portion of Log True Stress-Log True Strain Curves at 370°K, $\dot{\epsilon}_0 = 8.3 \times 10^{-5} \text{s}^{-1}$	88
37. Representative Engineering Stress-Strain Curves at 370°K, $\dot{\epsilon}_0 = 8.3 \times 10^{-6} \text{s}^{-1}$	89
38. Portion of Log True Stress-Log True Strain Curves at 370°K, $\dot{\epsilon}_0 = 8.3 \times 10^{-6} \text{s}^{-1}$	90
39. Engineering Stress-Strain Curves for Hot-Rolled Steel at $\dot{\epsilon}_0 = 8.3 \times 10^{-6} \text{s}^{-1}$, Various Temperatures.	91
40. Portion of Log True Stress-Log True Strain Curves at $\dot{\epsilon}_0 = 8.3 \times 10^{-6} \text{s}^{-1}$, Various Temperatures.	92

LIST OF ILLUSTRATIONS (Continued)

Figure	Page
41. Fracture Surface of HR Tensile Specimen.	96
42. Fracture Surface of S Tensile Specimen.	96
43. Crack Opening Displacement of CT Specimens in H-Purex at 370°K, $K_{I1}=49.4 \text{ MPa(m)}^{1/2}$	97
44. Time to Failure of CT Specimens in H-Purex at 370°K, $K_{I1}=49.4 \text{ MPa(m)}^{1/2}$	99
45. Crack Branching in CT Specimen.	101
46. Fracture Surface of CT Specimen Showing Various Regions (Right to Left): Fatigue, SCC, Ductile Overload, SCC Reinitiation, Air Fracture.	102
47. Closeup of CT Specimen SCC Fracture Surface.	102
48. SCC Fracture Surface Obscured by Film.	104
49. Film-Free, IG SCC Region Near Crack Tip.	104
50. SCC Surface of Q Microstructure After Descaling.	106
51. SCC Surface of HR Microstructure After Descaling.	106
52. SCC Surface of N Microstructure After Descaling.	107
53. SCC Surface of S Microstructure After Descaling.	107
54. Pitting on Descaled SCC Fracture Surface.	108
55. Cracks in Ferrite Grain Boundaries in HR Structure.	109
56. Cracks Outlining Pearlite Colonies in HR Structure.	109
57. Crack Velocity of CT Specimens in H-Purex at 370°K, $K_{I1}=49.4 \text{ MPa(m)}^{1/2}$	112
58. Calculated Crack Growth of CT Specimens in H-Purex at 370°K, $K_{I1}=49.4 \text{ MPa(m)}^{1/2}$	114
59. Crack Opening Displacement of CT Specimens in 5M NaNO ₃ at pH 6.0, 370°K, $K_{I1}=49.4 \text{ MPa(m)}^{1/2}$	116

LIST OF ILLUSTRATIONS (Continued)

Figure	Page
60. Time to Failure of CT Specimens in 5M NaNO ₃ at pH 6.0, 370°K, $K_I=49.4 \text{ MPa(m)}^{1/2}$	117
61. Crystalline Oxide on SCC Reinitiation Surface in 5M NaNO ₃ , pH 6.0.	119
62. Average Crack Velocity of CT Specimens in 5M NaNO ₃ at pH 6.0, 370°K, $K_I=49.4 \text{ MPa(m)}^{1/2}$	120
63. K_{SCC} of WOL Specimens in 5M NaNO ₃ at pH 6.0 and pH 13.7, 368°K.	123
64. K_{SCC} of WOL Specimens in 5M NaNO ₃ at pH 6.0, 368°K.	125
65. Fracture Surface of WOL Specimen.	127
66. Closeup of Chevron-Like Markings on SCC Fracture Surface.	127
67. Dependence of Crack Velocity Upon pH in 5M NaNO ₃ 368°K.	129
68. Crack Velocities of SCC Specimens in 5M NaNO ₃ at pH 6.0, 368°-370°K.	130
69. Crack Velocities of Hot-Rolled Steel in 5M NaNO ₃ at pH 6.0, Various Temperatures.	132
70. Oxide Pattern on HR Corrosion Coupon.	134
71. Pitting and IG Attack on Corrosion Coupon.	134
72. Polarization Curves in 5M NaNO ₃ at pH 3.5, 370°K.	136
73. Polarization Curves in 5M NaNO ₃ at pH 6.0, 370°K.	138
74. Polarization Curves in 5M NaNO ₃ at pH 13.7, 370°K.	140

ABSTRACT

The influence of alloy microstructure on stress corrosion cracking of mild steel in caustic-nitrate synthetic nuclear waste solutions was studied. An evaluation was made of the effect of heat treatment on a representative material (ASTM A 516 Grade 70) used in the construction of high activity radioactive waste storage tanks at Savannah River Plant. Several different microstructures were tested for susceptibility to stress corrosion cracking. Precracked fracture specimens loaded in either constant load or constant crack opening displacement were exposed to a variety of caustic-nitrate and nitrate solutions. Results were correlated with the mechanical and corrosion properties of the microstructures.

Crack velocity and crack arrest stress intensity were found to be related to the yield strength of the steel microstructures. Fractographic evidence indicated pH depletion and corrosive crack tip chemistry conditions even in highly caustic solutions. Experimental results were compatible with crack growth by a strain-assisted anodic dissolution mechanism, however hydrogen embrittlement also was considered possible.

TABLE OF CONTENTS

	Page
ACKNOWLEDGEMENTS	iii
LIST OF TABLES	iv
LIST OF ILLUSTRATIONS.	v
ABSTRACT	ix
 Chapter	
I. INTRODUCTION.	1
Background	
Literature Review	
Discussion of Cracking Mechanisms	
Summary	
II. MATERIALS, EQUIPMENT AND EXPERIMENTAL PROCEDURE	48
Experimental Program	
Test Material and Heat Treatment	
Tensile Tests in Air	
Stress Corrosion Cracking Experiments	
Corrosion Experiments	
III. EXPERIMENTAL RESULTS.	85
Tensile Tests in Air	
Stress Corrosion Cracking Experiments	
Corrosion Experiments	
Summary of Results	
IV. DISCUSSION OF RESULTS	145
Cracking in Nitrate and Caustic-Nitrate Solutions	
A Mechanism of Caustic-Nitrate Cracking of Steel	
V. CONCLUSIONS	174
VI. RECOMMENDATIONS	175
APPENDIX A. TABLES.	177
B. GLOSSARY OF TERMS AND ABBREVIATIONS	193

TABLE OF CONTENTS (Continued)

BIBLIOGRAPHY	Page 194
VITA	203

CHAPTER I

INTRODUCTION

Background

Certain radiosotopes produced as byproducts of the nuclear fuel cycle remain radioactive for centuries and require long term storage. In the past, much of the high-level radioactivity nuclear wastes have been stored in the form of neutralized (alkaline) nitric acid solutions and sludges in steel tanks. The tank storage method has been used for interim containment of wastes pending decisions on long-term disposal techniques. Mild steels, such as those used in the fabrication of nuclear waste storage tanks, are susceptible to environmentally induced cracking, commonly known as stress corrosion cracking (SCC), in the presence of either nitrate ion or hydroxide ion. Investigations indicated that cracks in waste tanks located at the ERDA Savannah River Plant were caused by SCC.¹ A leak was reported from waste storage tanks at the ERDA Hanford Plant;² this leak most likely resulted from SCC.

Stress corrosion cracking has been defined as the "rupture of metal, taking the form of cracks, that may occur under the conjoint influence of a corrosive environment and applied or residual [tensile] stresses."³ Stress corrosion cracks typically propagate normal to the principal tensile axis in uniaxial loading, and propagate either across individual metal grains as transgranular stress corrosion cracking (TG SCC) or between the grains as intergranular stress corrosion

cracking (IG SCC), depending upon the alloy and environment involved. In certain cases a transition between the two crack paths is developed by varying conditions of stress,⁴ strain rate,⁵ solution pH or alloy composition.⁶ Many engineering structures are constructed of alloys which are susceptible to SCC in certain media. Carbon and alloy steels, stainless steels, brass, aluminum, nickel and titanium alloys all crack in a variety of media, often at tensile stresses well below yield. In many cases the environments which cause SCC seem relatively noncorrosive to the alloy. Unpredictable failures continue to add to the ever-increasing list of SCC-causing environments. Alloys once thought to be immune to SCC have failed after years of use.

SCC was shown to cause cracking of waste storage tanks at the Savannah River Plant, Aiken, S. C. With the aid of remote observation and removal of sections of a waste tank wall, cracks were analyzed by Savannah River Laboratory.¹ Most cracks originated in the heat affected zone of welds and propagated into the ASTM A 285 Grade B steel plates, from which the tanks were fabricated. Cracks were up to several centimeters in length and extended intergranularly in a direction generally perpendicular to the welds. This direction was also perpendicular to the maximum residual tensile stress induced by welding during fabrication. The longitudinal welding stress may have exceeded the material's yield point near the weld centerline, and a large tensile stress probably extended into the heat affected zone.⁷ Numerous superficial cracks of 1 to 25 mm length also were found near welds on the inner tank surface which contacted the caustic-nitrate waste solution. This indicated crack initiation at the inner surface in heat affected zones.¹ The inner surface of

the examined tanks revealed little general corrosion but some shallow pitting. At least one crack was found to originate at an arc strike, a site of expected high residual stress. Studies also indicated that waste storage tank cracking was not directly related to radiation effects since cracking could be produced in nonradioactive synthetic waste solutions.⁸

Savannah River Plant high activity waste solutions have been stored as concentrated nitrate salts at high pH.⁹ Some of the waste materials precipitate from solution as a sludge. Operating conditions during service in cracked tanks consisted of a maximum sludge temperature of 215°C, a maximum supernate temperature of 52°C, and an average solution pH of 14. In such solutions and in synthetic waste solutions mild steel electrodes have open circuit surface potentials in the range generally observed for nitrate SCC.⁹ Since caustic embrittlement occurs at much lower potentials than does nitrate cracking, hydroxide ion is not considered the primary cracking agent in waste tank cracking.

The studies at Savannah River Laboratory concluded that nitrate SCC was the major cause of cracks in the mild steel storage tanks.^{1,9} Stress relief heat treatment to 1100°F was effective in preventing crack growth in test specimens,⁸ and stress relief was used in subsequent tank construction. To date, none of the heat-treated tanks has developed leaks. While the problem was alleviated, a degree of uncertainty involving SCC occurrences remains. Further studies were initiated to determine the influence of heat treatment and the resulting microstructures on the susceptibility of mild steel to SCC in synthetic nuclear waste solution. These studies constituted the work presented in this thesis.

Literature Review

Intergranular stress corrosion of mild steels has been noted and studied for over fifty years.^{10,11} Cracking was observed in a variety of liquid and gaseous media including: alkaline boiler water or concentrated hydroxide solutions,^{11,12} concentrated nitrate solutions,¹³ sulfides,¹⁴ cyanides,¹⁵ hydrocarbons,¹⁶ and coal gas liquor.¹⁷ This resulted in failures of steam boilers,¹⁸ fertilizer plants,¹⁹ bridges,²⁰ and petroleum distillation equipment.¹⁷ Mild steels are found to crack in an ever-increasing number of media,²¹ and emphasis is no longer placed on the specific natures of environments which cause cracking. Even seemingly innocuous, nonaggressive solutions of ammonium carbonate may crack mild steel under controlled electrochemical potential conditions.²¹

No universally accepted theory exists for the mechanism of SCC of mild steel in concentrated nitrate or caustic solutions. Indeed, there is little agreement on the reason why any specific alloy-environment combination causes SCC, and some investigators are unwilling to include IG cracking as a true example of SCC.²² Such people prefer to call intergranular failures "stress-assisted corrosion" since a degree of intergranular penetration usually occurs in the absence of stress.²³ In addition, while some corrosion authorities, such as Uhlig, propose a single mechanism to explain all SCC,²³ Staehle and others consider each case as unique with different mechanisms operating.²² Fundamental differences of opinion prevail in the field.

Nearly all of the stress corrosion susceptibility data for carbon

steels or mild steels comes from tests that use smooth surfaced specimens. Most of the SCC susceptibilities are measured as total time to failure after application of tensile stress. Stress corrosion cracking is somewhat arbitrarily divided into the crack initiation stage and the crack propagation stage. Since crack initiation at a smooth surface is often the slower and more time-consuming stage of cracking, time to failure data (which do not differentiate the two stages of cracking) tend to reflect specimen surface properties and crack initiation processes.²²

Nitrate Cracking of Mild Steel

Influence of Environment. Carbon and alloy steels crack in a variety of nitrate salt solutions. Cracking occurs rapidly enough to be studied in the laboratory at concentrations above about 2N and temperatures approaching the boiling point (about 90°C).¹³ The time to failure at a given stress shortens with both increasing temperature and nitrate concentration.^{13,24} Gilchrist and Narayan, however, found that time to failure became independent of solution concentration above 0.25N in NH_4NO_3 , in apparent disagreement with the general trend.²⁵ Nitrate salts of the alkali metals Li, K and Na induce IG SCC of mild steels with relative severities that are in order of increasing electrochemical potential of the cation.¹³ Solutions of these salts are relatively noncorrosive and produce only thin oxide films. More acidic salts such as $\text{Fe}(\text{NO}_3)_3$ and NH_4NO_3 cause more pronounced general corrosion to take place. $\text{Fe}(\text{NO}_3)_3$ promotes rapid dissolution, while NH_4NO_3 produces a black, adherent oxide film and is apparently the most aggressive nitrate cracking agent. The aggressiveness of NH_4NO_3 solutions appears to be related to the pH, and pH adjustment by

addition of nitric acid to alkali metal nitrate solutions increases their aggressiveness. At equal pH values, the cracking severity in alkali metal nitrates is equivalent to the severity in ammonium nitrate.¹³

The addition of hydroxide ion generally seems to inhibit nitrate cracking. SCC in NH_4NO_3 solutions is strongly inhibited by increasing hydroxide ion concentration in solutions over pH 7. However in solutions of pH 3 to pH 7 there is less effect.²⁶ The amount of caustic which can be added to nitrate solutions to inhibit cracking is limited however, because caustic solutions by themselves cause IG SCC (caustic embrittlement) of mild steels. Caustic additions and high pH inhibit the cathodic reaction but accelerate the general corrosion rate in NH_4NO_3 solutions.²⁶ Szklarska-Smialowska attributed this acceleration to stifling of nitrate ion reduction to nitrite and also to complexing of iron with evolved ammonia.²⁶ The inhibiting effect of raising the pH of other nitrate solutions was ascribed to impeding of corrosion at anodic sites by precipitated hydroxides.²⁷ Since general corrosion in NH_4NO_3 increases with pH, such would not appear to be the case in NH_4NO_3 solutions. Although the pH at the tip of a stress corrosion crack is acidic in other aqueous solutions, such data are not available for nitrate cracking of mild steel. Nevertheless, the inhibiting effect of increased pH may be related to this feature. The anodic current density of strained steel electrodes increases rapidly following additions of nitric acid to relatively nontarnishing nitrate solutions.¹³ Similar jumps in current density are seen if acid additions are made to tarnishing NH_4NO_3 solutions

when no stress is applied to the electrode, and film breakdown was proposed as the cause.¹² Such effects indicate that acidic conditions favor rapid metal dissolution.

Various ions in nitrate solutions have a pronounced effect on the cracking of mild steel. Sulfide ion was found to be particularly damaging.^{25,28} Increasing the concentration of alkali metal nitrate salts was shown to lower the apparent threshold stress for cracking.¹³ Similarly, additions of oxidizing ions such as KMnO_4 and $\text{K}_2\text{Cr}_2\text{O}_7$ were deleterious in nitrate solutions.¹³ Smialowski and Ostrowska also found the presence of dissolved oxygen to be necessary for cracking,²⁹ while Hertzog and Portevin found no such dependence.³⁰ Manganous ion appears to change the nature of corrosion products formed in NaNO_3 solution and shortens time to failure.³¹ A compact, adherent film was formed in the presence of manganous ion,³¹ while little or no film was observed on specimens exposed to pure sodium nitrate solutions.^{13,31} Manganous ion was thought to shift the equilibrium corrosion potential to a region of passivity where the general corrosion is decreased, but SCC is enhanced.³¹ Although acidic conditions promote cracking, passivity also seems to promote cracking. This suggests that cracking may occur under conditions of localized acidity and rapid dissolution combined with overall passivating conditions.

Chloride is among the ions which inhibit SCC of mild steel. Additions of chloride to nitrate solutions lengthen time to failure, but not monotonically.³¹ Because the chloride ion promotes pitting and general corrosion of steel, this effect probably overshadows the beneficial effect on SCC at high chloride concentrations. In addition, certain

commercial corrosion inhibitors are particularly effective in reducing SCC in steels; among them are the organic inhibitors quebracho and valonea and also HPO_4^{-2} salts, H_2PO_4^- salts, HAsO_4^{-2} salts and many basic salts.^{24,28,32}

Nitrite ion is a well-known corrosion inhibitor for steel, however the influence of nitrite ion on nitrate cracking is not well understood. While the nitrite ion inhibits cracking in NH_4NO_3 environments,³³ additions of nitrite to NaNO_3 solutions accelerate cracking.¹³ It was shown while small nitrite ion additions reduced the overall corrosion rate in 50% boiling NH_4NO_3 , larger amounts increased the corrosion rate.²⁸

Solution temperature is an important environmental parameter that influences nitrate cracking of mild steels. Cracking in nitrates is accelerated by increasing temperature, following an Arrhenius relationship. Activation energy for cracking in aerated 5N NH_4NO_3 was found to be 42 kJ/mole (10 kcal/mole).²⁶ The activation energy for overall corrosion in deaerated 5N NH_4NO_3 was evaluated as 40 kJ/mole (9.6 kcal/mole), while for either air or hydrogen saturated solutions the corrosion activation energies in stirred and in unstirred situations were 21-25 kJ/mole (5 to 6 kcal/mole) and 42-46 kJ/mole (10 to 11 kcal/mole), respectively.³¹

While the apparent activation energy for cracking in ammonium nitrate seems to be the same as the activation energy for corrosion in an unstirred solution, this does not necessarily mean that the entire cracking process is controlled by corrosion in placid environments. The reported value for cracking experiments comes from smooth-surfaced

specimen tests and must reflect crack initiation at a smooth surface as well as propagation. Crack initiation might be controlled by corrosion and the formation of grain boundary trenches. Crack propagation could be controlled by a different mechanism, and the solution conditions at the crack tip surface will likely be affected somewhat by plastic straining.

The dependence of nitrate cracking on electrochemical surface potential and the relationship of this dependence to the passivation properties of steel is well established. In nitrate solutions a critical cutoff potential for SCC appears to exist. While at electrode potentials increasingly more anodic (positive) than the cutoff potential SCC occurs with decreasing time to failure, potentials more cathodic (negative) induce immunity. This points to the feasibility of cathodic protection as a means of alleviating nitrate cracking of steels. In a 60% $\text{Ca}(\text{NO}_3)_2$ - 3% NH_4NO_3 solution the critical cutoff potential is about -280 to -340 mV versus a standard calomel electrode (SCE).²⁴ The cutoff potential shows a temperature dependency, becoming more anodic with increasing temperature in the range 80° to 110°C.²⁴ Humphries and Parkins reported a cutoff potential of -740 mV (SCE) in boiling 4N NH_4NO_3 with a minimum time to failure occurring at +460 mV.³⁴ In boiling 4N NaNO_3 , however, a cutoff of -640 mV was observed with a minimum time to failure also at +460 mV. The potential at the minimum time to failure corresponds to a value just to the passive side of the steel's critical passivating potential (peak current density on the anodic polarization curve). Figure 1 shows a typical anodic polarization curve for a passivating metal. Potentials just above and below the

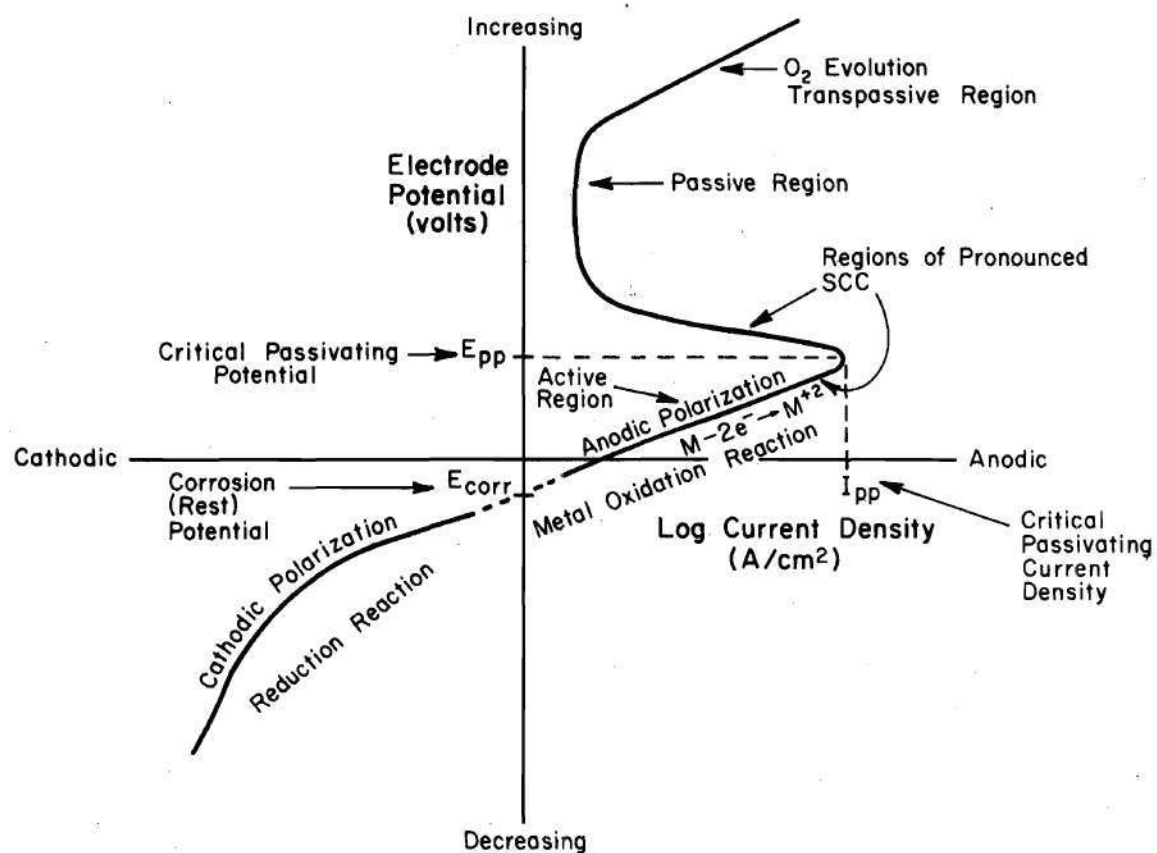


Figure 1. Polarization Diagram for Typical Passivating Metal.

critical passivating potential are often associated with pronounced incidence of SCC. Szklaraska-Smialowska found two minima in time to failure in an aerated 5N NH_4NO_3 solution: one at -390 mV and one at +60 to +460 mV.²⁶ The critical passivating potential in this case was at potentials somewhat more anodic or cathodic than this value, as expected. A cutoff potential was also observed at about -640 mV. At potentials more negative than this, failures occurred by general corrosion. The cathodic polarization curve in NH_4NO_3 solutions also showed a peak in current density thought to be associated with formation of a soluble ferrous-ammonia complex and hence with enhanced general corrosion.²⁶ However, electrodes previously passivated in nitric acid or in nitrite solution showed no such peak. The large increase in time to failure at the cutoff potential was attributed to reduction of nitrate ion to nitrite. The increase in general corrosion at more cathodic potentials was linked to ammonia evolved by nitrate ion reduction.²⁶ The cutoff potential also appears to be influenced by stress, being shifted to more negative values with increasing applied stress.³⁵

Passivity plays an important role in nitrate cracking. The relationship between passivation properties of steel in nitrate solutions and the dependence of nitrate cracking on surface potential confirms this importance. Since passivity is often associated with the formation of protective oxide films, oxides could be important in the nitrate cracking of steel. The electrochemical potential determines which oxides and/or soluble species develop during corrosion³⁶ and might influence whether general corrosion or SCC

becomes more probable. Humphries and Parkins found in 4N NH_4NO_3 solutions that magnetite (Fe_3O_4) formed on steel at the cathodic potentials which caused SCC, while nonprotective hematite ($\alpha\text{-Fe}_2\text{O}_3$) formed at the more anodic potentials.³⁴ At anodic potentials corresponding to minimum time to failure (+460 mV) hematite was the predominant oxide. Szklaraska-Smialowska also found magnetite at cathodic potentials near the critical cutoff potential in 5N NH_4NO_3 solution.²⁶ Flis verified the existence of magnetite at SCC potentials but found the hematite in 5N NH_4NO_3 solutions only at extremely anodic potentials.³⁷ Potential-pH conditions which favored cracking were found to correspond to regions of stability of Fe_2O_3 . Since magnetite was usually found instead, it was surmised that accumulation of carbon on corroding metal surfaces influenced the oxide phase, promoting formation of semiprotective magnetite rather than protective, passivating maghamite ($\gamma\text{-Fe}_2\text{O}_3$). It should be noted, however, that thermodynamic data for elevated temperatures are sparse, and a change of the stability regimes of various chemical species with temperature might be involved. Nevertheless, nitrate cracking of steel seems to be associated with semiprotective oxides and partial passivation.

The open circuit potential of specimens immersed in nitrate solution becomes more anodic (positive) with buildup of the oxide film. Application of stress reduces the extent of this polarization and causes the potential to be somewhat less anodic.³⁸ Notched tensile specimens were observed to undergo negative jumps in potential as large as 75 to 100 mV.³⁹ It was proposed that these jumps resulted

from strain and rupture of the oxide film. As mentioned previously such jumps in potential occur even in the absence of applied stress in NH_4NO_3 solution, indicating the nonprotective nature of films grown in such a medium. This may be related to the severity of SCC in NH_4NO_3 compared to other nitrates. The measurement of potential differences between filmed and unfilmed surfaces in 5% NH_4NO_3 showed the difference to be about 160 mV; it was thought that this would cause film-free metal to act as an anode and corrode preferentially. Such data support the well-known film rupture theory of SCC which views cracking process as localized dissolution at breaks in the corrosion product film.

Potential differences were measured between grain faces and grain boundaries in ferrous and nonferrous alloys.^{38,40} Such measurements support an electrochemical model of SCC and indicate preferential dissolution of active grain boundaries in the metal. Grain boundaries should be in a higher lattice energy state due to the local disorder and strain in the crystal structure and therefore at a more active potential than grain faces. Studies by Logan showed that the incidence of intergranular cracks in steel was related to the degree of crystallographic mismatch between adjoining metal grains.⁴¹ Maximum grain boundary surface energies should occur in a BCC alloy if the mismatch is between about 15 and 40 degrees.⁴² X-ray analysis of grains bordering intergranular cracks showed mismatches which ranged from 7 to 46 degrees with the majority lying between 10 to 30 degrees.⁴¹ These results indicate that nitrate cracking could be caused by preferential electrochemical dissolution of steel grain boundaries.

Various ferrite crystal planes exhibit different open circuit potentials and anodic polarization curves in ammonium nitrate solutions.⁴³ This indicates that certain crystal planes in iron will be preferentially corroded by nitrate solutions. It was suggested that this effect might be particularly important in crack initiation.⁴³ However, Logan found no evidence of preferential nitrate cracking in grain boundaries that border grains of a particular crystallographic orientation.⁴¹

Cementite precipitates (Fe_3C) may cause preferential grain boundary corrosion in steels. Cementite undergoes little cathodic polarization and is thus an efficient cathodic site.⁴⁴ Such sites would enhance the anodic dissolution of adjoining ferrite, and this principle is commonly used in the metallographic etching of two-phase alloys such as mild steels.

Influence of Stress/Strain. Tensile stress greatly accelerates intergranular corrosion penetration in mild steels in nitrate solutions and causes crack formation. The stress may either be externally applied stress or residual stress from heat treatment, welding or forming operations.^{8,45} Even stresses set up by differential contraction of adjacent phases in steels during solidification can induce stresses large enough to cause cracking. It was calculated that the tensile stress in the ferrite matrix surrounding a cementite precipitate may reach values up to 276 MPa (40,000 psi).⁴⁶ This approaches the yield point in mild steels, and was suggested as a possible reason for IG cracking of steel.²⁷

Elimination of residual (tensile) stresses by stress relieving heat treatment is effective in inhibiting cracking.^{19,47,48} Another

method of inhibition which is particularly effective in preventing surface initiation of cracks is the introduction of compressive stresses by shot peening or nitriding.²⁷

It is generally agreed that a certain degree of plastic deformation is necessary in order to obtain cracking in nitrate solutions.^{27,40} In general, time to failure increases rapidly with decreasing tensile stress.¹³ A threshold stress, below which cracking did not occur in a prolonged testing period, appeared to be below the yield point in low carbon steels¹³ but was well above the yield point in higher carbon steels.⁴⁹ An anomalous decrease in time to failure with decreasing tensile stress was found by Zabik between the yield point and elastic limit in 0.01% C steel.⁵⁰ No explanation was offered for the maximum in time to failure at a stress 10% higher than the elastic limit. The complicated effects of prestraining on nitrate cracking might be involved.

Increasing stress levels change crack morphology. Parkins and Usher demonstrated that at low stress levels and low nitrate concentrations only a few nonbranching cracks were formed. At high stress levels and at high nitrate concentrations numerous branching cracks were observed. Such behavior is seen in the cracking of other alloys under plane strain loading conditions.⁵¹

The stress state at the tip of a crack in an elastically loaded body is typically described by a scaling factor known as the stress intensity factor, K . This factor is proportional to the applied stress and to the square root of the crack length.

Under plane strain, crack opening load conditions the stress

intensity factor is denoted K_I .⁵¹ By use of precracked fracture specimens the stress corrosion crack velocity can be determined as a function of K_I .⁵¹ In many SCC systems the crack velocity decreases with decreasing K_I to a very small value that approaches zero crack growth rate (Figure 2). K_I at this apparent termination of cracking is called the threshold stress intensity for stress corrosion cracking or K_{ISCC} .⁵¹ Above K_{ISCC} the crack growth rate generally rises rapidly with increasing K_I . This region is called Stage I crack growth (Figure 2) and is characterized by a single, nonbranching crack.⁵¹ Crack velocity in Stage I cracking is so dependent upon stress intensity that only the longest crack (highest K_I) is favored for rapid growth. However at somewhat higher stress intensities, the crack velocity may become relatively independent of K_I . This region is called Stage II crack growth (Figure 2) and is characterized by many branching cracks.⁵¹ At yet higher stress intensities crack growth rate may increase with increasing K_I up to the onset of mechanical failure in so-called Stage III cracking (Figure 2).⁵¹

The relationship between crack velocity and K_I seems to describe the observations of Parkins and Usher.¹³ Non-branching cracks observed at low stress appear consistent with Stage I growth, and the branching cracks observed at high stress appear to be Stage II growth. The effects of nitrate concentration also may be explained. Since steel specimens demonstrate apparent Stage II cracking at high nitrate concentrations but Stage I cracking at low nitrate concentrations, the crack growth rate - K_I curve must be shifted to lower stress intensities (Figure 2). There is evidence that increasing nitrate concentration decreases K_{ISCC} .²⁷

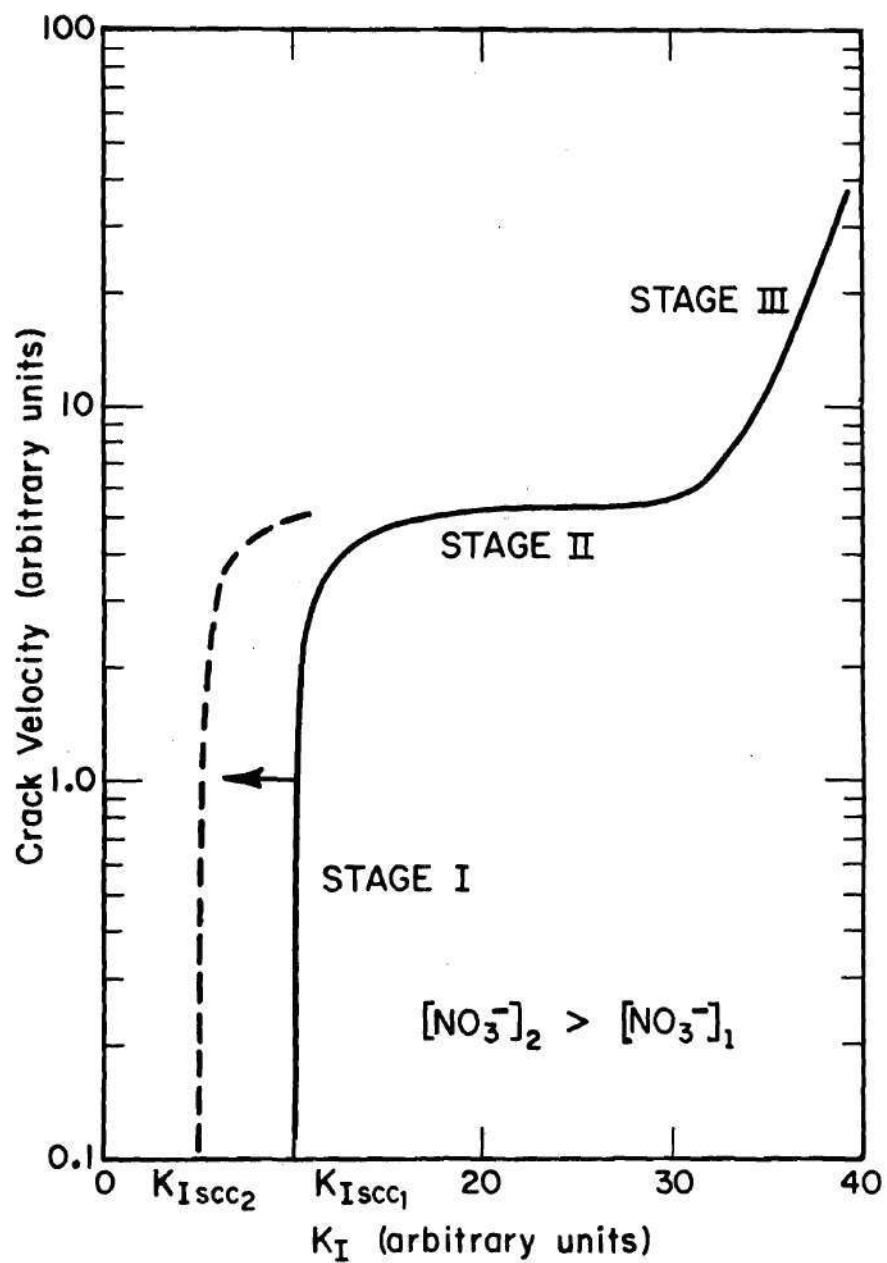


Figure 2. Dependence of Stress Corrosion Crack Velocity on Stress Intensity Factor and Nitrate Concentration.

Traditional time to failure data emphasize the slow, time-consuming crack initiation stage of the cracking process but do not differentiate between the two stages of SCC.²² Most smooth surfaced specimen tests reported in the literature are loaded to an initial stress intensity below K_{ISCC} . That is, no sharp cracks are deliberately introduced into the surface before testing, and the natural surface flaws are smaller than those required for a stress intensity larger than K_{ISCC} . Corrosion and grain boundary trenching (which are generally slow processes) will increase the surface flaw size to some critical depth during the crack initiation period.⁵¹ At this time the stress intensity reaches K_{ISCC} and crack propagation can proceed. Since smooth surfaced test specimens usually are of small cross section, cracking proceeds for a relatively short time before mechanical failure occurs. The importance of crack initiation stage in smooth specimen tests also is indicated by the effective inhibition of cracking by compressive surface stresses.

The effect of prior deformation on SCC in nitrate solutions is ambiguous. While prior straining in tension was shown to accentuate nitrate grain boundary attack of a polished steel surface,²⁷ other studies showed increased resistance to SCC after either cold rolling or prestraining in tension.^{49,53} However, there is renewed susceptibility to cracking when cold rolling is followed by prestraining in tension.^{49,52} Such effects appear to depend on the carbon content of the steel, and one explanation for such behavior was that deformation affected the amount of soluble carbon segregated at grain boundaries.⁵⁴ It was surmised that carbon-rich grain boundaries acted as cathodes which facilitated intergranular corrosion of the adjacent ferrite surfaces. This was

supported by electron microscopy and microhardness measurements. Deformation introduced many dislocations into the ferrite which were thought to redistribute interstitial atoms such as carbon during dislocation propagation.⁵⁴ Henthorne and Parkins were unable to correlate susceptibility to dislocation substructure, however corrosion attack on the walls of cracks seemed to correspond to dislocation tangle cell size.⁵⁵

Strain rate also affects the incidence of SCC. Henthorne and Parkins found that increasing strain rate increased the threshold stress at which a crack could be detected.⁵⁶ They correlated such an effect with the incubation time necessary after initial yielding for a deep crack to form which can then propagate rapidly. As mentioned before, straining electrodes are not anodically polarized to as great an extent as unstrained electrodes in nitrates.³⁸

Some investigators discuss the importance of the discontinuous manner in which tensile specimens yield in nitrate solutions. Discontinuous specimen elongation may be purely a reflection of the mechanical properties of the material rather than an indication of discontinuous corrosion attack. Flis and Scully demonstrated the same stress-strain behavior in specimens loaded in tension in both nitrate solution and liquid paraffin at the same temperature.⁵⁷ Henthorne and Parkins agreed with this interpretation of discontinuous yielding, and showed that the electrode potential jumps during SCC testing commenced at the material's upper yield point and were more pronounced in constant load (increasing stress) tensile tests than in constant deflection (decreasing stress) tensile tests.⁴⁹ This indicates that strain is important in

causing changes in the electrochemical surface properties of a specimen. However, there is no evidence that discontinuous yielding is particularly important in nitrate cracking.

Influence of Metallurgical Properties. Carbon, the most significant alloying addition to iron, is extensively studied with regard to SCC in nitrates. Maximum susceptibility to SCC occurs with carbon contents on the order of 0.01 to 0.05%.^{32,37} Susceptibility to cracking decreases with both lower^{27,52,58} and higher carbon contents.⁵⁹ The maximum solubility of carbon in ferrite is at the eutectoid temperature (0.0294% at 723°C)⁶⁰ and therefore might be related to the carbon content that corresponds to maximum susceptibility. The mechanism by which carbon influences SCC has been the subject of much controversy. The effects of discrete cementite precipitate particles²⁷ and soluble interstitial atoms^{54,58,61,62} in grain boundaries were examined. While Parkins pointed out the possible influence of interface stresses around cementite precipitates,⁵² Uhlig and others mentioned the possibility of carbon enhancing the chemisorption of aggressive ions.⁶²⁻⁶⁴ Flis emphasized the role of carbon in altering the anodic polarization characteristics of steel.³⁷ Humphries and Parkins showed with electron microscopy and microhardness measurements that the amount of carbon dissolved in grain boundaries was reduced by increasing amounts of cold work.⁵⁴ Such redistribution seemed to match the findings of other studies: that minor amounts of deformation increase susceptibility while large amounts reduce susceptibility to SCC.⁴⁹ Flis postulated an alteration of the oxide species which are stable on steel under SCC conditions due to surface enrichment in carbon.^{37,65} While low carbon

steels of about 0.01% C crack exclusively along grain boundaries, Zabik found some degree of "transgranular" cracking through pearlite areas in higher carbon steels.⁵⁰ However, the cracks in pearlite were parallel to cementite platelets and thus intergranular with respect to the two pearlite phases.

Nitrogen is another interstitial constituent of steel which was thought to play a role in SCC susceptibility. An early theory by Waber and McDonald, that strain induced Fe_4N was anodic to the matrix and provided a preferred path for dissolution,⁶⁶ was discounted by Parkins by analyzing data for several nitrogen containing steels in which no correlation with nitrogen content was found.⁵² The increased resistance to cracking imparted by large amounts of nitrogen contradicts such a mechanism. Small amounts of nitrogen (0.043%) when introduced into a steel do induce susceptibility,⁶² however the influence of carbon appears to be far more significant.³²

A dominant role of interstitial oxygen was disproved by Long and Uhlig who demonstrated that oxygen up to 0.07% did not induce susceptibility to nitrate cracking.⁶⁷

The possibility of hydrogen embrittlement being involved in SCC of mild steels was discounted by Logan and Yolken on several counts.⁶⁸ Specimens that were exposed to acetic acid-hydrogen sulfide solutions failed transgranularly by a hydrogen embrittlement mechanism, whereas specimens of the same steel that were exposed to NH_4NO_3 failed intergranularly. A hydrogen embrittled specimen, designed with a hollow cavity in the interior, showed a rapid influx of hydrogen into the cavity. The nitrate exposed specimen showed less influx than a specimen exposed to distilled water (which caused no cracking to occur). Hydrogen cracking

occurred extremely rapidly after crack initiation, while nitrate cracking progressed slowly. Finally, hydrogen embrittlement cracks originated at the root of starter notches while a pair of nitrate cracks began above the root of the starter notch, each on a side wall of the notch.

Substitutional alloying elements have a pronounced effect on SCC in nitrate solutions. One study related the incidence of cracking to segregation of substitutional alloying elements rather than to interstitials. Using transmission electron microscopy Flis and Scully found corrosion along transgranular corrosion paths which they identified as prior austenite grain boundaries.⁵⁷ It was suggested that these transgranular paths followed the segregation of substitutional impurities. Aging at 250°C for up to 5 hours had no effect on the microscopic cracking path, apparently ruling out the role of carbon and other interstitial elements in SCC of carbon steel. Neither could cracking be related to the presence of dislocations or precipitates. These results are in contrast to most other investigations in the literature, and fail to explain the observations of cracking along ferrite grain boundaries⁵⁰ and the pronounced effect of tempering and aging heat treatments.⁶²

Killed steels appear to be less susceptible to cracking in nitrate solutions than rimmed steels. This would indicate that aluminum and silicon added as deoxidizers are beneficial. Several investigators found that aluminum and titanium-killed steels were resistant to cracking,^{59,69,70} while others were unable to support such claims.⁷¹ Long and Lockington found that aluminum was only beneficial in quenched

and tempered steel, in which its nitride forming ability became of paramount importance.⁶⁴ The susceptibility of nontempered, aluminum-killed steels was attributed to quenching stresses.⁵⁹ It would appear that the benefit or detriment of alloying elements such as aluminum and titanium arises from the influence of such materials on the concentration of interstitial atoms such as carbon, oxygen and nitrogen. This influence may also explain the apparent immunity of 1% Cr-0.5% Ti steels because both elements are strong carbide formers.⁶⁴ The promotion of cracking by a 1% Ni addition was thought to be due to promotion of carbon solubility in grain boundaries. On the other hand, there is some indication that chromium or aluminum additions may be beneficial by stabilizing a highly protective oxide film.⁵² Another alloying addition known to be detrimental is copper, although no explanation for its effect has been developed.⁷²

The influence of post-annealing cooling velocity on nitrate cracking was studied using smooth surfaced specimens. It was demonstrated that susceptibility increased as cooling velocity increased from furnace cooling to air cooling to oil quenching to water quenching.^{30,62,69} The effects of such a change in cooling velocity were assumed to be chemical in nature.⁶²

Tempering after quenching relieves internal stresses and in some cases reduces susceptibility to nitrate cracking. The effect of tempering is more complex than merely stress relieving, and tempering can in some cases induce greater susceptibility. For low carbon steels Uhlig and Sava found tempering in the range 250°C to 700°C reduced susceptibility.⁶² Tempering at other temperatures was almost totally ineffective.

Minimum susceptibility occurred in the tempering range above 550°C for higher carbon steels.⁶⁹ This indicates that the effects of tempering are composition dependent.

The composition-dependent effect of tempering on nitrate cracking is difficult to interpret. Long and Lockington found that prolonged tempering at low temperatures induced susceptibility to SCC in pure iron and in iron alloys containing manganese and nickel.⁶⁴ Prolonged tempering at high temperatures reduced susceptibility again. These materials contained very small amounts of interstitials (up to 0.003%). The apparent activation energy for onset or loss of susceptibility was found to be 92 kJ/mole (22 kcal/mole) and 109 kJ/mole (26 kcal/mole).⁶⁴ These values are similar to the activation energies for atomic diffusion of carbon and nitrogen in ferrite.⁶⁴ In steels containing much larger amounts of interstitials such as mild steel and carbon and nitrogen steels the activation energies are quite different. Uhlig and Sava found that short term tempering reduced susceptibility to cracking but prolonged tempering reinduced susceptibility with activation energies of 146-176 kJ/mole (35-42 kcal/mole) for mild or carbon steel and 200 kJ/mole (48 kcal/mole) for a nitrogen steel.⁶² These values are close to the activation energy cited for thermal dissolution of nitrides (and presumably carbides) in steel.⁶²

Other alloy steels demonstrate a totally different effect or lack of effect of tempering. Chromium, titanium and aluminum steels were shown to be insensitive to the effects of 30 minute tempering heat treatments.⁶⁴ Another study involving aluminum-killed steels demonstrated that annealing reduced susceptibility, but similar annealing

induced greater susceptibility in steels containing no aluminum.⁵⁹ It was also shown that steels without aluminum could be made less susceptible if normalized, annealed at temperatures around 730°C to 780°C and air cooled. However, prolonged annealing of normalized steels at 700°C reinduces susceptibility.²⁷ Because this treatment caused spheroidization, it was postulated that accumulation of carbide globules in grain boundaries caused susceptibility. This indicates that most spheroidized steels should be fairly susceptible to SCC. However, Flix claimed that any heat treatment which increased the content of carbides or soluble carbon in grain boundaries should be beneficial and overlooked the effect of spheroidizing.³⁷

The stress required for crack initiation in mild steels in nitrate solutions⁵⁶ was shown to be proportional to the square root of the average grain diameter, d :

$$\sigma_i = \sigma_o + k d^{-1/2} \quad (1)$$

This relationship also was found for other alloys and the constant of proportionality "k" was related to the surface energy associated with creation of two crack surfaces.⁷³ Measurements of "k" in SCC tests indicated that surface energies were below those normally expected, thus supporting an adsorption mechanism for SCC.⁷³ However, this same grain size dependence also describes the plastic flow characteristics of a material and is known as the Hall-Petch relationship. Because the flow stress showed the same dependence on grain size as the SCC initiation stress, Henthorne and Parkins suggested that the grain size relationship

reflected the influence of dislocation dynamics⁵⁶ rather than an adsorption phenomenon.⁷³ They also suggested that a dislocation mechanism for SCC of mild steels might explain the effects of carbon and microstructure on cracking.⁵⁶

Metallographic analysis of the cracking process in various steels indicates a profound influence of microstructure.⁵⁰ Very low carbon steels crack exclusively by intergranular fracture with intense grain boundary dissolution and pitting being evident. Higher carbon steels undergo intergranular cracking around ferrite grains with some "transgranular" cracking through pearlite areas. Intense dissolution is found near pearlite, but the pearlite seems to block propagation of individual cracks. The use of fractography indicated that cracks that traveled through pearlite actually traveled between the lamellae of ferrite and cementite and were thus interphase cracks.⁵⁰ The cracks in patented and drawn steels seem to follow ferrite in grain boundaries of the elongated regions of bainite or pearlite.⁵⁰ Parkins showed accentuated dissolution of ferrite adjacent to carbide particles in grain boundaries.²⁷ Corroded areas adjacent to grain boundaries and carbide particles had white borders or halos instead of being coated with black oxide film. Such findings support an electrochemical dissolution model of SCC with grain boundaries acting as anodes and carbide particles as cathodes.

Caustic Cracking of Mild Steel

Influence of Environment. Service failures of boilers containing caustic solutions often originate at crevices in the riveted seams. SCC of mild steel in caustic solutions, also called caustic embrittlement,

appears to occur in a specific range of temperatures and caustic concentrations. While caustic cracking is not observed below about 15% NaOH, a limiting concentration also seems to exist at about 40% NaOH, above which service failures are not expected.⁷⁴ Cracking occurs intergranularly in general, but some evidence of transgranular cracking is found.⁷⁵ Caustic solutions cause the surface of steel to be covered with a thin, black, adherent magnetite film. The calculated potential - pH diagram for high temperatures, however, indicates that soluble hypoferrous ion (HFeO_2^-) might be stable under cracking conditions.³⁴

Specific additions to caustic solutions and the concentrations of these additives have a strong effect on caustic cracking. Increasing solution concentration of caustic in the range 20-50% NaOH appears to decrease time to failure.⁷⁶ Oxygen in small amounts promotes caustic cracking while large concentrations apparently promote passivity and thus inhibit SCC.^{38,53} Small amounts of chlorides promote caustic cracking, while large amounts reduce this effect.^{77,78} Additives that enhance susceptibility to caustic cracking include: small amounts of lead oxide,⁷⁹ small amounts of silicates,^{75,79} small amounts of nitrates,^{74,79} small amounts of oxidizers such as permanganates and chromates⁷⁹ and small amounts of sulfates.⁷⁷ Larger amounts of these same additives, however can inhibit cracking.⁸⁰ Other additions said to inhibit caustic embrittlement include acetates,⁷⁷ carbonates,⁸¹ lignin sulfonates and tannins (two commercially used corrosion inhibitors).⁸¹ Weir, however, reported that silicates, chlorides and phosphates had no effect on cracking.⁸² A careful electrochemical study of the effect of additives indicated that such confusing effects on caustic cracking were related

to shifts in corrosion potential induced by the added species.⁸³

At controlled potentials in the caustic cracking range such materials as Al_2O_3 , Cr_2O_3 , KMnO_4 , NaNO_3 , Na_3PO_4 , PbO , Pb_3O_4 and ZnO had no effect on cracking in 35% NaOH . The only effective SCC inhibitors found were valonea, quebracho tannins and NaH_2PO_4 .

The electrochemical potential exhibited by a steel specimen in caustic solution has a large influence on its susceptibility to caustic embrittlement. Both time to failure and the accompanying reduction in area of tensile specimens have a pronounced minimum at about -940 mV (SCE) in boiling, concentrated caustic solution.^{24,83,84} This potential for maximum susceptibility to cracking changes only slightly from 70° to 125°C and corresponds to values near the critical passivating potential on an anodic polarization curve.⁸⁴ Caustic cracking only occurs in a narrow range of potentials.⁶³ The probable explanation for small amounts of various additives being harmful but large amounts being beneficial with respect to caustic cracking was attributed to changes in potential by Reinoehl and Berry,⁷⁶ and is illustrated in Figure 3. Small quantities of additive may give a cathodic reduction reaction polarization curve which intersects the anodic oxidation reaction polarization curve at $E_{\text{corr } 1}$, $I_{\text{corr } 1}$ near the anodic current peak. Thus corrosion will occur at the potential and current density where the two curves intersect (anode and cathode currents are equal). Larger amounts of additive may shift the reduction reaction curve so that it intersects the oxidation reaction curve at $E_{\text{corr } 2}$, $I_{\text{corr } 2}$. In such a case the metal will be at a passive potential where SCC is much less pronounced and only very low anodic current density can flow.

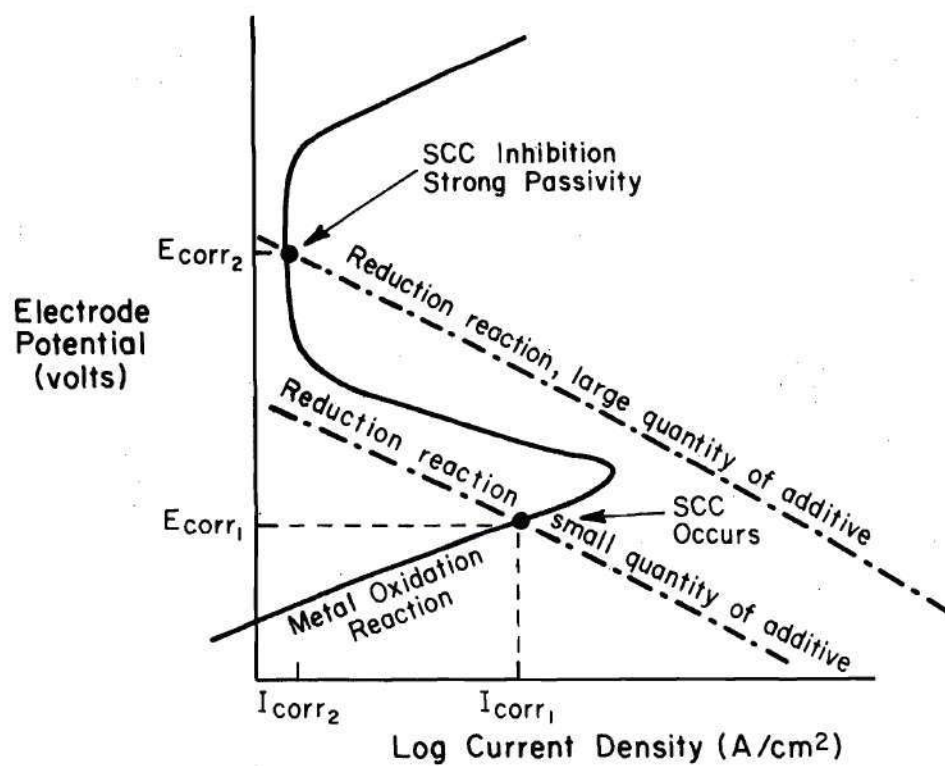


Figure 3. Effect of Additives on Corrosion and Cracking.

Magnetite is often found on the surface of specimens tested in caustic solutions.⁸⁴ However other corrosion product species have been detected as well, including maghamite ($\gamma\text{-Fe}_2\text{O}_3$)⁸⁵ and lepidocrocite ($\gamma\text{-FeOOH}$).⁸⁶ At the potential corresponding to maximum susceptibility the oxide appears to be magnetite, but at anodic potentials well into the passive range, and including the area of SCC immunity, the oxide is maghamite.^{34,84} At intermediate potentials an oxide was detected which was neither magnetite nor maghamite but seemed to be an ordered structure with twice the unit cell dimensions of magnetite.³⁴ This structure was apparently stabilized by varying concentrations of lattice vacancies which made the oxide porous and caused incomplete passivation. Reinoehl and Berry found that at the potential where cracking was most severe the general corrosion was also the most intense, and the dissolved ions turned the caustic solution green.⁷⁶ This indicated the presence of divalent ferrous ion, probably HFeO_2^- . Potentials which inhibited cracking were associated with brown or tan solutions, indicating presence of the trivalent ferric ion. The presence of soluble hypoferrous ion (HFeO_2^-) at the potential giving the most severe cracking indicates that caustic cracking is promoted by free corrosion (active dissolution) conditions. Inhibition of cracking at potentials associated with the ferric ion shows that magnetite and maghemite formation conditions can lead to passivity. These are the only protective iron species in high pH water.³⁶

The presence of both soluble and oxide species indicates that caustic cracking occurs very close to the pH-potential limits for passivity of steel. This observation prompted speculation that an active

metal-passive metal concentration cell might cause the cracking.⁷⁶ Since cracking has been associated with crevices in boilers such a cell might consist of: Fe/conc.NaOH//dilute NaOH/Fe (or perhaps Fe/low O_2 //high O_2 /Fe). Cell voltage differences as high as 700 mV were measured between two halves of a broken tensile specimen with one half passivating and the other half reverting to an active state.⁷⁶ Passivity thus appears to be metastable. This effect is illustrated in Figure 4. More than one corrosion potential and current can exist at a metal surface in a situation where the reduction reaction polarization curve intersects the oxidation reaction polarization curve at more than one point. Slight changes in surface condition such as oxide film breakdown due to strain may shift a localized region to $E_{corr 1}$, $I_{corr 1}$ and cause this region to become anodic. Other surface sites in the same piece of metal may remain at $E_{corr 2}$, $I_{corr 2}$ or $E_{corr 3}$, $I_{corr 3}$ and act as cathodes in a galvanic corrosion cell involving only a single material.

Most studies of caustic cracking indicate an acceleration of the process by increased temperature.^{63,84} An Arrhenius relationship with apparent activation energy for caustic cracking of 75 kJ/mole (18 kcal/mole) was reported for tests in boiling 33% NaOH.⁸⁴ Robinson and Nel, however, found that in boiling 50% NaOH increasing the temperature from 210°C to 240°C decreased susceptibility to caustic cracking.⁷⁵ No explanation of this unexpected temperature effect was offered.

Influence of Stress/Strain. Caustic embrittlement seems to initiate only where the yield point has been exceeded and yielding has occurred.^{75,84} Three point loaded bending specimens crack predominantly in the region of the two outer load points.⁷⁵ Cracking thus appeared to

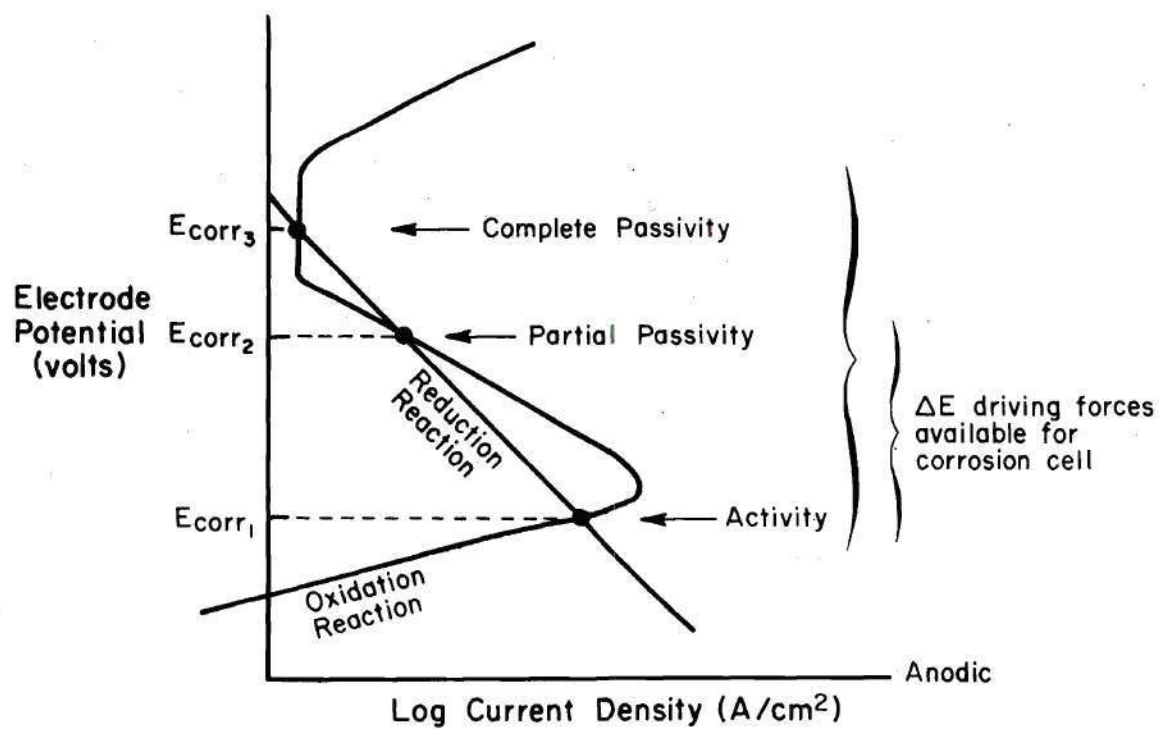


Figure 4. Conditions for Metastable Passivity.

occur in a region of high stress gradient. Specimens previously strained just above their upper yield point fail much more rapidly when tested in boiling caustic than do specimens which are not prestrained.⁸⁴ However, specimens strained 30% in air before testing have much longer times to failure, with fracture occurring outside of the necked region.⁸⁷ This seems to parallel the behavior in nitrate cracking where small amounts of deformation induce susceptibility, but large amounts increase resistance. McCarthy and Harrison were able to relate the incidence of caustic cracking to the fracturing of magnetite surface films with 0.1 to 0.8% metal strain in mild steel.⁸⁸ Yielding apparently induces caustic cracking by causing oxide rupture.

Influence of Metallurgical Properties. Bohnenkamp found that high carbon contents inhibited crack initiation on a smooth surface but not propagation of existing cracks.⁸⁷ Carbides were also found to corrode preferentially with respect to the ferrite matrix in caustic solution (unlike the relative corrosion rates found in nitrate solutions). Introduction of nitride precipitates by nitriding was shown to make steel more susceptible to cracking at low stresses, while alloying with titanium and aluminum to remove interstitial nitrogen demonstrated that cracking could occur in nitrogen-free steels as well. Rimmed steels have been found to be more susceptible than killed steels in nitrate cracking, but killed steels have been shown to be more susceptible than rimmed steels to caustic cracking.^{32,75}

Robinson and Nel discounted the role of interstitial hydrogen in embrittling steel in caustic solution. Specimens charged with hydrogen exhibited reduced ductility but those exposed to caustic failed in a

normally ductile manner upon testing in air.⁷⁵ Cracking in hydrogen charged specimens did not always originate at the surface, but caustic cracking always originated at the surface. It was found that oxidizing agents such as PbO and KMnO_4 increase susceptibility, even though such agents would not be expected to favor hydrogen ion reduction and absorption by the metal surface.⁷⁵

Heat treatment and microstructure have a decided influence on caustic embrittlement. Bohnenkamp induced susceptibility to caustic cracking by spheroidizing a normalized steel.⁸⁷ He also demonstrated that quenching a steel raised the stress required for crack formation because the heat treatment also resulted in a higher yield point. This confirmed the necessity of plastic deformation in initiating caustic embrittlement. Annealing followed by tempering in the range 400° to 700°C did not cause appreciable changes in susceptibility, however quenching and then tempering in the range 300° to 400°C reduced susceptibility. Thus quenching and tempering appear to be beneficial for both caustic and nitrate cracking.^{62,87}

Discussion of Cracking Mechanisms

One cannot find overwhelming agreement in the literature concerning the mechanism of cracking in either caustic or nitrate solutions. Both similarities (IG fracture path, yield strength dependence, microstructural dependence) and differences (narrow potential range of caustic cracking, dissimilar activation energies, opposite effects of deoxidizing alloying elements, mutual inhibition of the two ions) can be found. The same mechanisms which have been postulated for other cracking phenomena have been applied to nitrate and caustic cracking as well. These mechanisms

have been advanced for decades with little apparent agreement and without any generally accepted mechanism to date. The mechanisms proposed to explain SCC may be divided into the following categories.

Physical Processes

Mechanical Fracture Aided by Corrosion. Cracking is primarily mechanical fracture with corrosion aiding by corroding through resistant regions.⁸⁹

Corrosion Product Wedging. Materials fracture under the influence of stress generated in crevices by corrosion products having a greater volume than that of the metal being corroded.^{90,91}

Chemical Processes

Electrochemical Dissolution. Cracking consists of electrochemical dissolution along preexisting susceptible paths with stress being of secondary significance.^{40,66,92}

Physical-Chemical Processes

Tunneling and Tearing. Cracking is primarily due to corrosion tunnels which subsequently link up by mechanical tearing of uncorroded bridges in between.⁹³

Brittle Film. Cracking consists of brittle fracture of a growing oxide on a stressed metal. The crack runs into the underlying metal and arrests, and the process then repeats after refilming at the base of the crack.^{94,95}

Dissolution and Microcracks Nucleating at Stacking Faults or Slip Bands. Chemical dissolution occurs at sites of segregated impurities in stress-induced stacking faults or in blocked bands of coplanar dislocations. This preferential corrosion results in a micropit (crack)

which can then propagate mechanically for some distance.^{96,97}

Mechano-Anodic. Stress and the resultant straining of material at a crack tip result in depolarization and high rates of dissolution.^{98,99}

Film Rupture. Straining a metal will continuously disrupt the surface film and result in restricted dissolution at slip steps emerging at a crack tip. Passivation is maintained behind on advancing crack tip due to the surface film. A natural potential difference between filmed and unfilmed metal provides the driving force for corrosion to proceed.^{22,39}

Chemisorption. Adsorption of aggressive atoms or ions from solution onto a metal surface weakens interatomic bond energies at a crack tip and allows the material to fracture at a lower stress than otherwise expected.^{23,24,100}

Hydrogen Embrittlement

Planar Pressure. Hydrogen builds up gas pressure along lattice planes and causes cleavage.¹⁰¹

Void Pressure. Hydrogen accumulates in voids in a metal and builds up pressure to cause fracture.^{102,103}

Surface Energy or Bond Energy Reduction. Hydrogen diminishes the surface energy at the tip of a microcrack¹⁰⁴ or the interatomic metal bond energy in a region of maximum triaxial stress¹⁰⁵ and allows rupture at a lower stress.

Hydride Formation. Hydrogen induces formation of hydrides in the metal which then cleave or are preferentially dissolved.^{106,107}

Dislocation Pinning. Hydrogen pins dislocations and thus embrittles the material.¹⁰⁸

Dislocation Unpinning. Hydrogen increases dislocation mobility

and allows the material to fail at a lower stress.⁴

Nitrate and caustic cracking do not seem to be caused by a purely mechanical mechanism. Fracture of mild steel in air at typical cracking temperatures occurs by transgranular microvoid coalescence (dimpled rupture) instead of intergranular fracture. One may discount a corrosion product wedging phenomenon on the basis of a pronounced dependence of cracking upon heat treatment and microstructure. The wedging action of corrosion products should not be dependent upon such effects.

At the other extreme, purely electrochemical models do not seem to explain IG cracking of steel. While being supported by the claim of IG destruction of steel by anodic polarization in the absence of stress,⁵⁵ a purely electrochemical mechanism is rendered less acceptable by the appearance of a threshold stress for cracking¹³ and the observation of cracks in service only at highly stressed regions such as welds.¹ A purely electrochemical process does not explain the observed grain size effects.⁵⁶

Of the remaining models one may also discount the tunneling and tearing model since cracks are solely IG and show no evidence of repeated tearing or shear rupture features in either nitrate or caustic.⁵⁰ The brittle film model also may be discounted. Nitrate and caustic cracks show neither regularly repeated cleavage-like features nor short TG extensions branching out from the path of the main stress corrosion crack.⁵⁰ Repeated brittle fracture of the oxide film and crack arrest in the underlying metal would cause such features. Stacking fault mechanisms may also be discarded since they would not apply to the BCC structure and dislocation substructure of mild steel.

The chemisorption theory, originally proposed to explain liquid metal embrittlement, has been advanced as a generalized theory to explain all of stress corrosion cracking.²³ This theory does not seem to adequately describe nitrate and caustic cracking. There is little evidence that substantial reduction in the surface energy of metals results from contact with aqueous solutions. The theory has been applied to both IG and TG cracking with little concern for the difference in crack path. Chemisorption is not supported by the adsorption properties of crack-causing media. Ions of both low adsorbability¹⁰⁹ (CO_3^{-2} , PO_4^{-3} , OH^-)^{21,110,11} and high adsorbability¹⁰⁹ (NO_3^- , HS^- , S^{-2})^{13,14} can cause cracking of steel. In fact, high strength steels may crack in both distilled water¹¹¹ and high purity steam.¹¹² The only ion common to all these solutions that might be responsible is the hydrogen ion. Still the chemisorption theory does not explain the role of the anion in the different solutions. Surface adsorption would also be expected to occur preferentially at ledge or kink sites on a crystal face. Such a site would be generated by an emergent dislocation. However, no preferential attack has been found related to dislocations¹¹³ or their substructure.⁵⁵ The rather prominent existence of a crack incubation period¹¹⁴ in nitrate and caustic cracking cannot be explained on the basis of chemisorption. There does not appear to be any particular reason for a delay time in surface reactions. If the physical rupturing of iron interatomic bonds is solely responsible for cracking, this cannot adequately explain the marked effects of heat treatment and microstructure. Furthermore, this theory in no way accounts for the mutual inhibition effect of caustic and nitrate ions on cracking in other medium.

Hydrogen embrittlement is a possible mechanism of nitrate and caustic cracking. A hydrogen mechanism for nitrate cracking was discounted by Logan and Yolken.⁶⁸ Their results indicated a difference in fracture mode, crack velocity, and hydrogen permeation rate in acetic acid-hydrogen sulfide solution and ammonium nitrate solution. However, Beachem proposed a change in fracture mode with increasing hydrogen content in high strength steel.⁴ It is possible that the acetic acid solution resulted not only in a higher hydrogen permeation rate but also a higher hydrogen concentration in the steel studied than did the nitrate solution. The Beachem theory could account for the TG acetic acid cracks and the IG nitrate cracks. If a hydrogen mechanism were operating, a much higher hydrogen permeation rate in acetic acid might also explain the much higher crack velocities produced by this medium compared to nitrate.

A study of nitrate cracking inhibitors for mild steel showed that Na_2HAsO_4 was particularly effective.²⁸ The addition of such a hydrogen recombination poison as arsenic in solution should increase hydrogen uptake. If a hydrogen mechanism were operating this would promote cracking. On the other hand, the addition of this basic salt would raise solution pH also. Such an increase in solution pH²⁷ or the addition of one of several basic salts³² reduces susceptibility to nitrate cracking. It is not clear, therefore, whether a hydrogen mechanism is actually operating in IG SCC of mild steels in nitrate solutions.

Controversy over a hydrogen mechanism also exists in caustic cracking. While the earliest works favored a hydrogen embrittlement

mechanism, more current investigations offer other explanations such as active/passive corrosion and film rupture.^{12,75,76,87} It is not possible to draw definite conclusions at this time.

Crack tip chemistry studies revealed acidic conditions near the tip of stress corrosion cracks in other steel alloy-aqueous environment systems.^{111,115} This indicated the possibility of hydrogen generation within cracks and led to confirmation of pH-potential conditions that could produce hydrogen evolution in cracks.¹¹¹ In fact, hydrogen gas was detected coming from cracks and crevices,¹¹⁶ and a hydrogen mechanism is currently favored for the cracking of high strength steel in water or dilute chlorides.¹¹¹ While the possibility exists of such a mechanism in nitrate solutions, no attempt will be made in this discussion to critique the various proposed mechanisms for hydrogen embrittlement. They are in a state of controversy and constitute a major study in themselves. However a number of reviews^{117,118} and conference proceedings^{119,120} on the subject are available.

The two mechanisms which seem to be supported by many of the investigations of nitrate and caustic cracking are the mechano-anodic and film rupture theories, modified to account for preexisting susceptible paths at grain boundaries (in other words, strain-assisted anodic dissolution along grain boundaries). The observations of preferential corrosion attack at grain boundaries¹²¹ and an active surface potential at grain boundaries³⁸ confirm the existence of preexisting susceptible paths for corrosion. The accelerating effect of plastic deformation on both nitrate⁵⁶ and caustic⁸⁷ cracking indicates that strain assists the corrosion process.

The susceptibility of grain boundaries to localized corrosion in nitrate solutions seems to involve the presence of interstitial impurities. It was demonstrated repeatedly that small additions of elements such as carbon^{32,37} and nitrogen⁶² significantly increased nitrate cracking susceptibility in iron. Flis and Scully claimed that cracking resulted from substitutional impurity atom segregation at prior austenite grain boundaries.⁵⁷ However, their heat treatments involved cooling velocities on the order of 10^5 degrees C per second. At such cooling rates it is not difficult to imagine trapping of impurities at prior grain boundaries and a resulting high strain energy path for preferential corrosion. However, there is no reason to expect that the preferential attack at ferrite grain boundaries in slowly cooled steels is exactly the same phenomenon. The influence of interstitial atoms such as carbon on SCC susceptibility of ferritic steels does not support a substitutional element mechanism.

The mechanism by which interstitials cause susceptibility in iron is still in doubt. It was proposed alternately that soluble carbon in grain boundaries both increased⁵⁴ and decreased³⁷ nitrate cracking susceptibility. Humphries and Parkins⁵⁴ claimed that carbon-rich grain boundaries acted as local cathodes and accelerated corrosion of the adjacent ferrite grain surfaces. Parkins²⁷ also suggested that carbide precipitates in grain boundaries had the same effect. However, iron carbides are cathodic to ferrite in nitrate solutions but anodic to ferrite in caustic solutions. A single electrochemical carbide mechanism cannot operate in both media. Flis however, discussed the decrease in nitrate cracking susceptibility at higher carbon contents than about 0.03% and

proposed stabilization of protective magnetite layers by carbon. He supported his idea with polarization data which showed a reduction in critical current density for passivation as carbon content increased. The same data also show higher passive region current densities with higher carbon contents, and Flis' conclusions seem highly speculative.

Studies of carbon effects on susceptibility to SCC seem to demonstrate a relationship between maximum carbon solubility in ferrite and maximum susceptibility. Referring to the iron-carbon phase diagram,¹²² steels with 0.0294% C would exhibit a higher degree of carbon rejection from ferrite into grain boundaries during cooling and the eutectoid transformation than would steels with a lower carbon content. Steels with a higher carbon content than 0.0294% would all undergo about the same degree of carbon rejection to ferrite grain boundaries during the phase transformation, but the total area of pearlite and ferrite-pearlite interfaces available for retaining the rejected carbon would also be higher. This may be related to the decrease in susceptibility at higher carbon contents. The increased yield strength with higher carbon content could have a beneficial influence on cracking⁵⁶ that predominates at the large carbon contents.

Heat treatment and carbon content both affect the carbon distribution in steel, and there should be a relationship between the effects of these two variables on cracking susceptibility. The direct proportionality between susceptibility and cooling velocity^{30,62,69} seems to indicate that nonequilibrium carbon distributions are deleterious and cause pronounced nitrate cracking. This indicates that carbon (interstitial atom) rejection to ferrite grain boundaries is responsible

for susceptibility. Since the proportionality between yield point and cooling velocity would be expected to give an inverse relationship between susceptibility and cooling velocity,⁵⁶ one might rationalize that chemical segregation effects overshadow strength considerations with large changes in cooling velocity. Uhlig et al., observed a relationship between the variation of susceptibility to nitrate cracking and both carbon content and cooling velocity. Furnace cooled specimens showed a general decrease in susceptibility with increasing carbon, but water quenched specimens showed an increasing or constantly high degree of susceptibility up to at least 0.2% C.¹²³ Earlier data of Long and Uhlig seemed to show a maximum in susceptibility at about 0.03% C even in quenched specimens,⁵⁸ but the reduction in susceptibility over 0.03% C was very slight. It appears that carbon segregation effects due to cooling velocity are more important than strength considerations in determining nitrate SCC susceptibility of smooth surfaced specimens. Therefore, interstitial atom segregation is the dominant factor in crack initiation.

The reason for grain boundary susceptibility to caustic cracking is even more obscure than for nitrate cracking. Fewer systematic studies appear in the literature. The reported relationship between carbon content and caustic cracking is not identical to that in nitrate cracking, but similarities exist. In both cases susceptibility decreases with increasing carbon content at carbon levels above the maximum solubility in ferrite of .0294% at the eutectoid transformation temperature. However, below this carbon content a decrease in susceptibility with decreasing carbon was not confirmed in caustic cracking.⁸⁷ The preferential

dissolution of carbides compared to ferrite in caustic solutions is opposite to the preferential dissolution of ferrite in nitrate solutions. This indicates that if a preferentially corroded species is required for cracking, it may be different in nitrate and caustic solutions.

The relationship between electrochemical potential and time to failure in the two cracking media shows that caustic cracking occurs in a narrow potential range⁶³ that corresponds closely to the potential-pH range of stability of the soluble hypoferrous ion at elevated temperatures.¹²⁴ Nitrate cracking, on the other hand, is severe across a wide range of potentials.^{26,63} The nitrate cracking potentials seem to correspond to those near the onset of hydrogen evolution up to the point of oxygen evolution within the region of soluble ferrous and ferric ion stability at elevated temperature.¹²⁴ Therefore, it appears that IG cracking of steel in both caustic and nitrate cracking is associated with thermodynamic conditions that favor stability of a soluble iron species. Crack propagation could occur by anodic dissolution in both cases. However, nitrate and caustic cracking both are related to the passivation properties of steel in these solutions. The steel surface must be passivate at locations other than the crack tip in order to sufficiently localize dissolution. Under such localized dissolution conditions cracks can then rapidly propagate.²²

The dependence of cracking upon surface potential could support either a dissolution or hydrogen embrittlement mechanism. Supporters of a dissolution mechanism can argue that since cracking occurs at applied potentials over one volt more positive than the hydrogen evolution range,

cracking must be due to dissolution. They can further argue that IG cracking is suppressed by cathodic polarization in both nitrate and caustic solutions,^{26,63} and point to the change in fracture path with sufficiently cathodic potentials to give hydrogen charging and TG hydrogen cracking.²¹ Since the range of potentials for nitrate cracking seems to outline the region of ferrous and ferric ion stability at about pH 3, dissolution mechanism advocates can claim that these data are compatible with the concept of the occluded corrosion cell.¹²⁵ That is, the acidic pH observed to occur at crack tips^{111,115} results from free iron dissolution and precipitation of insoluble corrosion products in a crevice. This impedes further inward diffusion of bulk solution constituents. The pH at the crack tip then becomes dependent upon equilibria between soluble ferrous ions and insoluble hydroxides in the case of steel in aqueous solutions. In such an environment the inherently anodic grain boundaries would dissolve preferentially. Behind the advancing crack tip less aggressive chemistry conditions could favor passivity, and dissolution would be localized to the crack tip.

Hydrogen mechanism advocates can draw support from the potential ranges for cracking which lie near to or encompass the region of hydrogen evolution in both nitrate and caustic cracking. They also suggest that the potential within a crack or crevice is relatively independent of the externally applied potential,¹²⁶ and in this way they counter arguments that potentials can be too high for hydrogen evolution. They can point as well to Beachem's postulate that fracture mode can change from IG to TG with increasing hydrogen content.⁴ This would refute the argument that the change in fracture mode with cathodic polarization was

due to a change in cracking mechanism.²¹

There is also a controversy concerning the role of stress in IG SCC of steel in nitrate and caustic. If a hydrogen embrittlement mechanism were operating, stress might lead to increased hydrogen solubility in ferrite and allow buildup of a critical concentration for embrittlement.¹⁰⁵ Louthan suggested that stress-induced dislocation motion might act as a "hydrogen pump" to create immense hydrogen pressures at suitable internal defects such as voids or microcracks.¹²⁷

If a dissolution mechanism were operating, stress would probably cause one of two effects. Either metal straining would cause film rupture^{22,39} or strain activation of the dissolution process.^{98,99} It was suggested that oxide rupture was the primary role of stress in both nitrate⁴¹ and caustic⁸⁸ cracking. If a condition exists at the crack tip which is favorable for soluble ion formation, it would be difficult to justify a film rupture model. In some way oxide formation would have to be involved in the process, perhaps induced by the presence of dissolved oxygen. In fact, studies of caustic and nitrate cracking report surface films at a solution pH in the soluble ion stability range.⁸⁴ On the other hand, there are those who maintain that jumps in anodic current are much too large to be caused by oxide rupture.³⁴ They favor a strain-activated dissolution model. Others, however, claim that one can in fact account for current jumps solely on the basis of oxide rupture.^{49,128}

Summary

The cracks observed in some of the nuclear waste storage tanks at the ERDA Savannah River Plant appear to be caused by nitrate stress

corrosion cracking.⁸ Surface potentials exhibited by waste tank steels in the caustic-nitrate waste solutions are in the nitrate cracking range.⁹ Cracks in waste tanks are associated with residual stresses in weld regions;^{6,8} stress relief of new tanks has been successful in avoiding SCC.⁸ Other metallurgical influences on the SCC of waste tank steels are not completely understood.

Much of the data in the literature support a strain-assisted anodic dissolution mechanism of IG SCC of mild steel in nitrate or caustic solutions. However in light of the solution chemistry at crack tips in other aqueous environments,^{111,115} hydrogen embrittlement cannot be ruled out.

Nearly all of the SCC data for carbon and mild steels in nitrate or caustic solutions come from tests that use smooth surfaced specimens. These data do not differentiate the crack initiation and propagation stages of SCC and tend to emphasize surface properties and crack initiation. The cracking susceptibilities of such steel specimens are inversely proportional to yield strength in both nitrate⁵⁶ and caustic solutions.⁸⁷ However, yield strength is not the only important factor in determining cracking susceptibility. Although the cracking susceptibilities of heat treated steels increase with increasing cooling velocity,^{30,62,69} the yield strength also increases. Other effects of heat treatment such as grain boundary segregation of impurity atoms during cooling must override the influence of yield strength.

In order to more precisely determine the influence of heat treatment and microstructure on the IG SCC of steel, it is necessary to study separately the crack initiation and the crack propagation stages of SCC. Precracked fracture specimens can be used for such studies.⁵¹

CHAPTER II

MATERIALS, EQUIPMENT AND EXPERIMENTAL PROCEDURE

Experimental Program

Objective of Study

The primary objective of this study was to determine the influence of heat treatment and microstructure on the SCC of a typical waste storage tank steel, A 516 Grade 70, in synthetic caustic-nitrate nuclear waste solutions. Further, it was hoped that a knowledge of how microstructure affected the SCC characteristics of the steel would increase understanding of the cracking mechanism.

Two potential applications of the results of this study are to indicate possible metallurgical influences on waste storage tank cracking and to provide information that is potentially useful in waste tank design.

Experiments

A waste tank test weld in A 516 Grade 70 steel was examined to identify typical waste tank microstructures. Laboratory heat treatments of a single plate of A 516 Grade 70 were made in order to approximate certain of the weld microstructures and to obtain a wide variety of structures. All test specimens were sectioned from the same plate.

Round bar tensile specimens of the various microstructures were tested in air to determine mechanical properties of the test material. Notched and fatigue cracked fracture specimens were stressed in nitrate and caustic-nitrate solutions. The fracture specimens were used in

constant load and constant crack opening displacement stress corrosion experiments⁵¹ to measure the stress corrosion crack propagation rates and the threshold stress intensities for cracking in the various microstructures. Unstressed corrosion coupons and polarization electrode specimens were tested in nitrate and caustic-nitrate solutions in order to determine the corrosion properties of the microstructures. The stress corrosion properties of the various microstructures of A 516 Grade 70 were then related to their mechanical (tensile) properties and their electrochemical (corrosion) properties. Additional experiments were conducted to examine the effects of various environmental variables such as nitrate solution pH and temperature on corrosion and cracking in order to clarify the cracking mechanism. The details of each particular test are discussed in the appropriately titled sections of this chapter.

Test Material and Heat Treatment

ASTM A 516 Grade 70 Test Material

The latest waste storage tanks constructed at the Savannah River Plant were fabricated from ASTM A 516 Grade 70 steel. Specification ASTM A 516 Grade 70 (Table 1, Appendix A) is for a silicon-killed carbon steel for moderate and low temperature pressure vessel service.¹²⁹ All testing materials came from a single heat of 2.54 cm (1 in) thick hot-rolled plate fabricated by Bethlehem Steel Corp., heat number 518X0796. The manufacturer's test and analyses for this heat are listed in Table 2 (Appendix A).

A 516 Grade 70 Weld Microstructures

Test welds were made during waste storage tank fabrication using

an unknown heat of A 516 Grade 70. One such weld was examined for microstructure, and a micrograph of a transverse weld section (etched with 2% nitric acid in ethanol) is shown in Figure 5.

The weld fusion zone (center of Figure 5) consists of dendritic grains as shown in Figure 6. The upper weld bead (Figure 6) exhibits directionally solidified dendrite growth, while the lower weld bead (not shown) is more equiaxed in structure. Immediately adjacent to the fusion zone is a narrow region of massive transformed austenite grains interspersed with Widmanstätten ferrite needles (Figure 7). This region and regions further from the weld centerline did not become molten. The large size of the transformed grains is due to austenite grain growth at high temperature. The transformed austenite grains seem to be partially martensitic and partially pearlitic, and in this region the hardness is 232 DPH (R_c 18.5).

The structures more distant from the weld centerline than the massive grain region are of finer grain size because of the lower austenite solution temperatures during welding. An intermediate grain size structure was probably heated to midway in the austenite range (Figure 8). The pearlitic areas in such a region may still be partially martensitic, but the hardness in this region is much lower than the coarse structure: 172 DPH. Still further from the weld centerline the ferrite grain size is extremely small (Figure 9), and the region appears as a light band across the welded plates (Figure 5). This structure was heated to a low temperature in the austenite range. Hardness is not significantly changed from the coarser-grained structures, perhaps due to the opposing influences of decreased grain size and decreased martensite content. Still

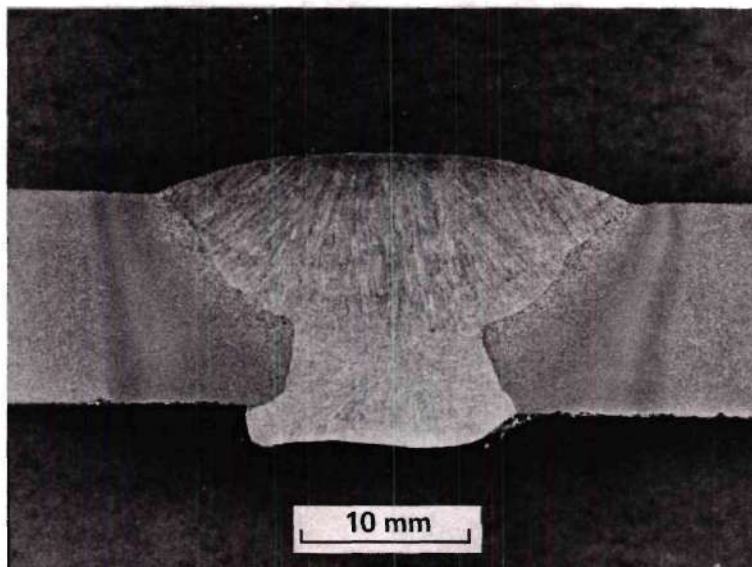


Figure 5. Transverse Section of Test Weld Showing Thermal Effects.

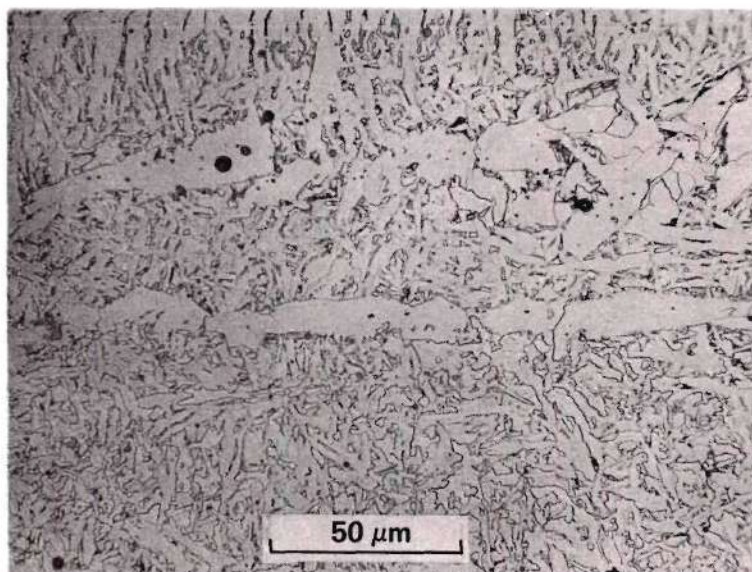


Figure 6. Upper Weld Bead (Top, Central Region of Figure 5).

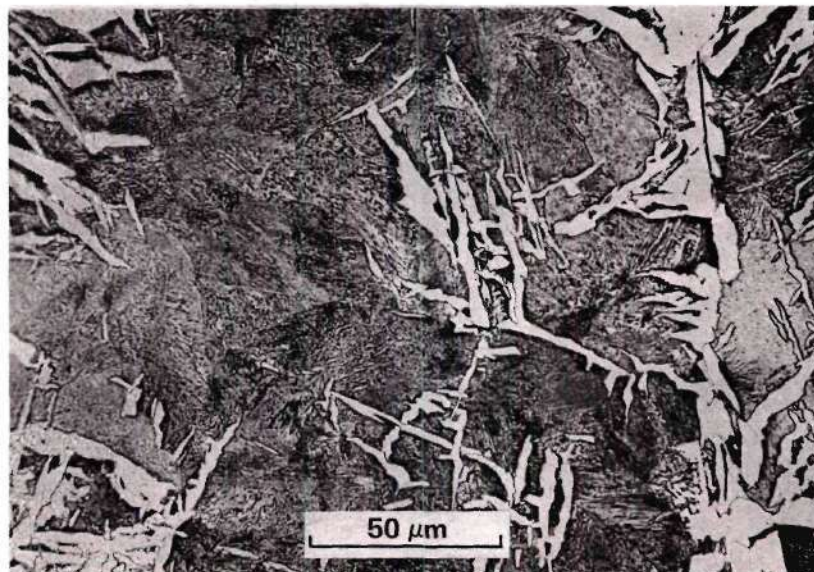


Figure 7. Massive Grains (Adjacent to Weld Bead in Figure 5).

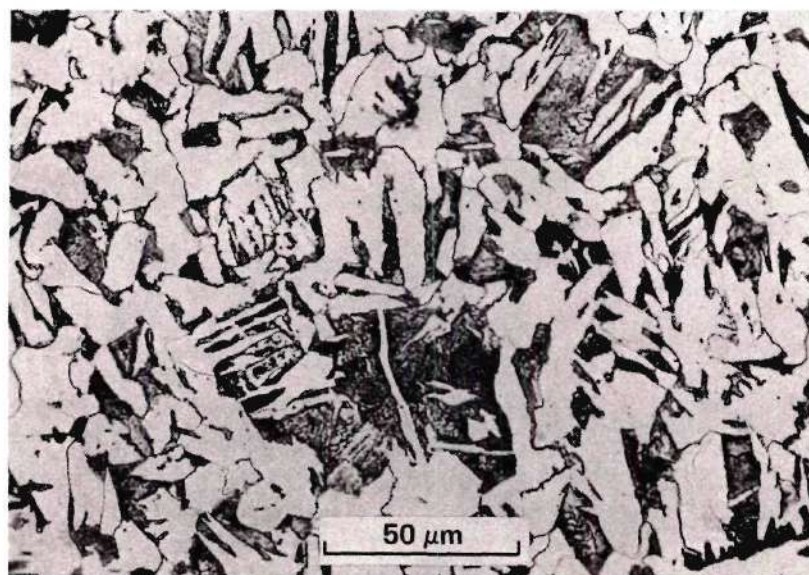


Figure 8. Intermediate Grain Size (Between Weld Bead and Light Band Across Plates in Figure 5).

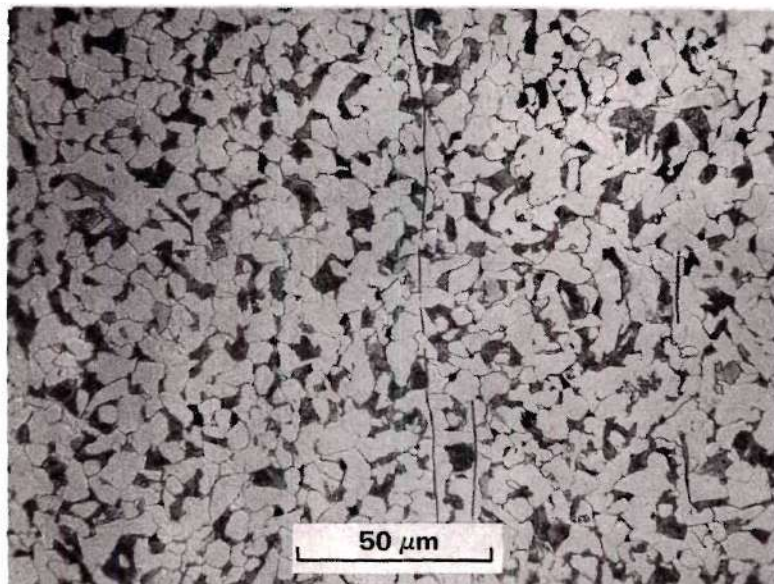


Figure 9. Refined Grains (Light Band Across Plates in Figure 5).

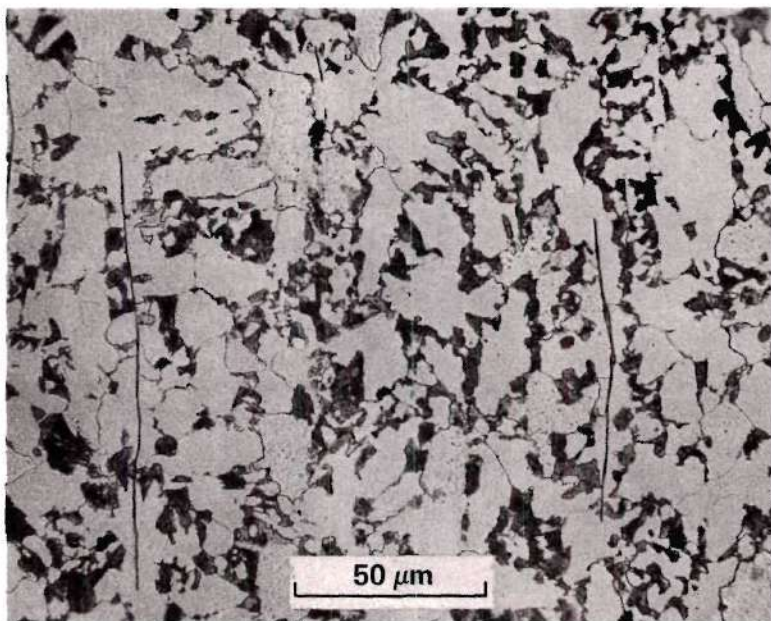


Figure 10. Feathery Pearlite (Dark Band Across Plates in Figure 5).

further from the weld centerline is a dark band across the welded plates (Figure 5). This is a partially spheroidized structure, usually referred to as feathery pearlite or troostite (Figure 10). This zone apparently was heated to approximately the eutectoid transformation temperature for a short time during welding. All structures further from the weld centerline (than the dark band of Figure 4) were heated to below the eutectoid transformation temperature and appear to be relatively unaffected base metal of hardness 165 DPH. A typical microstructure in this hot-rolled base metal is shown in Figure 11.

Laboratory Heat Treatments

The heat treatments used in this study are outlined in Table 3. They include quenching, quenching and tempering, normalizing and spheroidizing. Hot-rolled, as-received material was also tested. These heat treatments were chosen in an effort to simulate certain weld microstructures and also to examine as wide a range of structures as possible. All microstructures shown in this study were polished using standard metallographic practices and were chemically etched with 2% nitric acid in ethanol.

Certain microstructures which occur in a weld region may be approximated in large sections by appropriate heat treatments. Because of hardenability limitations, other structures, such as martensitic structures, cannot be produced uniformly throughout the cross section of a large quenched specimen. Furthermore, the large grain sizes which were observed adjacent to the weld fusion zone cannot be produced in large specimens without extremely high temperatures that result in "burning" the steel (oxidizing grain boundaries). The weld structures which were

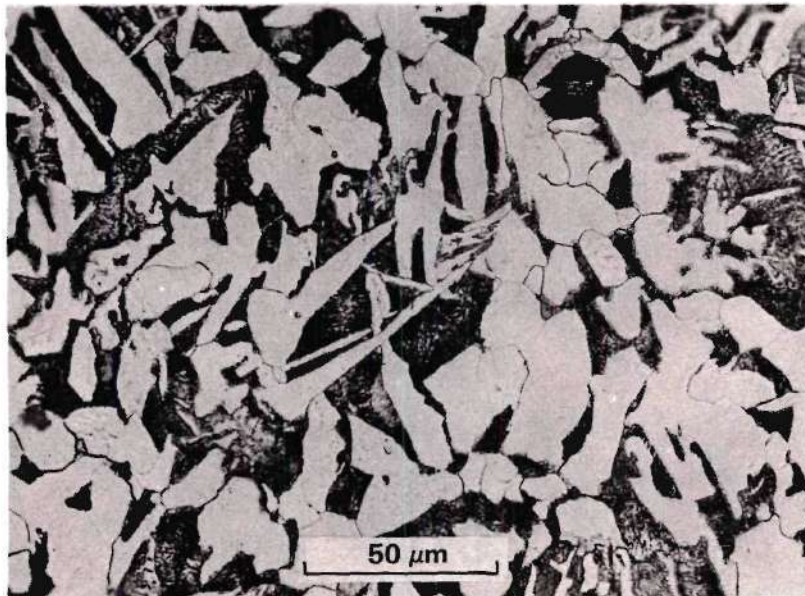


Figure 11. Unaffected Base Metal of Unknown Heat (Welded Plates in Figure 5).

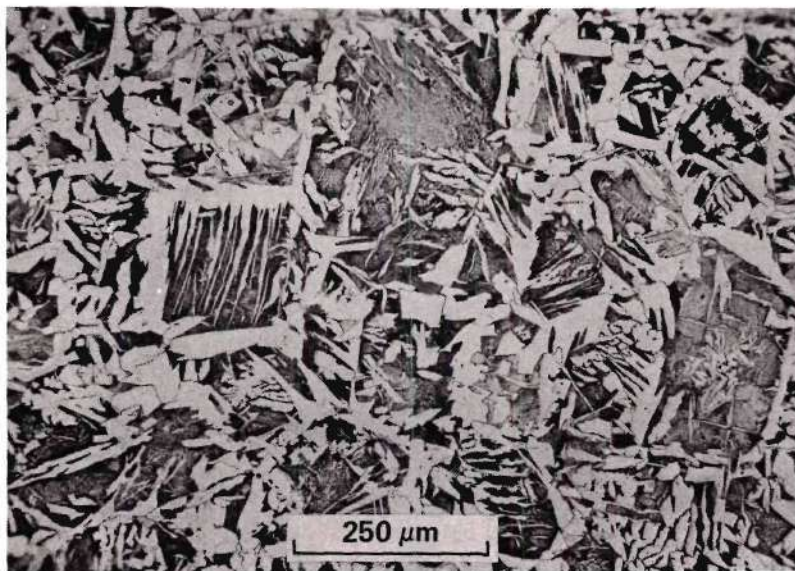


Figure 12. Heat 518X0796; Heat Rolled Condition.

approximated by heat treatment included the intermediate grain size region (by quenching) and the grain-refined region (by normalizing).

The hot-rolled, as-received material from heat 518X0796 is shown in Figure 12. This material has a Widmanstätten structure that indicates solution annealing at a very high austenite temperature before hot rolling.

A fine grained ferrite-pearlite structure was produced by heating the hot-rolled material to 1108°K (1535°F) for one hour followed by cooling in still air (normalizing). This heat treatment reduced the hardness and refined the grain size of the original material. The hardness of normalized material was about 155 DPH compared to 205 DPH for hot-rolled material. The degree of grain refinement can be seen by comparing Figures 12 and 13.

Quenching in iced 10% brine after heating to 1108°K (1535°F) for one hour produced a complex structure with suppressed ferrite nucleation (Figures 14 to 16). A substantial amount of proeutectoid ferrite can be seen in the structure. Scanning electron microscopy reveals that the transformed austenite grains contain a fine dispersion of pearlitic or bainitic carbide particles (Figure 16). The hardness, 230 DPH, indicates that some martensite may be present. X-ray diffraction patterns indicated broadening of ferrite peaks (perhaps due to unresolvable martensite). Diffraction peaks corresponding to cementite (Fe_3C) and epsilon carbide (Fe_2C) were also found. The cementite is indicative of pearlite, and epsilon carbide is found in bainite or tempered martensite.

The quenched structure was reheated to the eutectoid transformation,

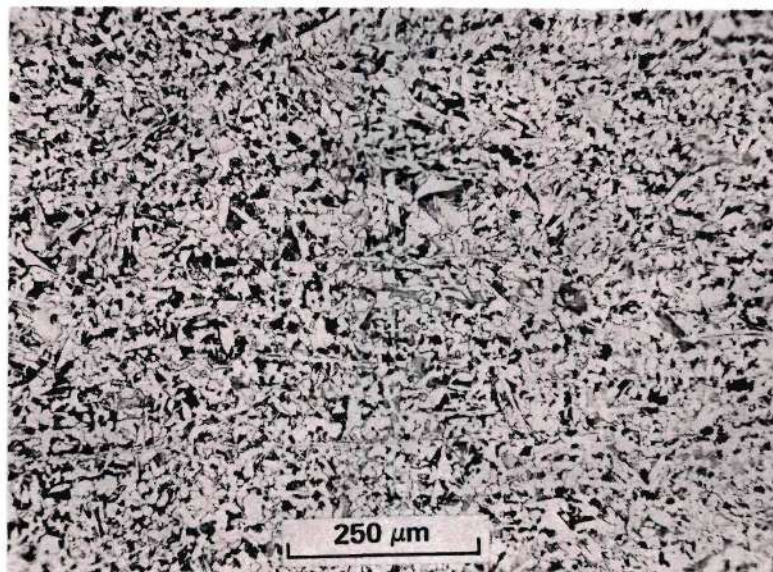


Figure 13. Heat 518X0796; Normalized Condition.



Figure 14. Heat 518X0796; Quenched Condition.

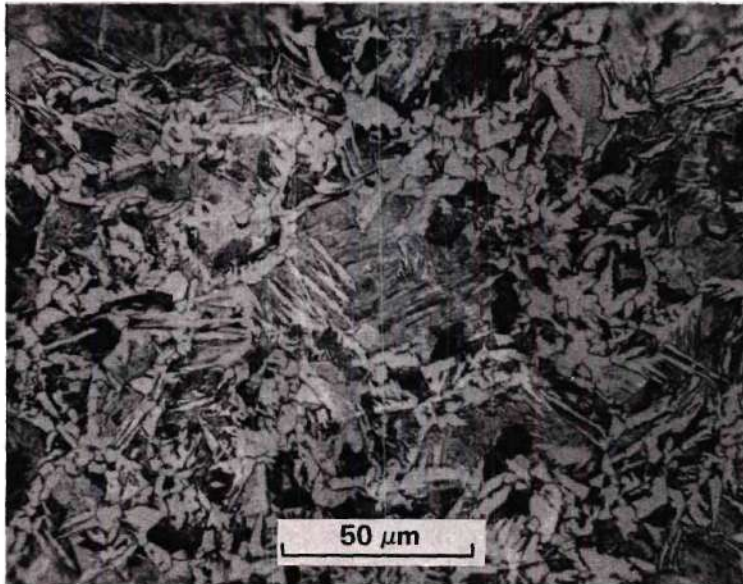


Figure 15. Heat 518X0796; Quenched Condition.

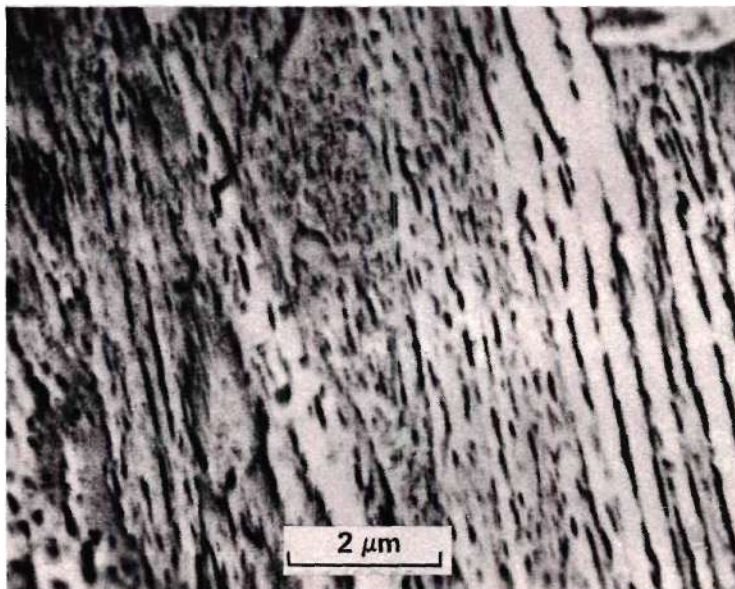


Figure 16. Heat 518X0796; Quenched Condition.

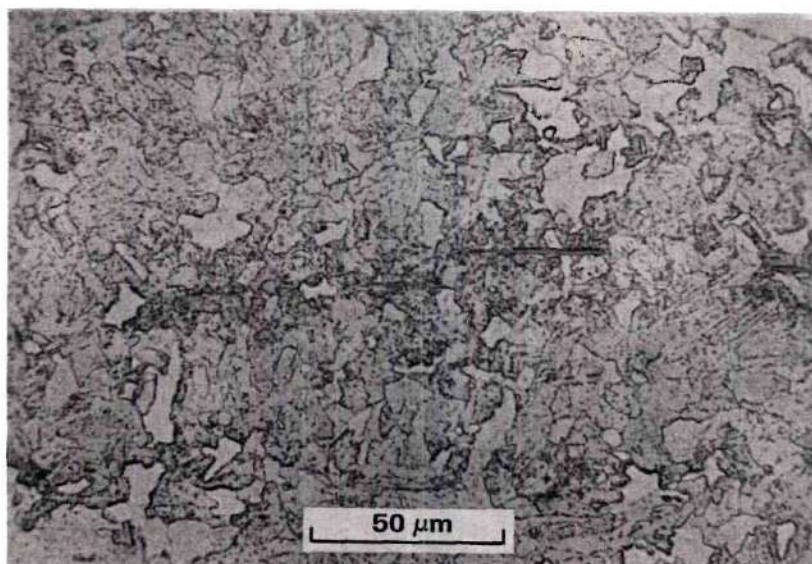


Figure 17. Heat 518X0796; Spheroidized Condition.

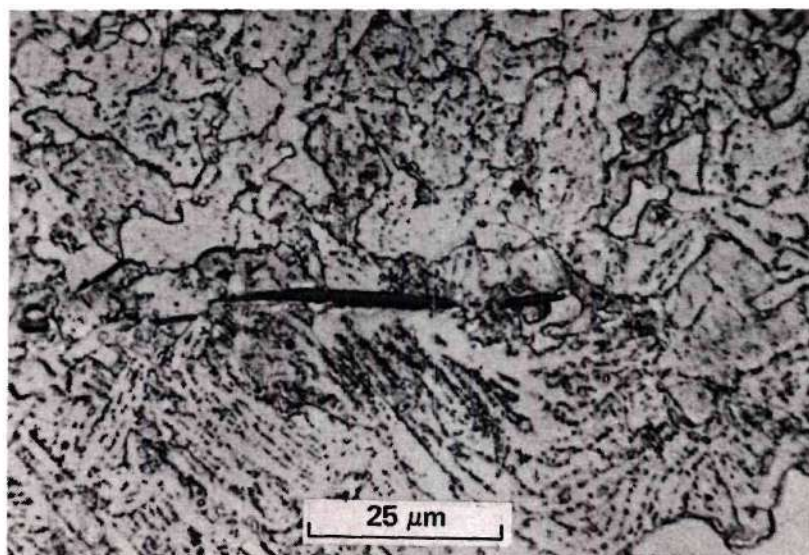


Figure 18. Heat 518X0796; Spheroidized Condition.

977°K (1300°F), for four hours (followed by air cooling) to finely spheroidized the carbide precipitates (Figures 17 and 18). This heat treatment reduced the hardness to the same level as the normalized structure (155 DPH). A preferential distribution of carbides along grain boundaries and prior cementite platelets or martensite needles can be seen (Figure 18). Scanning electron microscopy of the structure also shows carbide agglomeration along grain boundaries (Figure 19).

Test specimens which were heat treated to produce these microstructures were designated HR (hot-rolled, as-received), N (normalized), Q (quenched) and S (spheroidized). Hot-rolled, normalized and quenched materials were also coarsely spheroidized by holding at 997°K (1300°F) for 72 hours and were designated HS, NS and QS respectively. The microstructures of these specimens are shown in Figures 20, 21 and 22. Additionally, some quenched material was tempered at 866°K (1100°F) for one hour in order to examine the effects of tempering (a common method of stress relief). This microstructure was designated QT11 and appeared identical to the Q treatment. Spheroidized material was also quenched from 977°K and was designated SQ. These heat treatments provided a variation in grain size, carbide morphology and cooling velocity. All heat treatments were conducted in air in a furnace controlled to $\pm 1^\circ\text{K}$ (2°F).

All of the material that was examined had numerous stringers (Figures 9, 10, 17, 18, 19). These were analyzed by X-ray fluorescence analysis and were identified as MnS, a common inclusion in mild steels. Additionally, it can be seen that areas in the hot-rolled plate from heat 518X0796 are austenite grain size ASTM one to two and exceed the

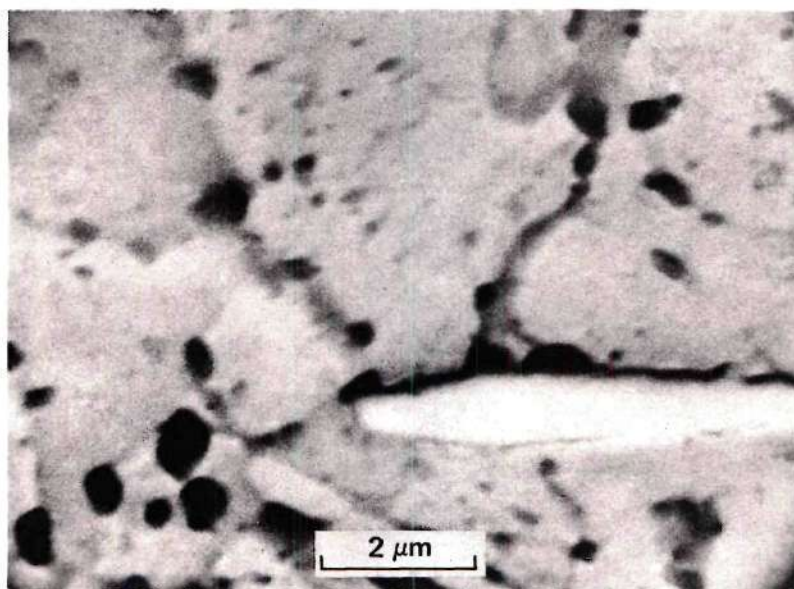


Figure 19. Heat 518X0796; Spheroidized Condition.

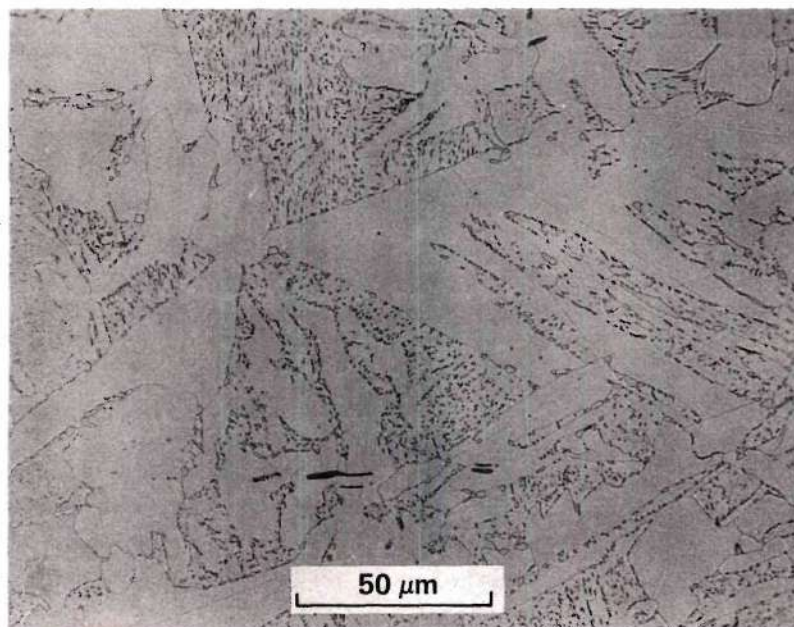


Figure 20. Heat 518X0796; Hot Rolled and Spheroidized Condition.

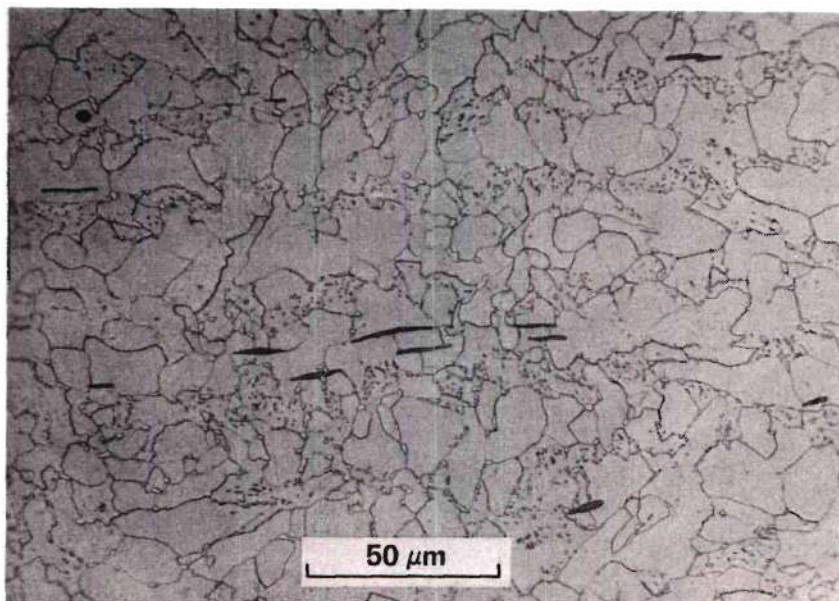


Figure 21. Heat 518X0796; Normalized and Spheroidized Condition.

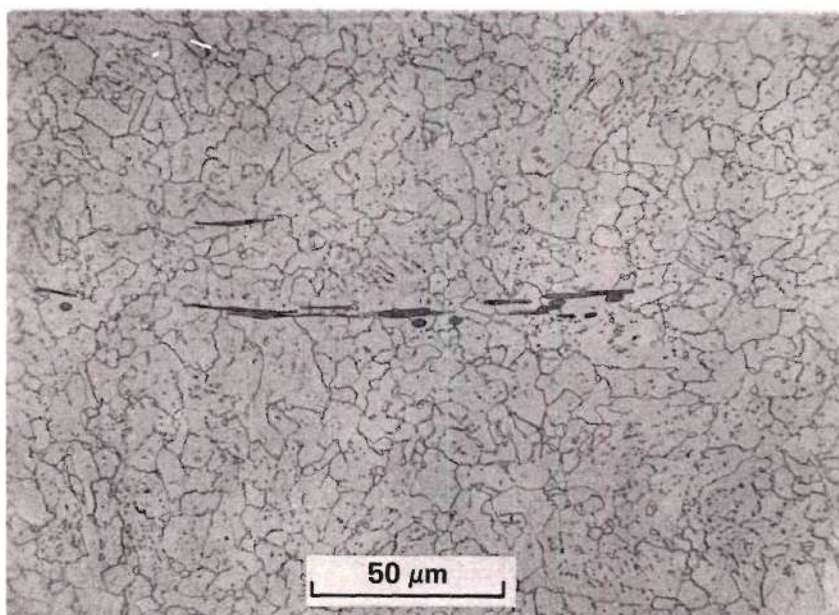


Figure 22. Heat 518X0796; Quenched and Spheroidized Condition.

ASTM specification for austenite grain size (Figure 23 and Table 1).

To avoid unknown orientation effects, all test specimens were labeled according to their orientation in the original heat 518X0796 plate. These designations are outlined in ASTM E 399 (Figure 24).¹³⁰

Tensile Tests in Air

To characterize the mechanical properties of each microstructure, tensile tests were conducted in air.

Tensile Specimens

Round bar tensile specimens of 0.635 cm (0.25 in.) gage diameter and 5.08 cm (2 in.) gage length were fabricated from heat treated 2.54 x 2.54 x 15.24 cm (1 x 1 x 6 in.) bars (Figure 25). Specimens were cut in a TL or LT orientation. Most of the tensile specimens were oriented in the TL direction (i.e., the axis of the specimens was along the transverse axis of the rolled plate shown in Figure 24). A few were oriented along the longitudinal axis, the LT orientation, to identify orientation effects. Duplicate TL specimens of the HR, N, Q, QS, S, HS, NS and QT11 microstructures were tested; duplicate LT specimens of the HR and N heat treatments also were tested. All specimens were vapor degreased in benzene and ultrasonically cleaned in distilled water and ethanol before air drying.

Tensile Test Equipment and Procedure

Tensile tests were conducted on an Instron Model TT Universal Testing Machine at initial strain rates of $\dot{\epsilon}_0 = 8.3 \times 10^{-5} \text{ s}^{-1}$ and $8.3 \times 10^{-6} \text{ s}^{-1}$. Both specimens and grips were located in an environmental chamber with the temperature regulated to $370^\circ\text{K} \pm 1^\circ$ ($206^\circ\text{F} \pm 2^\circ$). Strain was calculated from crosshead displacement. Various stress and

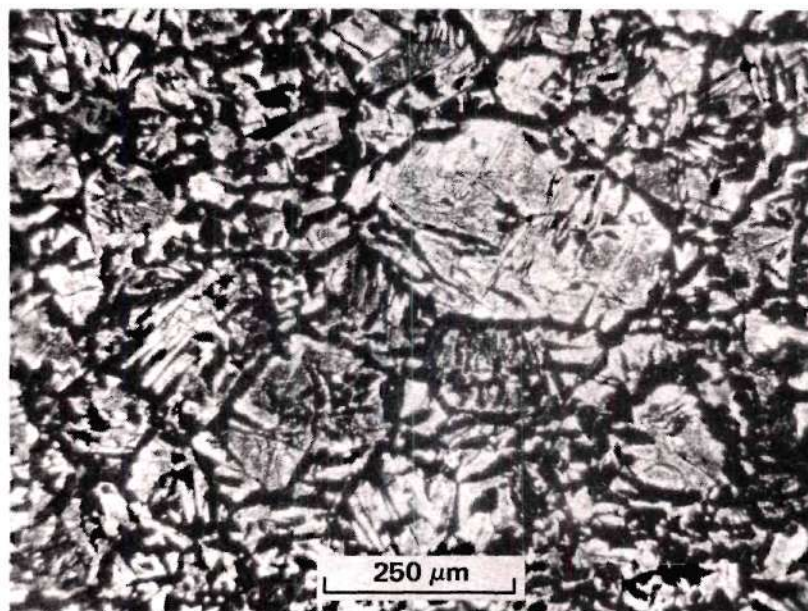


Figure 23. Grain Size of Heat 518X0796; Polarized Light,

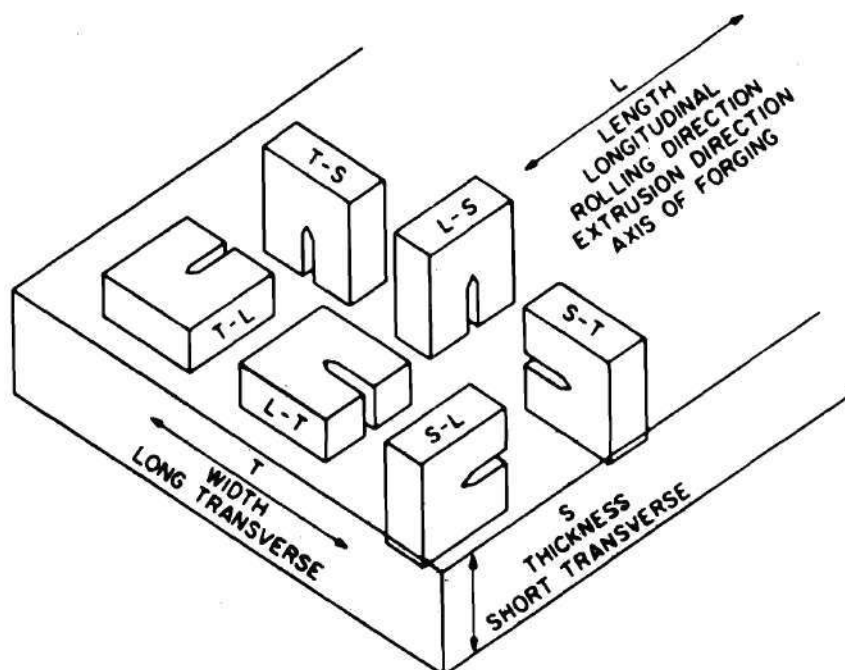


Figure 24. ASTM Crack Plane Orientation Code for Rolled Plate (Reference 130).

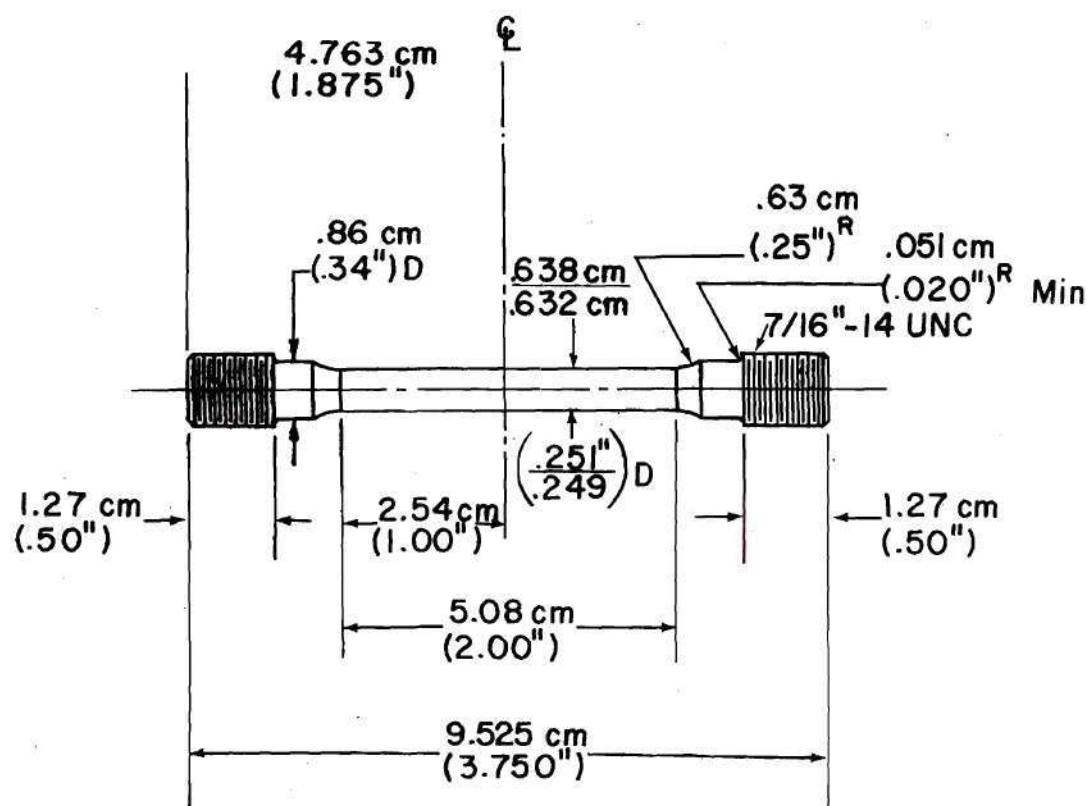


Figure 25. Round Bar Tensile Specimen.

strain parameters were calculated from the load-displacement records for each microstructure in order to characterize the mechanical properties of the microstructures.

Stress Corrosion Cracking Experiments

Two types of stress corrosion cracking experiment were conducted in synthetic nuclear waste and various nitrate solutions. One test, conducted at constant load, utilized compact tensile (CT) specimens¹³⁰ which were dead weight loaded by an overhead beam arrangement. The other test, conducted at constant crack opening displacement, utilized wedge-opening-loaded (WOL) specimens¹³¹ which were self-loaded by a bolt and pin. While in the constant load test the stress intensity increased with crack propagation, in the constant crack opening displacement, test the stress (intensity) decreased. The primary reasons for using these specimens are that they may be precracked by fatigue and are large enough to permit crack growth rate measurements over an extensive distance in the material. Precracking simulates the formation of a sharp crevice during the so-called crack initiation stage of SCC⁵¹ and reduces the crack initiation time. The CT specimen constant load tests were of relatively short duration and were used for a quick measure of relative crack propagation rates between various microstructures of steel. The WOL specimen constant displacement tests were of much longer duration than the constant load tests but required no external load equipment while specimens were cracking. Furthermore, WOL specimens were used to determine not only crack propagation rates but also the threshold stress intensity below which crack growth rate is negligible. This parameter is a measure of SCC susceptibility which, along with crack

propagation rate, allows determination of the relative resistance of different alloys or microstructures to SCC in various cracking media.

Constant Load Tests

Constant Load Specimens. Compact tensile specimens were fabricated to dimension $W = 5.08 \text{ cm (2 in.)}$ (Figure 26).¹³⁰ All specimens were 1.9 cm (0.75 in.) thickness, a representative waste tank plate thickness. Most of these specimens were machined in a TL orientation, and a few were made in the LT orientation. Specimens were vapor degreased in benzene or toluene, and the sides were wet ground to a 600 grit finish. The specimens were then ultrasonically cleaned sequentially in distilled water and ethanol and were air dried.

The notch in the CT specimens was sharpened by fatigue cracking in tension on a CGS-Lawrence (Division of Instron Corp.) Dynamic Test Machine at a maximum stress intensity of $24.7 \text{ MPa(m)}^{\frac{1}{2}}$ ($22.5 \text{ ksi(in.)}^{\frac{1}{2}}$) and a minimum stress intensity of $1.4 \text{ MPa(m)}^{\frac{1}{2}}$ ($1.25 \text{ ksi(in.)}^{\frac{1}{2}}$) and a frequency of about 20 Hz. Crack progression was measured with a travelling microscope set up to view the side of the specimen. The fatigue crack was extended to a crack length of 1.78 cm (0.7 in.) measured from the load centerline. In some of the Q specimens the fatigue cracks were initiated at a somewhat higher maximum stress intensity in order to obtain a crack in a reasonable length of time. However, at no time did the maximum stress intensity during fatigue cracking exceed 55% of the initial stress intensity during stress corrosion testing.

The stress state at the tip of a crack in elastic materials can be characterized by the stress intensity factor, "K". For compact tension specimens loaded in plane strain the stress intensity factor

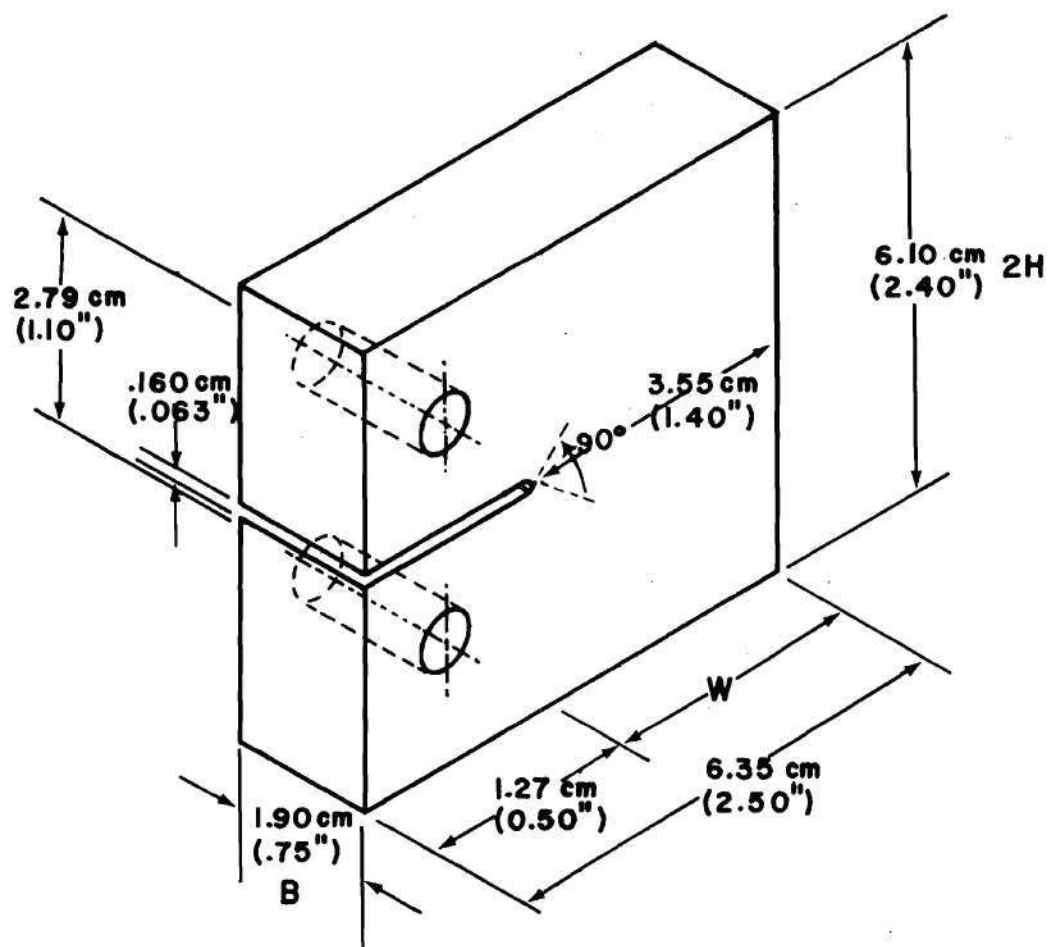


Figure 26. Compact Tensile Specimen.

can be represented:

$$K_I = \frac{Y P \sqrt{a}}{B W} \quad (2)$$

and

$$Y = 29.6 - 185.5(a/w) + 655.7(a/w)^2 - 1017(a/w)^3 + 638.9(a/w)^4, \quad (3)$$

where "P" represents the applied load, "a" and "B" and "W" are the crack length, specimen breadth and specimen width (Figure 26) and "Y" is a finite geometry correction factor.^{130,132} The ASTM guideline for minimum plane strain dimensions¹³⁰ in a given material is

$$W-a, H, B > 2.5 (K_I / \sigma_y)^2 \quad (4)$$

where " σ_y " is the yield stress and the dimensions are as denoted in Figure 26. Low strength materials such as mild steels meet the guidelines only in the case of very low stress intensities or very large specimen dimensions. A 516 Grade 70 requires minimum dimensions far larger than typical waste tank plate thicknesses (e.g., the 1.9 cm (0.75 in.) thickness used in stress corrosion tests in this study). Therefore, all stress intensities reported in this study are denoted K rather than K_I , where the subscript "I" indicates plane strain crack opening perpendicular to the specimen notch plane.

Constant Load Test Equipment and Procedure. Constant load tests were conducted using Baldwin-Lima-Hamilton 12,000 lb Lever Arm Creep Testing Machines (Figures 27 and 28). The CT specimens were connected to the upper and lower loading rods of the testing machines by means of 17-4 PH stainless steel clevises and pins (Figure 28). The CT specimens were placed in stainless steel beakers that were wrapped with heater tape and filled with about 1500 cm³ of solution. The tops of the beakers were sealed with a neoprene gasket and a fluorocarbon lid through which passed a vent condenser standpipe, mechanical thermometer, thermocouple well and upper loading rod. The thermocouple was connected to a temperature controller to maintain constant temperature $\pm 0.5^{\circ}\text{K}$.

Test solutions were brought to test temperature before the specimens were loaded to 32,720 newtons (N) (7,355 lb), corresponding to an initial stress intensity (K_{I1}) of 49.4 MPa(m)^{1/2} (45ksi (in.)^{1/2}). Crack progression was monitored by measuring upper loading rod deflection, a direct indication of crack opening displacement. Deflection was measured by both a dial indicator gauge and a linear variable differential transformer (LVDT). The LVDT output was recorded on a time base strip chart recorder. Maximum sensitivity was about 0.00025 cm (0.0001 in.) on the dial indicator and 0.0005 cm (0.0002 in.) on the recorder. Both readings agreed within ± 0.005 cm (0.002 in.) over a full scale range of about 1 cm (0.4 in.).

The total time to failure of each specimen was measured from application of the initial test load to final failure (ductile overload). Specimens were subsequently torn open in air and stress corrosion crack propagation lengths were measured. An average crack velocity (crack

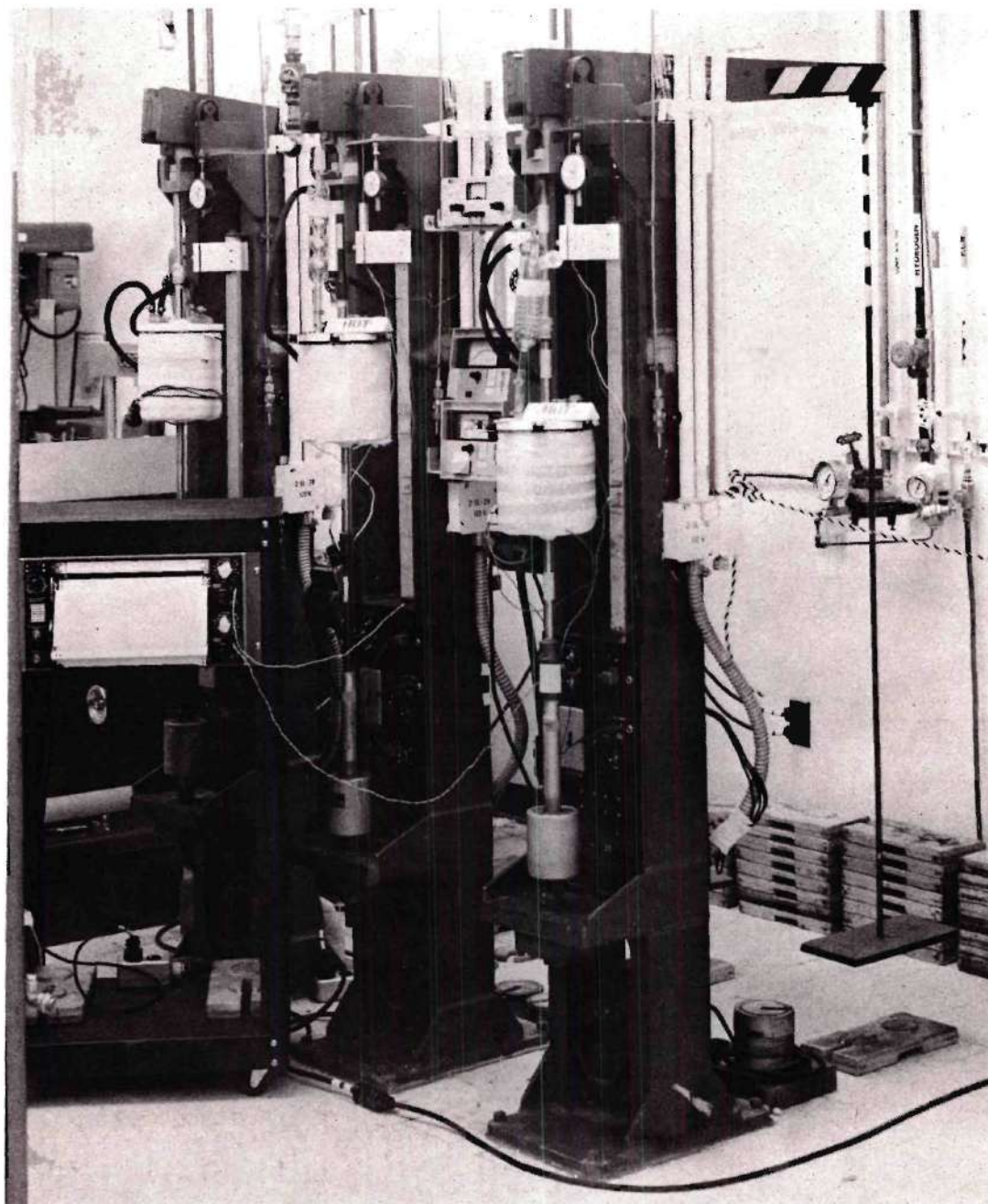


Figure 27. Constant Load Creep Testing Machines Used for Stress Corrosion Studies.

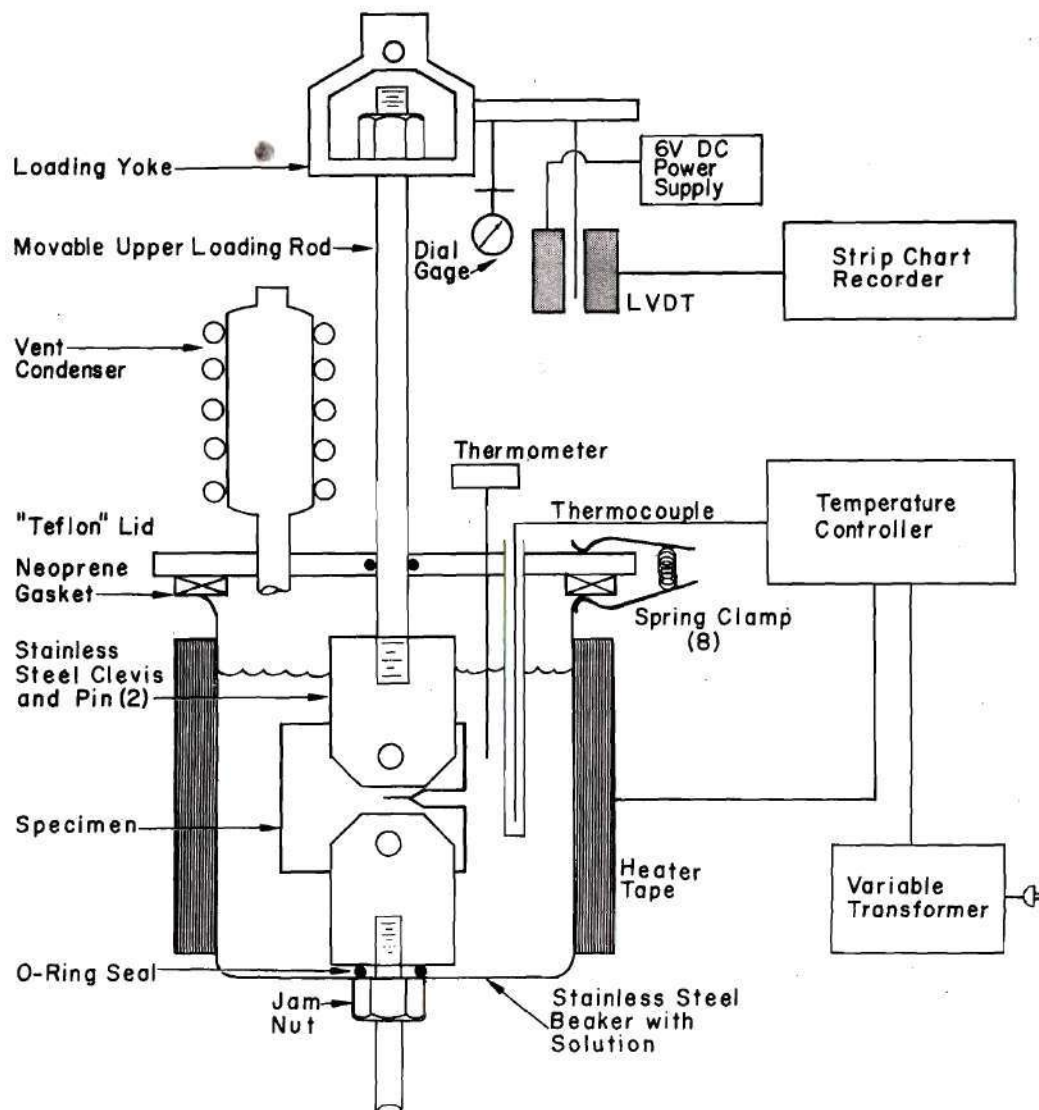


Figure 28. Constant Load Test Cell and Controls.

propagation length by time to failure) was calculated for each specimen. The crack length was measured optically along the specimen notch plane at the thickness centerline and at both specimen sides. A weighted average crack length¹³¹ was used to calculate the average crack velocity.

Transverse sections of cracks and SCC fracture surfaces were examined optically and also by means of an Advanced Metals Research Model 900 Scanning Electron Microscope (SEM).

Compact tension specimens were calibrated to determine the relationship between crack length and crack opening displacement so that instantaneous crack velocities could be calculated. CT specimens of a low yield strength (HR) and a high yield strength (Q) microstructure having different fatigue crack lengths were loaded to the stress corrosion test load in distilled water at 370°K and crack opening displacements were measured. In a given microstructure the crack length-displacement calibration data from these tests and from the initial loadings and ductile overload points in SCC tests were used to establish a graphical calibration of crack length against crack opening displacement. This calibration was used to convert crack opening displacement-time curves from constant load SCC tests into crack length-time curves. Instantaneous crack velocities were then calculated from the slopes of the crack length-time curves. Due to plasticity effects and crack branching during SCC testing, accurate (compliance) calibrations¹³² of CT specimens could not be obtained. Therefore, the calibrations in this study were approximate and were used only to support the validity of average crack velocity as an index of susceptibility to SCC in constant load tests.

Constant Load Test Conditions. Duplicate HR, N, S, Q and QT4 specimens were tested in synthetic H-Purex solution, a hypothetical caustic-nitrate waste solution representing a flow sheet calculation of the composition of the Savannah River Plant H-Area Purex process wastes (Table 4).⁶ The test temperature was 370°K (206°F). Duplicate specimens of the HR and N heat treatments were fabricated in the LT orientation to identify crack plane orientation effects. Duplicate specimens of the Q heat treatment were tempered at 478°K (400°F) for one hour (designated QT4) to examine the influence of low temperature tempering on quenching stresses.

Duplicate CT specimens of the HR, N, Q, HS, NS, QS and QT11 microstructures were tested in a 5M NaNO₃ solution (pH 6.0 ± 0.15)¹³³ at 370°K. This experiment was designed to evaluate the effect of microstructure on cracking in a pure nitrate environment.

Compact tension tests of specimens of the HR, N, S and Q microstructures were also conducted at 370°K in 5M NaNO₃ at pH 13.7. These tests were designed to evaluate the effect of hydroxide addition on cracking in a nitrate environment.

In order to evaluate the effect of temperature on crack velocity, an additional compact tension specimen of the HR microstructure was tested in 5M NaNO₃ solution at pH 6.0 and at 357°K and 345°K (84° and 72°C).

Constant Deflection Tests

Constant Deflection Specimens. Modified wedge-opening-loaded (WOL) fracture specimens of dimension $W = 6.48$ cm (2.55 in.) were utilized in constant deflection cracking experiments (Figure 29).¹³¹ The specimens were fabricated in the TL orientation and after machining were vapor

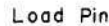


Figure 29. Wedge Opening Loaded Specimen (Reference 131).

degreased in benzene or toluene, wet ground on the sides to a 600 grit finish, ultrasonically cleaned sequentially in distilled water and ethanol, and then air dried. They were fatigue cracked in tension at a frequency of 20 Hz to an initial crack length of about 2.26 cm (0.89 in.) at a maximum stress intensity of $20.8 \text{ MPa(m)}^{\frac{1}{2}}$ ($19.0 \text{ ksi(in.)}^{\frac{1}{2}}$) and minimum stress intensity of $1.3 \text{ MPa(m)}^{\frac{1}{2}}$ ($1.2 \text{ ksi(in.)}^{\frac{1}{2}}$). In most cases the maximum stress intensity during fatigue cracking did not exceed 54% of the initial stress intensity during WOL tests. However, Q specimens had to be fatigue cracked at a higher stress intensity than the other specimens and did not give valid WOL test results.

Constant Deflection Test Equipment and Procedure. Each specimen was loaded to the desired initial load using an Instron Model TT Universal Testing Machine, and crack opening displacement at the initial load was measured with a clip-on, cantilever-type strain gauge.¹³⁰ Specimens were then self-loaded with a bolt and pin to the crack opening displacement at the initial load. The initial load (corresponding to the desired stress intensity factor) was calculated by the relationships

$$K_I = P C_3(a/w) / B \sqrt{a} \quad (5)$$

and

$$C_3(a/w) = 30.96(a/w) - 195.8(a/w)^2 + 730.6(a/w)^3 - 1186.3(a/w)^4 + 754.6(a/w)^5, \quad (6)$$

where " $C_3(a/w)$ " is the finite geometry correction factor and the other

parameters are as in equation (2) and Figure 29.

Specimens were placed in polyethylene bottles which had been radially cut in half, and the specimens were immersed up to the root of the notch in nitrate solution. The bottle halves were then sealed together with commercial masking tape and were partially immersed in a controlled temperature steam bath at 368°K (95°C). Each bottle was vented through a vent condenser to a location outside the steam bath.

Wedge opening loaded specimens were withdrawn from the solution and crack lengths were measured optically approximately every 100 hours. As the cracks grew, the stress intensity factor, K , decreased.¹³¹ Cracks slowed as they approached a final length arbitrarily determined to be that length which was measured after 1500 hours unless further growth was apparent during the preceeding 100 hour interval. The final (crack arrest) K , denoted K_{scc} , was calculated from the initial stress intensity, initial and final crack lengths and a published calibration curve.¹³¹ Crack velocities were determined from the slopes of smooth curves drawn through crack length-time data. Specimens were fractured open in air and crack lengths were measured. A weighted average final crack length was calculated from crack lengths measured along the specimen sides and along the thickness centerline.¹³¹

Constant Deflection Test Conditions. One WOL specimen of the HR, N, S and QT11 microstructures was tested in 5M NaNO_3 at pH 6.0; a second specimen of these heat treatments was tested in 5M NaNO_3 at pH 13.7. This procedure was designed to evaluate both the effects of microstructure on nitrate cracking and to examine the influence of solution pH on cracking. Additional tests in 5M NaNO_3 at pH 6.0 were conducted using duplicate

specimens HS, NS, QS, SQ and Q microstructures. All such tests were at 368°K.

In order to determine the temperature dependence of WOL specimen cracking, a hot-rolled WOL specimen was immersed in 5M NaNO_3 solution of pH 6.0 at four different temperatures: 370°K, 357°K, 345°K and 333°K (97°, 84°, 72° and 60°C). Specimens were placed in glass reaction kettles that had ground glass, flanged lids (Figure 30). Ground glass fittings in each lid were connected to a vent condenser and thermometer. The specimen containers were partially immersed in mineral oil baths that were maintained at constant temperature to approximately $\pm 1^\circ\text{K}$ (Figure 31).

Corrosion Experiments

In order to evaluate the corrosion properties of the various steel microstructures, unstressed corrosion specimens were exposed to various nitrate solutions both at open circuit and at controlled potential conditions.

Corrosion Coupon Tests

Two corrosion coupons of the HR, N, S and Q microstructures were immersed in 5M NaNO_3 solutions of pH 6.0 and 368°K (95°C) in order to determine the influence of microstructure on intergranular penetration of nitrate solutions into unstressed steel. Specimens were 2.54 x 2.54 x 0.32 cm (1 x 1 x 1/8 in.) wafers that were wet ground on all sides to a 600 grit finish. After 500 hours of exposure the specimens were examined metallographically for intergranular corrosion.

Electrochemical Polarization Tests

The potentiodynamic polarization of A 516 Grade 70 steel electrodes having various microstructures was examined using a technique similar to a

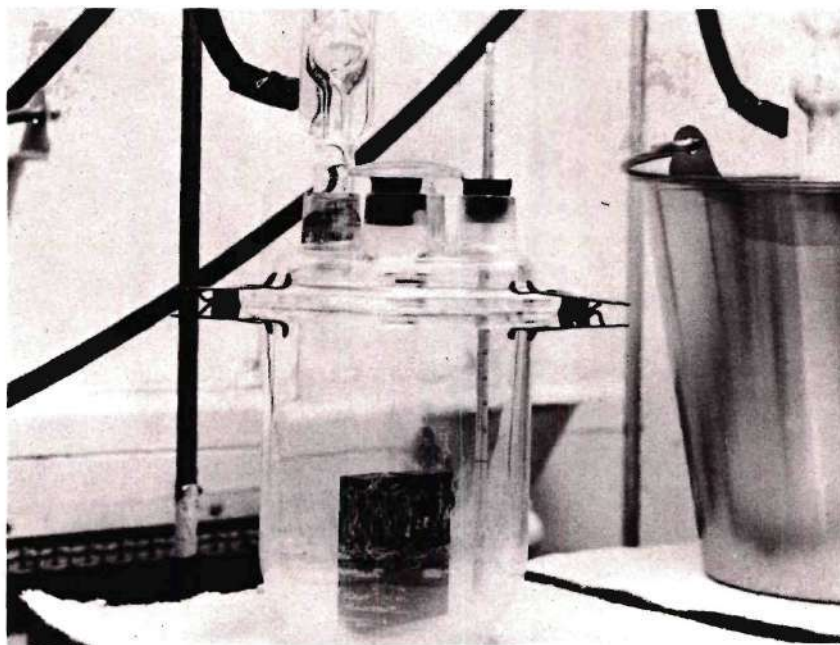


Figure 30. Pyrex Reaction Kettle with Flanged Lid.



Figure 31. Temperature Regulated Oil Baths.

standard method.¹³⁴ The technique utilized the test material as one electrode (working electrode) in a electrolytic cell; the other current-carrying electrode (the auxiliary electrode) was a noble metal (Figure 32).¹³⁵ The potential at the surface of the test electrode was varied by passing current through the solution between the working electrode and auxiliary electrode (Figure 33). The current and potential were plotted on a recorder and gave a graphic representation of the current flow through the various microstructures (e.g., corrosion rate) at any given potential.

Polarization Test Specimens. The test electrodes were 1.27 cm (0.5 in.) length and 0.635 cm (0.25 in.) diameter steel cylinders which were fabricated after heat treatment and were drilled and tapped to accept a mounting rod. Prior to immersion in the test solution each specimen was mounted on the threaded portion of a bolt and was rotated at high speed using an electric drill. The specimen was wet ground successively with 240 and 600 grit abrasive papers while rotating. Next, the specimen was vapor degreased in toluene, rinsed in distilled water and air dried. It was then immediately immersed in the test solution.

Polarization Test Equipment and Procedure. The polarization test cell was of a standard design (Figure 32).¹³⁵ The test cell was heated with a mantle and was vented through a condenser. Two auxiliary electrodes were used (that were electrically connected in parallel); each was a hollow cylinder of platinized platinum¹³⁴ that was suspended on a platinum wire.

Voltage measurements were made using a saturated calomel reference electrode (Figure 33) that was immersed in test solution at room temperature.

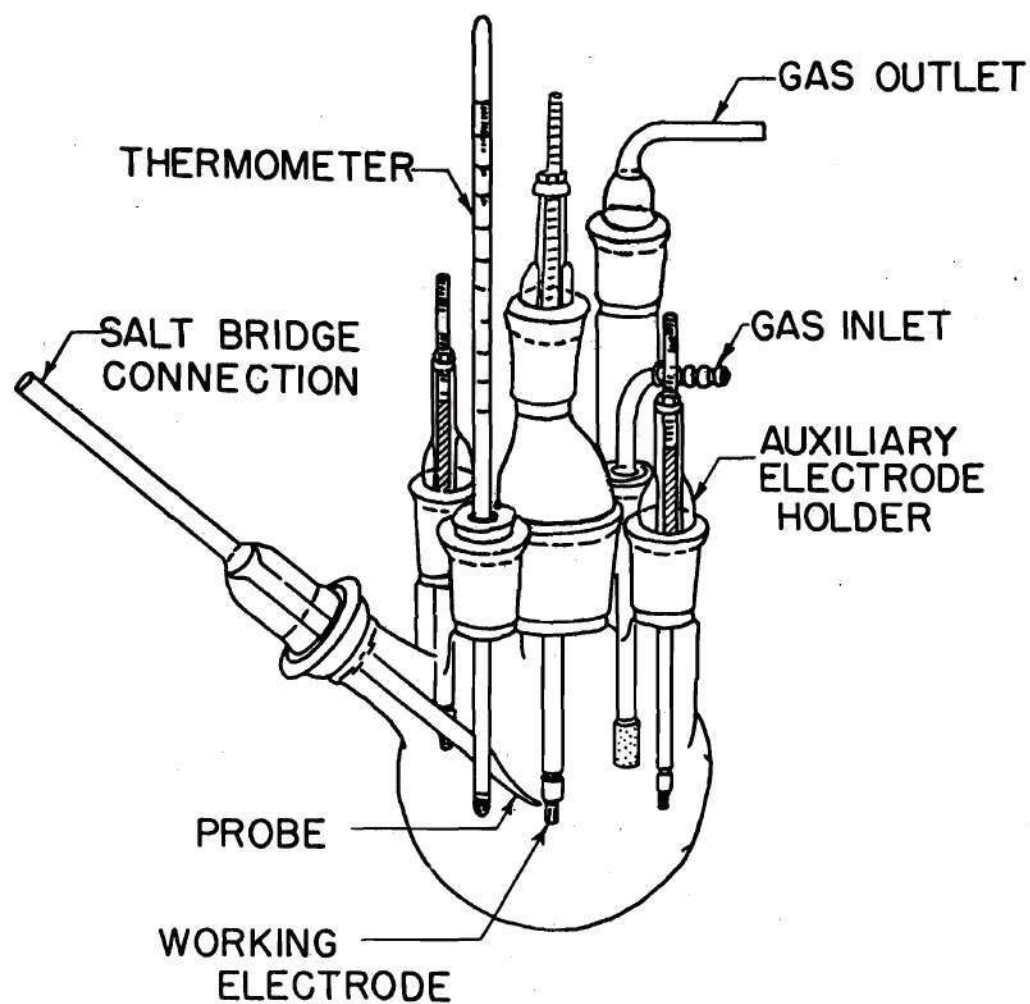


Figure 32. Electrochemical Polarization Test Cell (Reference 135).

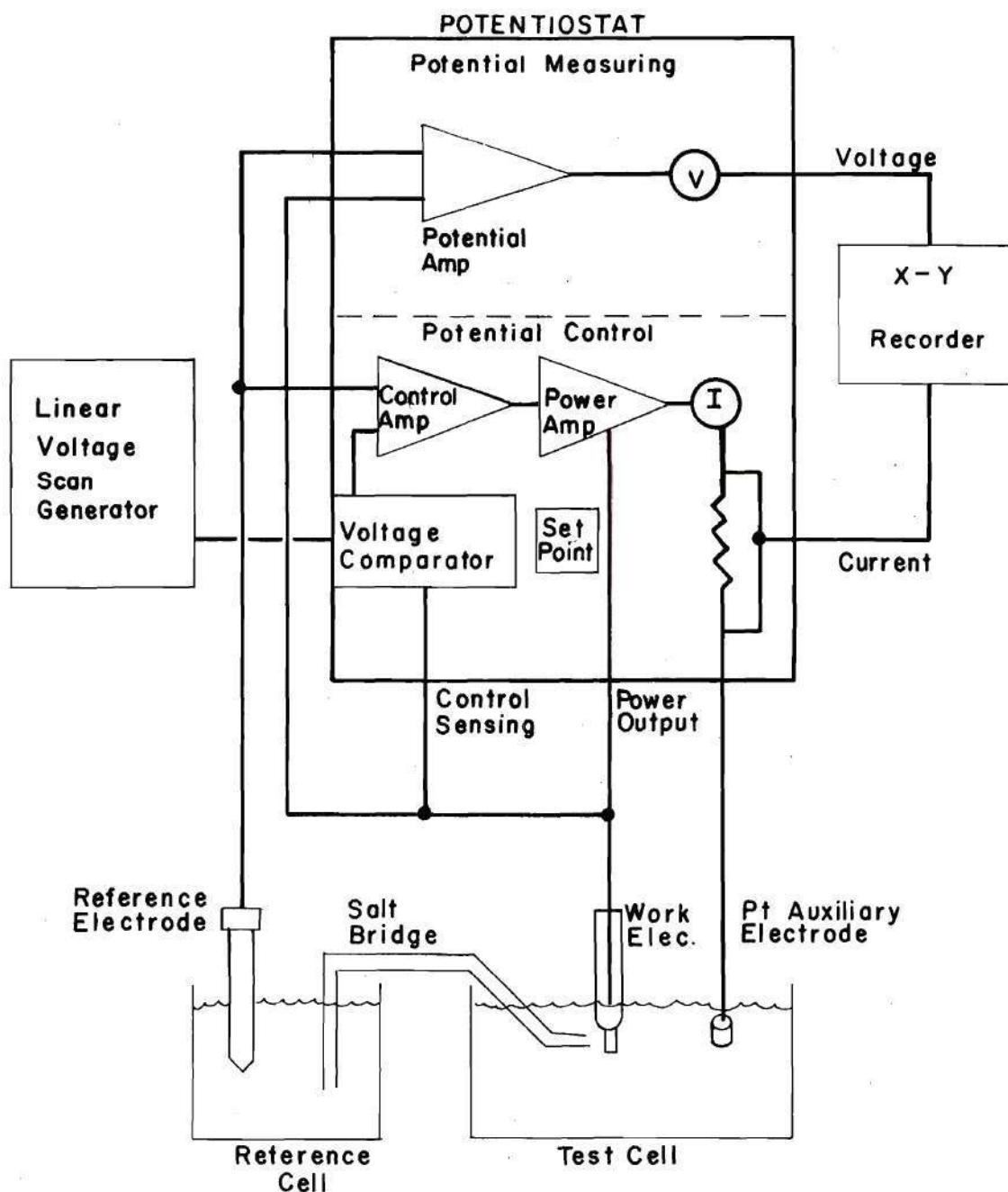


Figure 33. Polarization Experiment Schematic Diagram.

A TRW Instruments Model 200A Research Potentiostat was used for polarization control. A linear voltage scan of 10 mV/min was obtained using a TRW Instruments Model 202A Linear Scan Unit. Voltage and current were recorded on a Houston Instruments (Division of Bausch & Lomb) Model 2000 Omnigraphic X-Y Recorder.

Polarization experiments were conducted by initially filling the test cell with solution and heating to test temperature. Helium purging gas was continually bubbled through the cell at 2000 cm³/min using a perforated tube to deaerate the solution and keep it stirred. Purging was commenced at least two hours prior to the start of testing and was continued throughout the test. After an hour of purging and when the solution reached test temperature, the test electrode surface was prepared and the electrode was immersed in solution. Tests were begun after an hour of specimen immersion and when the open circuit potential of the specimen had stabilized. Anodic polarization scans were started five millivolts cathodic to the open circuit potential and cathodic polarization scans were started a five millivolts anodic to the open circuit potential to accurately define the potential at zero current flow. The voltage and current were continuously recorded as the voltage of the test electrode was continuously increased or decreased in the desired direction. Voltage-current data from the polarization experiments were converted to standard semi-logarithmic voltage-current density plots¹³⁶ by dividing measured currents by the specimen surface area.

Polarization Test Conditions. Polarization experiments were conducted at 370°K using the HR, N, S and Q microstructures in 5M NaNO₃

solutions at pH 3.5, pH 6.0 and pH 13.7. Solution pH was varied to examine the inhibiting effect of hydroxide ion on corrosion in nitrate solutions and to evaluate polarization behavior under possible occluded cell crack tip conditions.^{111,115}

CHAPTER III

EXPERIMENTAL RESULTS

Tensile Tests in Air

Representative stress-strain curves for tensile specimens of various heat treatments are shown in Figures 34-40, and with the accompanying tensile data are summarized in Tables 5-7. Except for cases where a single datum is denoted by an asterisk, values given in the tables are results for duplicate specimens. Most of the microstructures had a definite yield point, but some (e.g., Q) did not. For microstructures that did not have a definite yield point the proportional limit is given in lieu of the lower yield point and the 0.2% offset yield stress is given in lieu of the upper yield stress. Strain hardening parameters were calculated by assuming that the relationship

$$\sigma_T = k \epsilon_T^n \quad (7)$$

describes stress-strain behavior in the work hardening region of the stress-strain curves.¹³⁷ In Equation (7) the terms " σ_T " and " ϵ_T ", the true stress and strain, can be shown to be¹³⁸

$$\sigma_T = \sigma(1+\epsilon), \quad (8)$$

$$\epsilon_T = \ln(1+\epsilon). \quad (9)$$

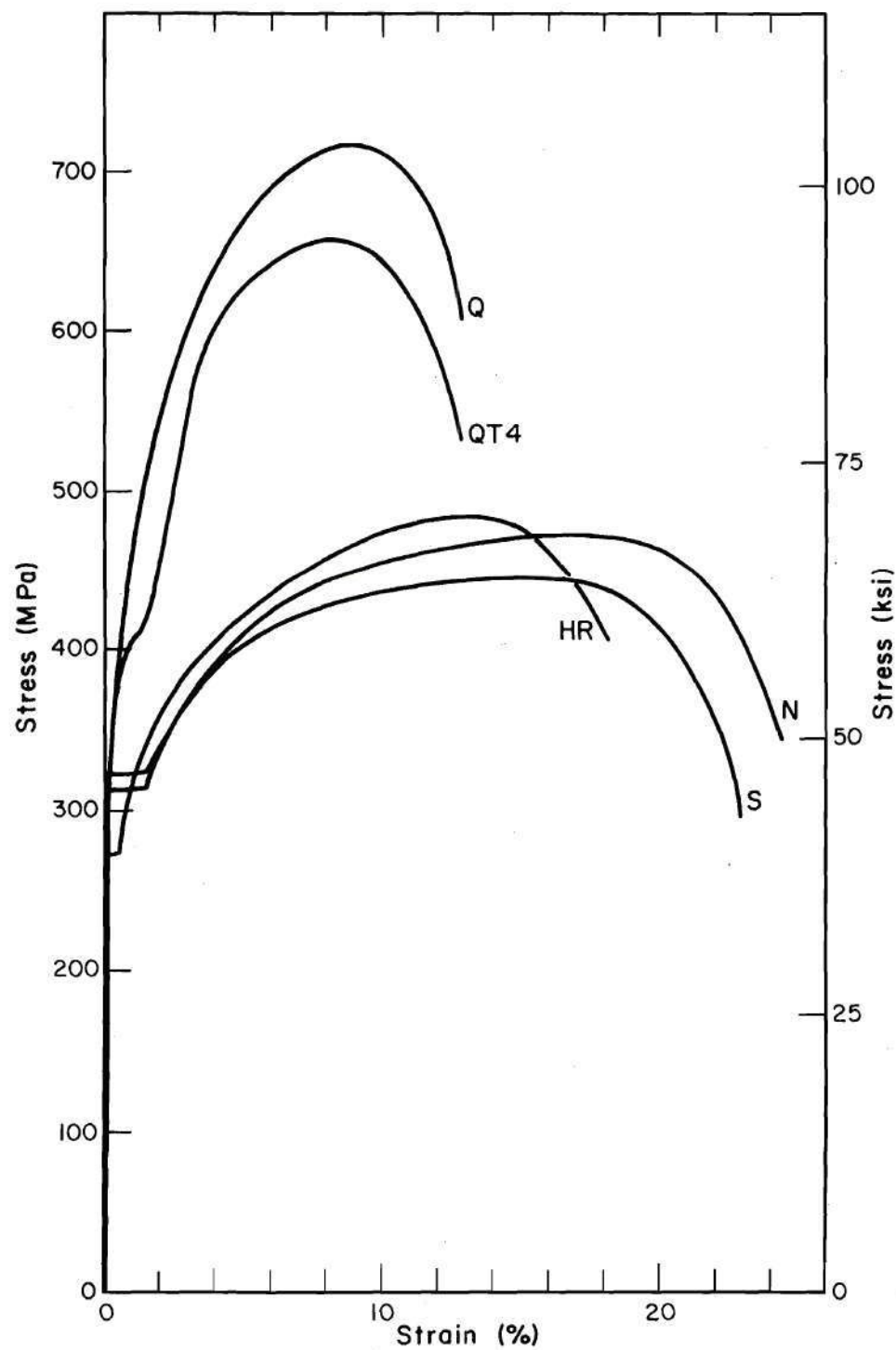


Figure 34. Representative Engineering Stress - Strain Curves at 370°K, $\dot{\epsilon}_0 = 8.3 \times 10^{-5} \text{ s}^{-1}$.

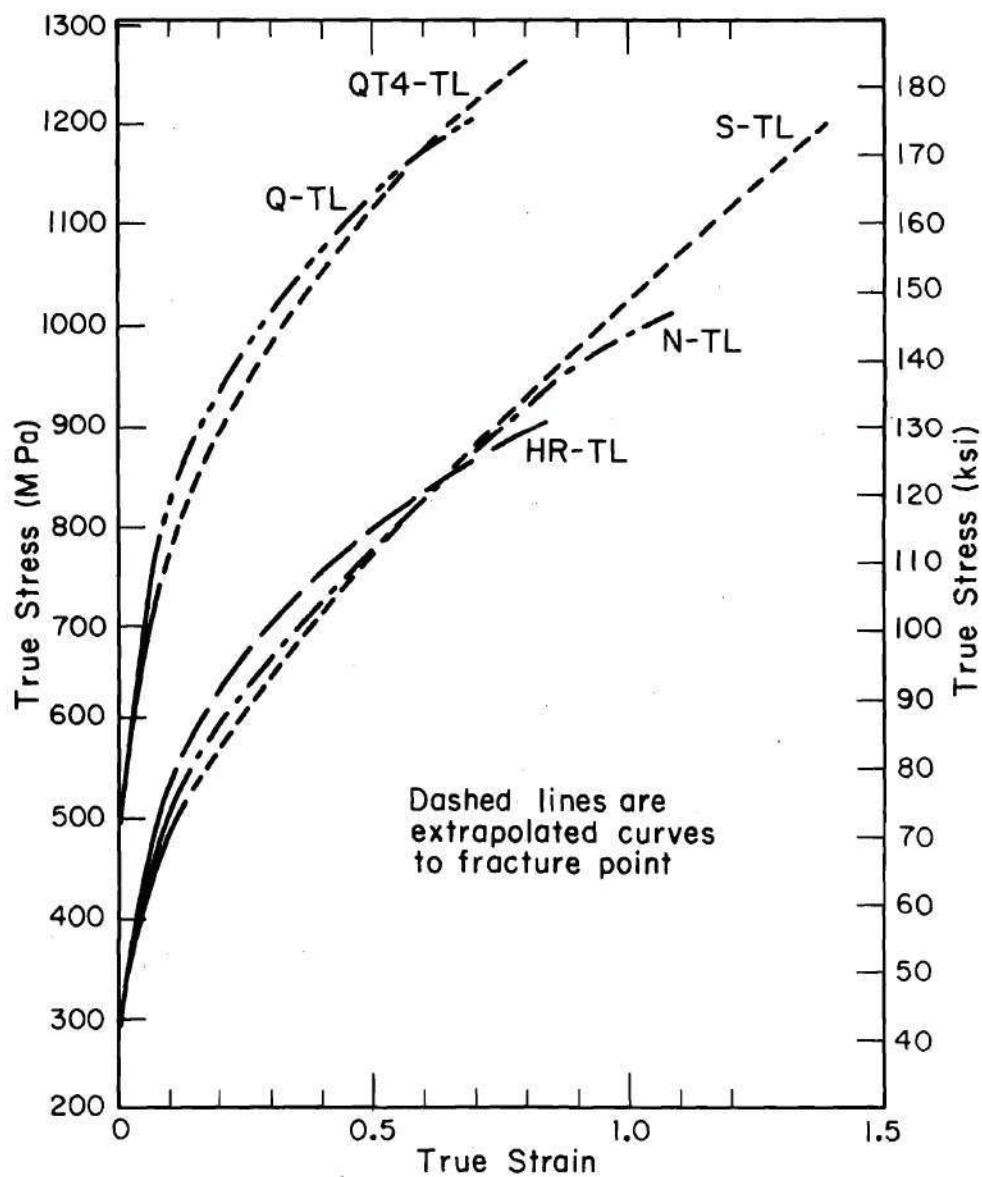


Figure 35. Representative True Stress - True Strain Curves at 370°K $\dot{\epsilon}_0 = 8.3 \times 10^{-5} \text{ s}^{-1}$.

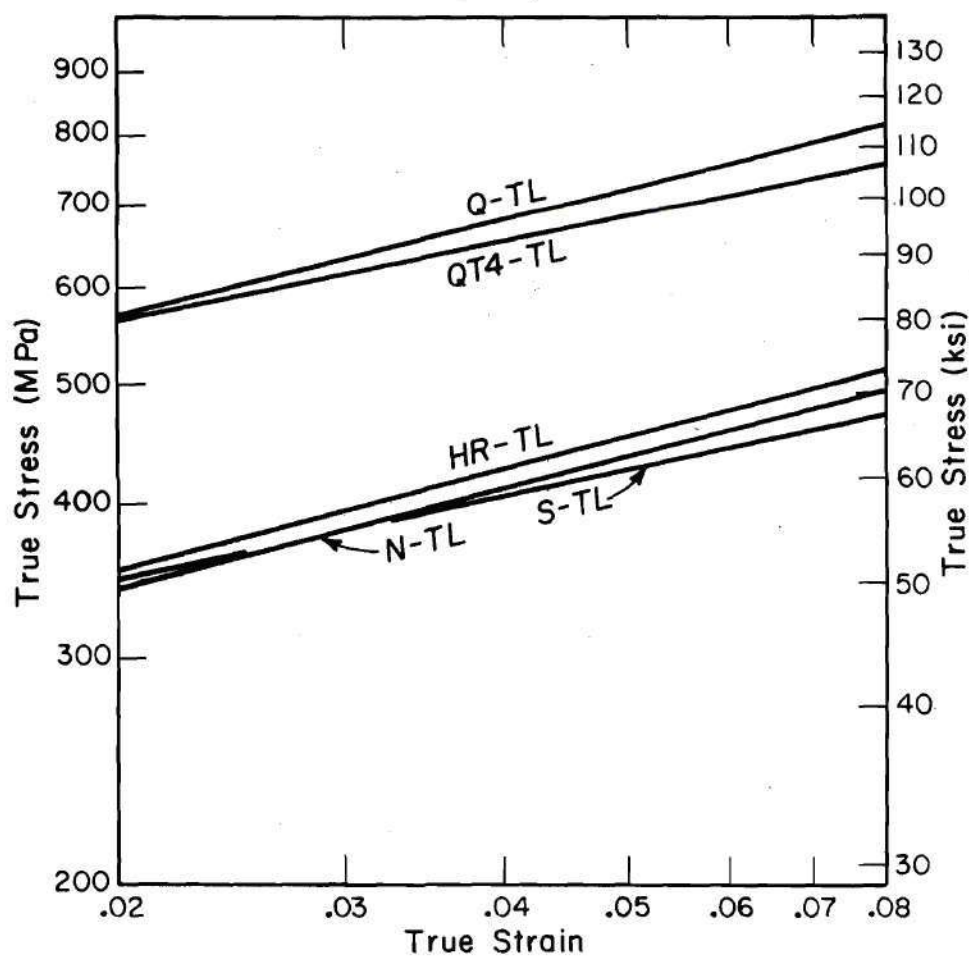


Figure 36. Portion of Log True Stress - Log True Strain Curves at 370°K, $\dot{\epsilon}_0 = 8.3 \times 10^{-5} \text{ s}^{-1}$.

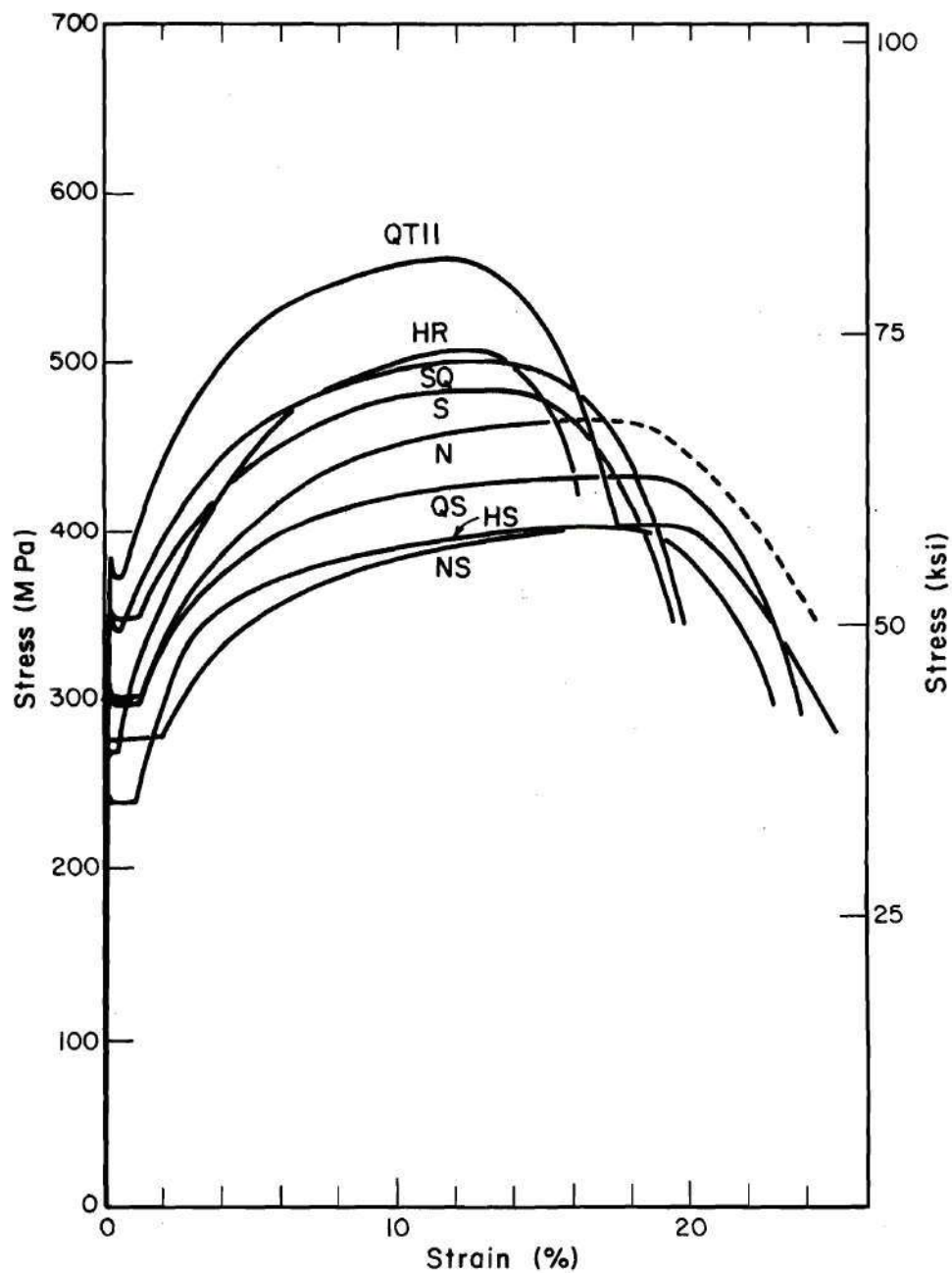


Figure 37. Representative Engineering Stress - Strain Curves at 370°K, $\dot{\epsilon}_0 = 8.3 \times 10^{-6} \text{ s}^{-1}$.

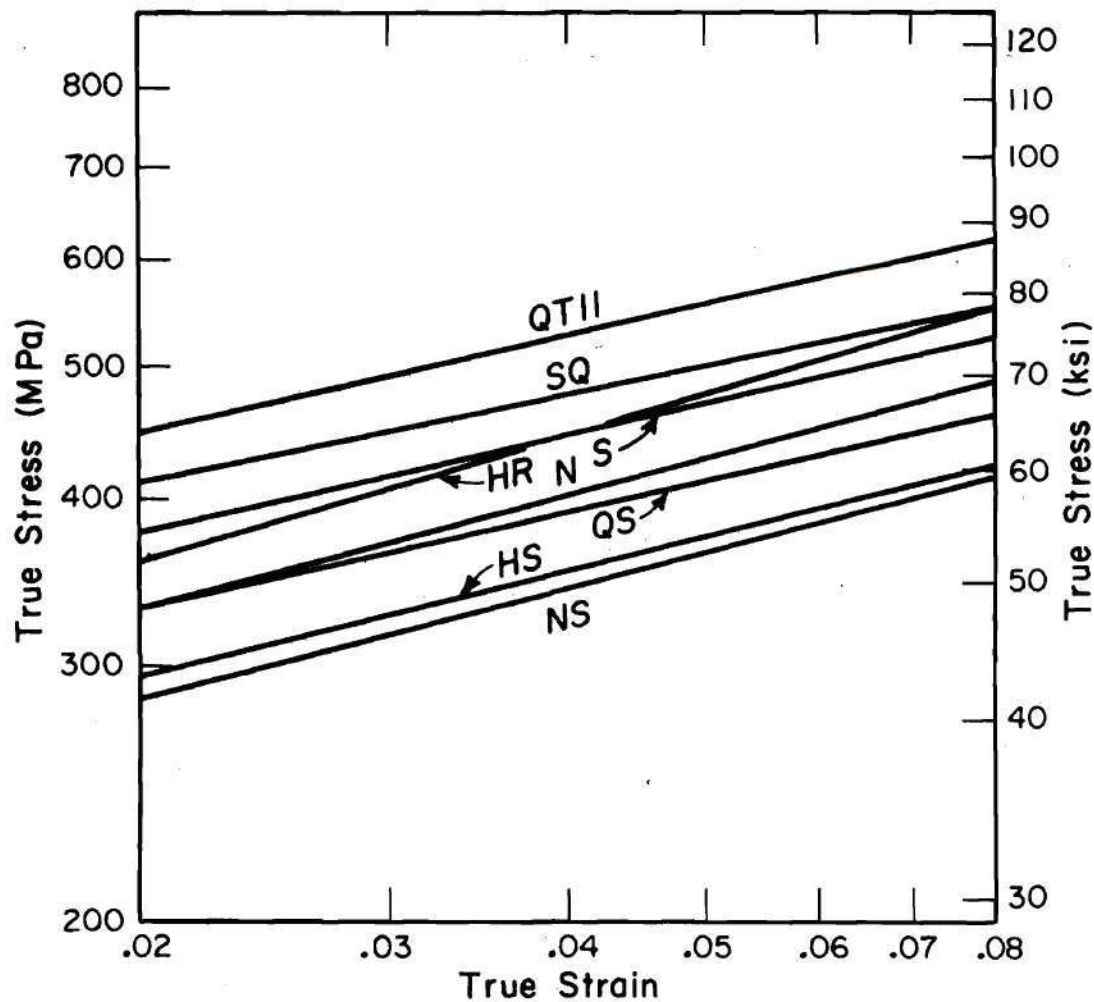


Figure 38. Portion of Log True Stress - Log True Strain Curves at 370°K, $\dot{\epsilon}_0 = 8.3 \times 10^{-6} \text{ s}^{-1}$.

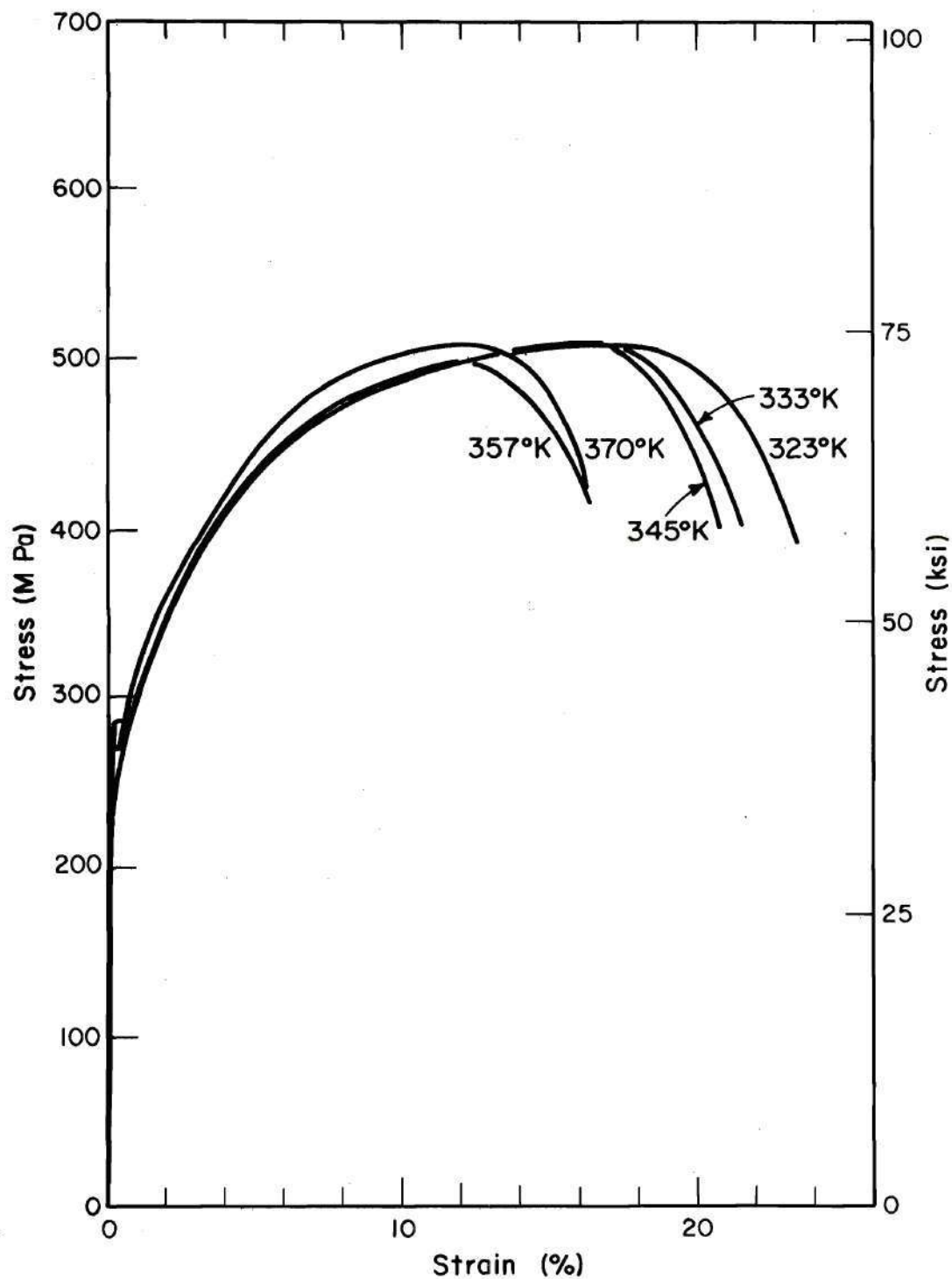


Figure 39. Engineering Stress - Strain Curves for Hot-Rolled Steel at $\dot{\epsilon}_0 = 8.3 \times 10^{-6} \text{ s}^{-1}$, Various Temperatures.

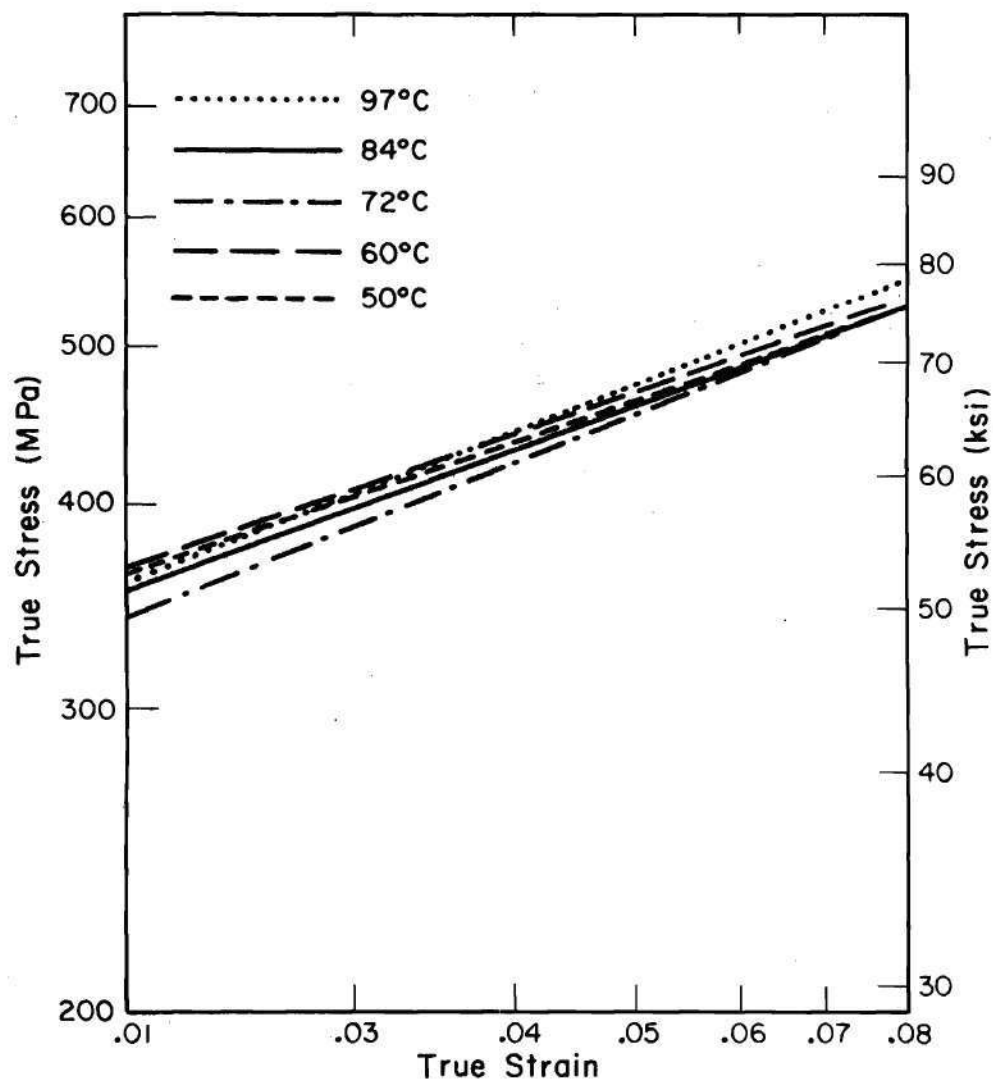


Figure 40. Portion of Log True Stress - Log True Strain Curves for Hot-Rolled Steel at $\dot{\epsilon}_0 = 8.3 \times 10^{-6} \text{ s}^{-1}$, Various Temperatures

In Equation (7) "k" represents the strength coefficient; "n" is the strain hardening exponent, which can be shown to be the true strain at necking.

The as-received, hot-rolled, HR, structure had a lower yield strength and lower ductility than the normalized, N, structure (Figures 34 and 37). This may result from the larger grain size of the HR structure (Figures 12 and 13). However, since increasing grain size causes lower strengths and ductilities and smaller strain hardening exponents,¹³⁹ the relatively large strain hardening exponent and ultimate strength of the HR structure compared to the N structure must be due to influences other than grain size (perhaps related to deformation from hot rolling).

There was no significant effect of orientation on tensile behavior (Table 5) in either HR material or N material. Metallographic examination of these materials confirmed such isotropy by showing no difference in grain structure between transverse or longitudinal sections.

The tensile properties of the spheroidized structure, S, closely resembled those the normalized structure, but the S structure had a somewhat higher yield strength. Quenching the spheroidized structure, SQ, raised the strength. The quenched structure, Q, was considerably stronger and less ductile than the others (Figure 33). This resulted from its martensitic or bainitic components. The quenched specimens showed no definite yield point; this indicated the presence of unpinned dislocations.¹³⁷ Tempering the Q structure for one hour at 478°K (400°F), the QT4 structure, lowered the strength and produced an inflection in the stress-strain curve (indipient yield point) just above the proportional

limit (Figure 34). Tempering the quenched material at 478°K caused a moderate reduction in strength but little change in ductility (Figure 34 and Table 5). Tempering the quenched material for one hour at 866°K (1100°F), the QT11 structure, reduced the tensile strength and increased the ductility (Figures 34, 37 and Tables 5, 6). Tempering at 866°K also produced a well-defined yield point (Figure 37).

The coarsely spheroidized structures, HS, NS and QS, had some of the highest ductilities and lowest yield strengths of all the structures studied. The respective yield points of these three structures decreased with increasing ferrite grain size as expected from Equation (1).

The temperature dependence of the tensile properties of hot-rolled steel in the range 323°-370°K is shown in Figure 39 and Table 7. There was a distinct reduction in ductility and a small, systematic decrease in lower yield stress with increasing temperature. These changes in tensile properties were quite small compared to the large increases in strength with increasing temperature which may occur in mild steels tested in certain temperature ranges.¹⁴⁰ Such increases in strength are thought to result from interstitial atom-dislocation interactions. Most of the structures showed some degree of serrated yielding, the so-called Portevin-le Chatelier effect (due to interstitial atom-dislocation interactions).¹³⁷ The two test temperatures which resulted in markedly lowered ductility, 370°K and 357°K (Figure 39), represented test conditions under which the HR microstructures also demonstrated pronounced serrated yielding. This is not surprising; such interstitial atom-dislocation interactions are responsible for embrittlement problems like blue-brittleness in mild steels.¹³⁷

Scanning electron microscopy of fracture surfaces of tensile specimens are shown in Figures 41, 42. Most of the steel microstructures had fracture surfaces that were nearly identical to the ductile rupture fracture mode of as-received HR material (Figure 41). The fracture surfaces of the S and SQ structures were characterized by numerous, small pores that appeared to correspond to the finely spheroidized carbide morphology of these structures (Figure 42). The few, large cavities seen in the micrographs appear in bands across the fracture surface. SEM X-ray fluorescence analysis of chips of material clinging within the large pores revealed that they consisted of manganese and sulfur. This indicates that the large pores are associated with MnS stringers.

Stress Corrosion Cracking Experiments

Constant Load Tests in H-Purex Solution

Specimens of the HR, N, S, Q and QT4 microstructures were tested in synthetic H-Purex solution to gain experience with such tests and to obtain a preliminary evaluation of the influence of heat treatment and microstructure on cracking.

Crack opening displacements of compact tension specimens were measured as a function of time. The displacement-time curves for individual specimens of the various microstructures overlapped extensively, and each curve appeared to be more unique to a particular specimen than representative of a particular microstructure. Therefore average displacement-time curves for each microstructure were plotted with the ranges in time to failure shown by error bars (Figure 43). Since linear scale displacement-time curves had continually increasing slopes and

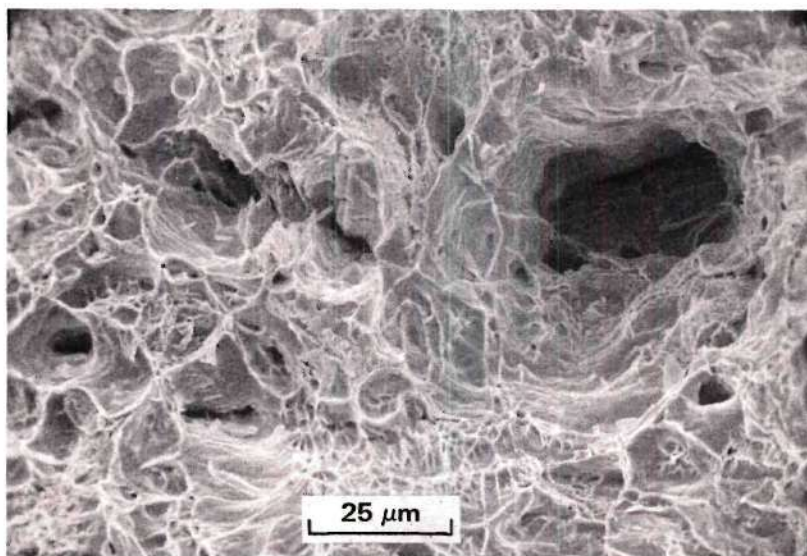


Figure 41. Fracture Surface of HR Tensile Specimen.

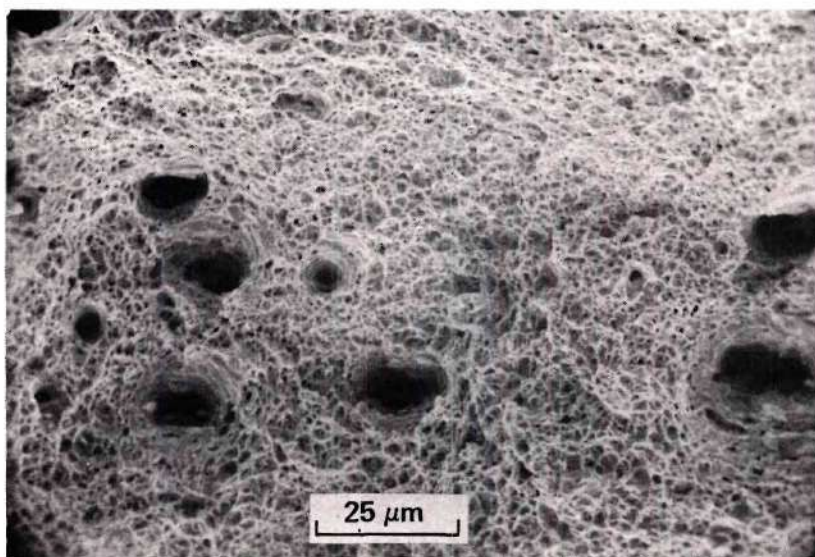


Figure 42. Fracture Surface of S Tensile Specimen.

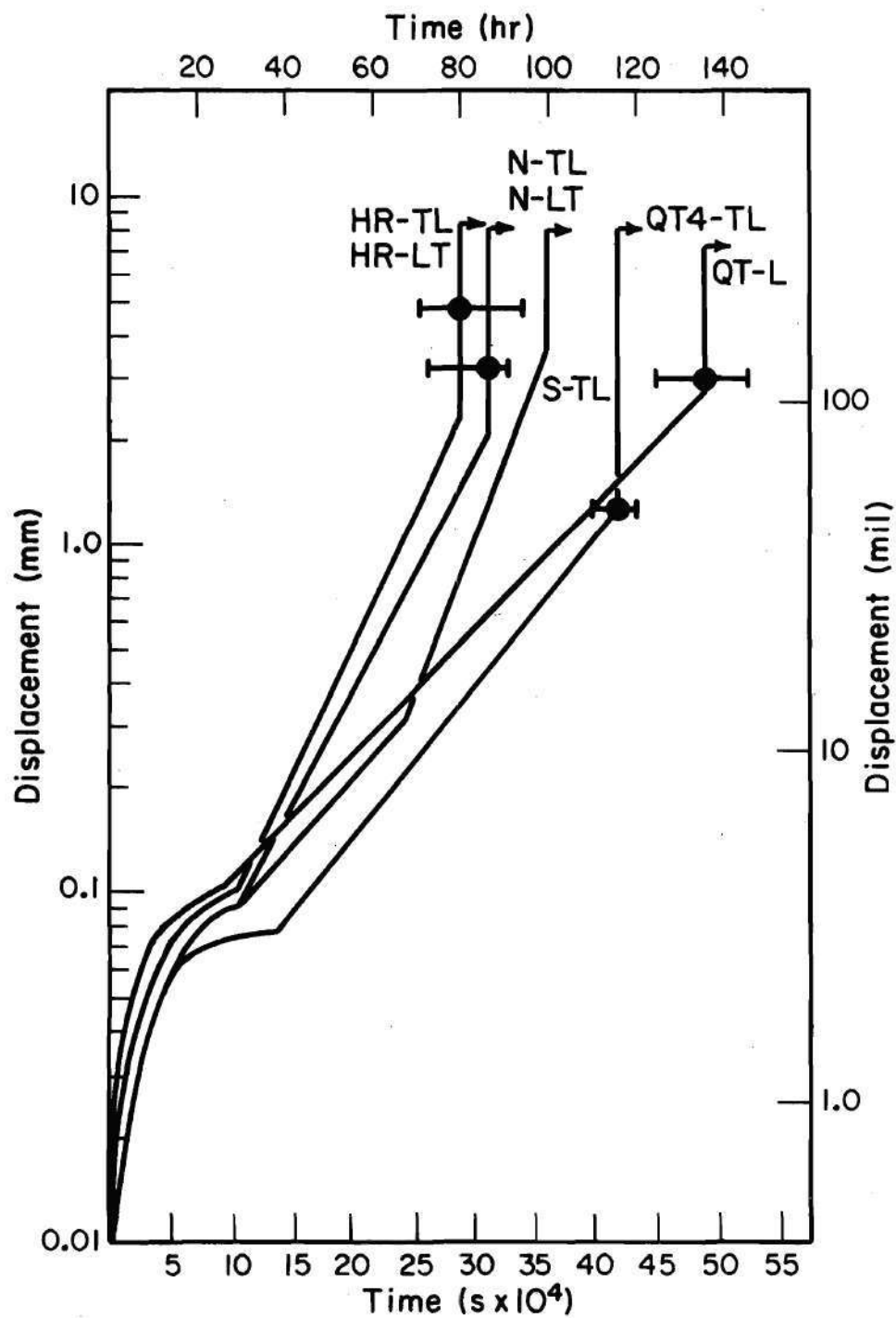


Figure 43. Crack Opening Displacement of CT Specimens in H-Purex at 370°K, $K_I = 49.4 \text{ MPa (m)}^{1/2}$.

were difficult to compare, the curves in Figure 43 were plotted on a semi-logarithmic scale for ease of comparison.

The rapid initial rise in crack opening displacement during the first several hours of testing was due to plastic relaxation of the specimen (microstrain¹³⁷) and occurred in inert environments (distilled water) as well (Figure 43). Extrapolation of the linear portions of the curves back to small displacements indicated that crack initiation times were small and insignificant compared to the times to failure. However, plastic relaxation obscured initial crack growth and prevented accurate determination of the crack initiation time.

Time to failure was measured from the time of load application to the time of specimen overload. At overload the specimens underwent a sudden, large increase in crack opening displacement (vertical lines in Figure 43) and emitted a popping noise. At this time the applied load was partially relieved as the load pan came to rest against a mechanical stop. Time to failure of individual specimens are given in Table 8 and averages are plotted as a function of yield strength in Figure 44 (error bars indicate range between individual specimens). There appeared to be a correlation between susceptibility to cracking as measured by time to failure and the upper yield point (or proportional limit where applicable) of the various microstructures (Figure 44). However, there was considerable scatter time to failure data for duplicate specimens. Furthermore, time to failure data could bias the measurement of relative susceptibilities. High strength microstructures might crack farther before reaching ductile overload, and these microstructures would seem less susceptible than low strength microstructures having

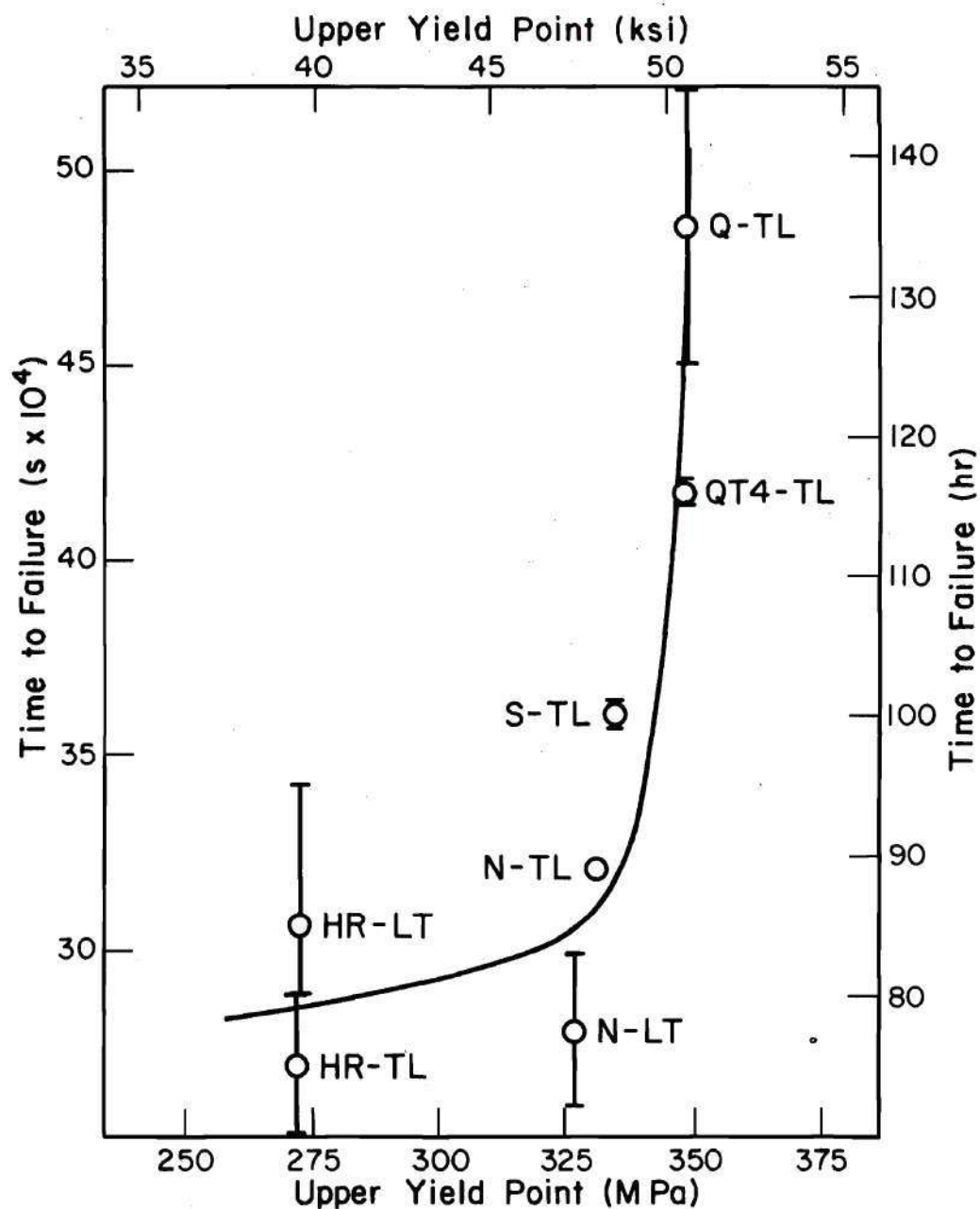


Figure 44. Time to Failure of CT Specimens in H-Purex at 370°K, $K_I = 49.4 \text{ MPa (m)}^{1/2}$.

the same stress corrosion crack propagation rate. Therefore, average crack velocity (stress corrosion crack length divided by time to failure) was used to minimize such bias.

Compact tension specimens tested over 100 hours in synthetic H-Purex solution at 370°K remained bright and shiny on outer surfaces. Therefore no appreciable corrosion occurred in H-Purex. However, all microstructures underwent IG SCC in a branching pattern that initiated near the tip of the fatigue crack (Figure 45). Two main crack branches formed symmetrically about the notch plane. Fine subbranches formed as the main branches propagated. The branching angle between the notch plane and the main crack branches was not constant but decreased rapidly with distance from over $\pi/4$ radians (45°) at the origin of branching to a measured average angle of about $\pi/6$ radians ($30 \pm 6^\circ$) further along the cracks. Because the measured branching angle seemed to be independent of microstructure, and for simplicity of measurement, crack lengths were measured in the plane of the specimen notch. Such a measured crack length is within 15% of the length of a crack lying at $\pi/6$ radians (30°) from the notch plane.

Stress corroded CT specimens were subsequently fractured open in air for measuring crack lengths and conducting fractography. A typical CT specimen fracture surface revealed (from right to left in Figure 46) a fatigue crack (light area), stress corrosion crack (dark area), ductile overload fracture (light area), a reinitiated stress corrosion crack (dark area) and another ductile fracture surface (light area, broken in air). The chronological development of these features was:

- (1) a fatigue crack was mechanically introduced in air,

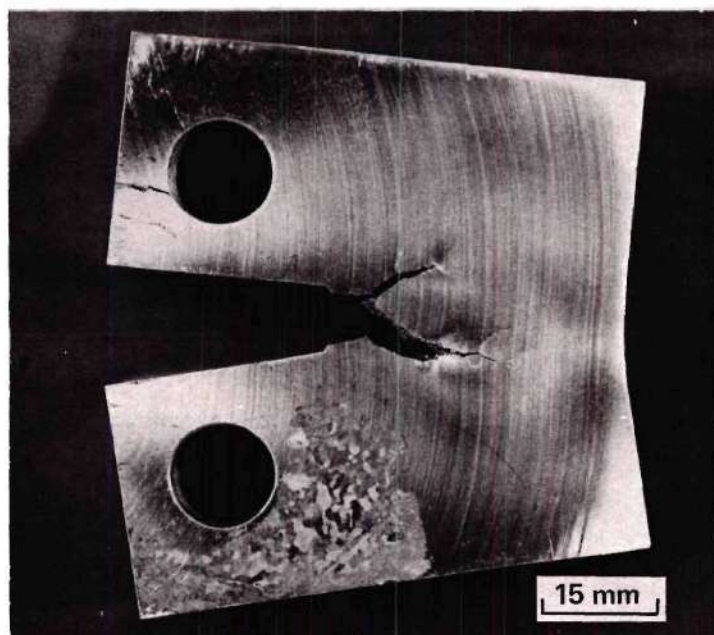


Figure 45. Crack Branching in CT Specimen.

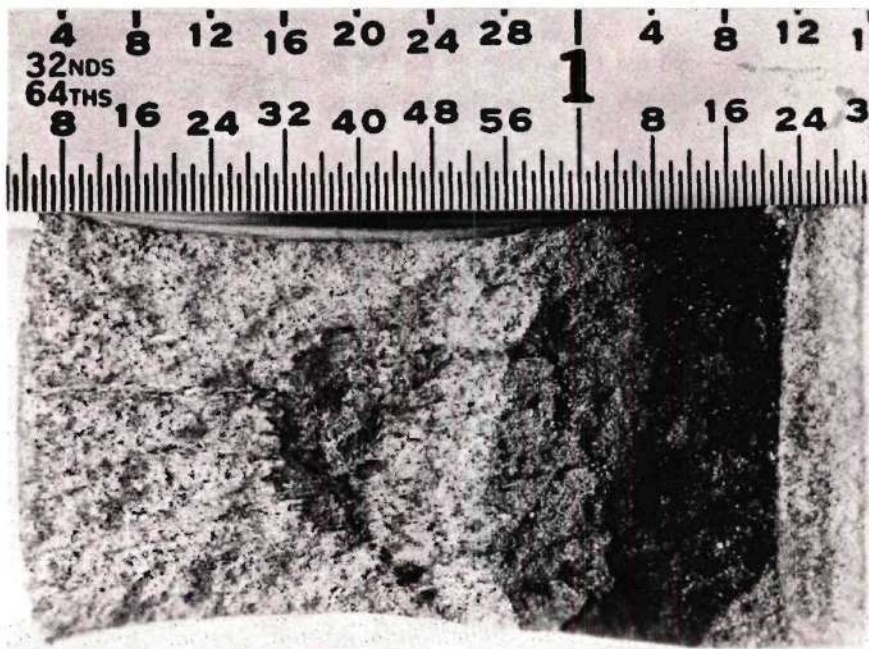


Figure 46. Fracture Surface of CT Specimen Showing Various Regions (Right to Left): Fatigue, SCC, Ductile Overload, SCC Reinitiation, Air Fracture.

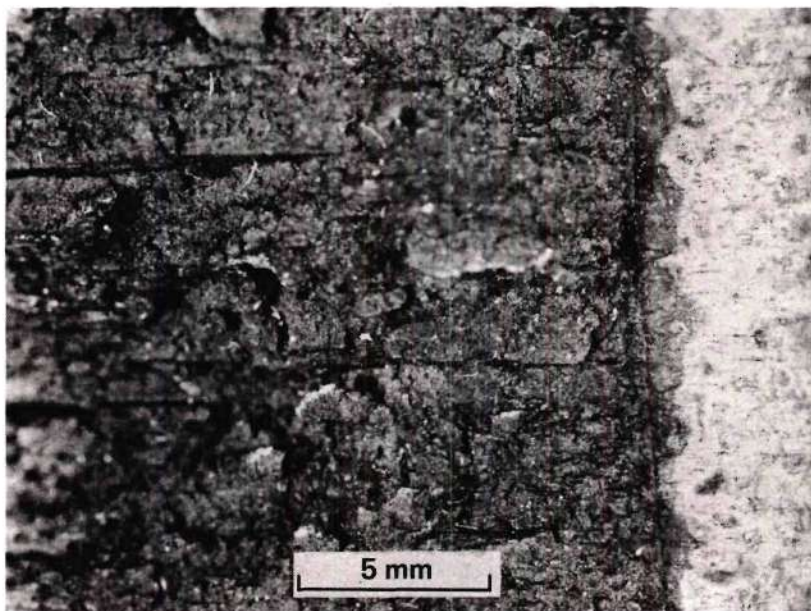


Figure 47. Closeup of CT Specimen SCC Fracture Surface.

- (2) a stress corrosion crack (IG, oxide-covered fracture surface) propagated in H-Purex to the point of ductile overload,
- (3) the overloaded specimen failed by ductile fracture in solution and partially released the applied load as the load pan contacted a mechanical stop,
- (4) IG SCC reinitiated, and
- (5) the specimen was removed from solution and was completely torn open in air on a tensile test machine.

A close up view of a typical stress corrosion fracture surface is shown in Figure 47. The fracture surface revealed crack branching (vertical line in Figure 47) and also delaminations (horizontal lines) perpendicular to the fracture surface that appeared to be associated with bands of sulfide stringers in the material. The transition from the fatigue crack to the SCC fracture was abrupt and did not indicate sub-critical crack growth by a purely mechanical mechanism during initial plastic relaxation of specimens.

Intergranular features of the stress corrosion fracture surface were generally obscured by a thick, grey-black surface film (Figure 48). The film was identified as magnetite, Fe_3O_4 , by the Debye-Scheerer technique of X-ray diffraction.¹⁴² Sample d-spacings and relative diffraction line intensities are listed in Table 9.

A narrow region at the tip of stress corrosion fracture surfaces was relatively film-free and had recognizable IG facets (Figure 49). This region was adjacent to the abrupt change to ductile fracture that occurred where the CT specimens reached overload (Figures 46-47). The film-free IG facets apparently occurred where corrosion and film formation

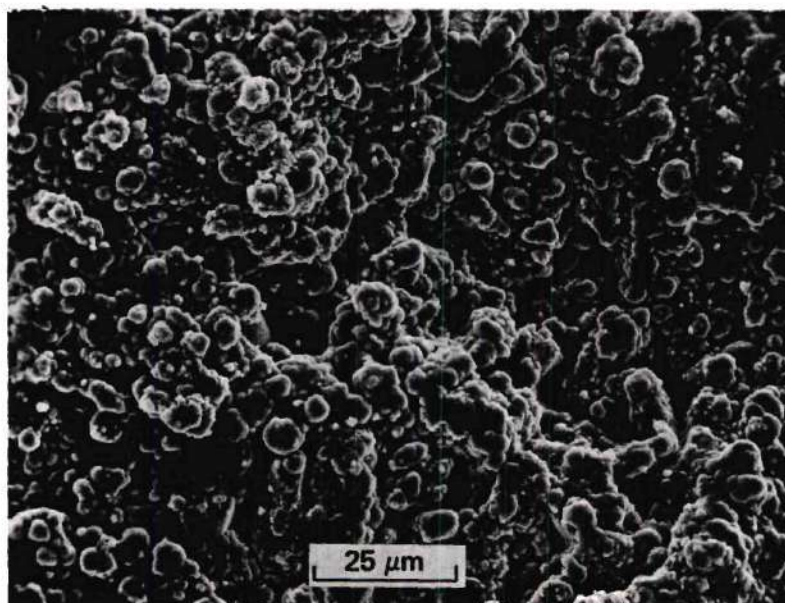


Figure 48. SCC Fracture Surface Obscured by Film.

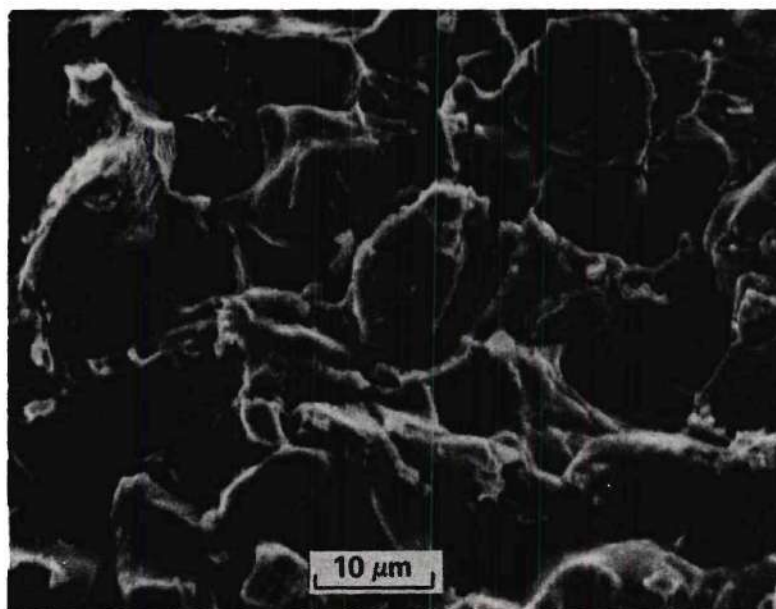


Figure 49. Film-Free, IG SCC Region Near Crack Tip.

proceeded for only a short time before overload. The ductile overload fractures in H-Purex were generally passivated and resembled the fracture surfaces of tensile specimens tested in air (Figures 41-42). These passivated, ductile fracture surfaces indicated that overload and specimen tearing exposed fracture surfaces to H-Purex solution from the bulk medium. This solution passivated the surfaces and inhibited further corrosion.

Compact tension specimens were descaled (in an inhibited sulfuric acid with low pitting properties¹⁴¹) to reveal the IG features of the stress corrosion fracture surface. Descaled SCC fractures in the Q, HR, N and S microstructures are shown in Figures 50-53 respectively. The apparent pitting and surface roughness seemed to result from SCC; the descaling solution did not attack fine surface features such as ductile fracture ridges. The descaled fracture surfaces revealed grain facets (Figures 51-52) previously obscured by the oxide film, and a higher magnification micrograph revealed that rough fracture features consisted of many crystallographic etch pits (Figure 54).

Transverse sections of CT specimens (viewed perpendicular to the specimen sides) revealed the morphology of microcracks that branched off the main fracture surface (Figures 55-56). Narrow grain boundary cracks no more than 0.25 μm wide were seen that were filled with a grey-black material, presumable magnetite (Figure 55). Grain Boundary cracks seemed to propagate randomly along ferrite grain boundaries (such as in hot-rolled steel in Figure 55); there was no apparent cracking along prior austenite grain boundaries as found by Flis and Scully.⁵⁷ While in some areas an apparent preference existed for cracking along ferrite-pearlite

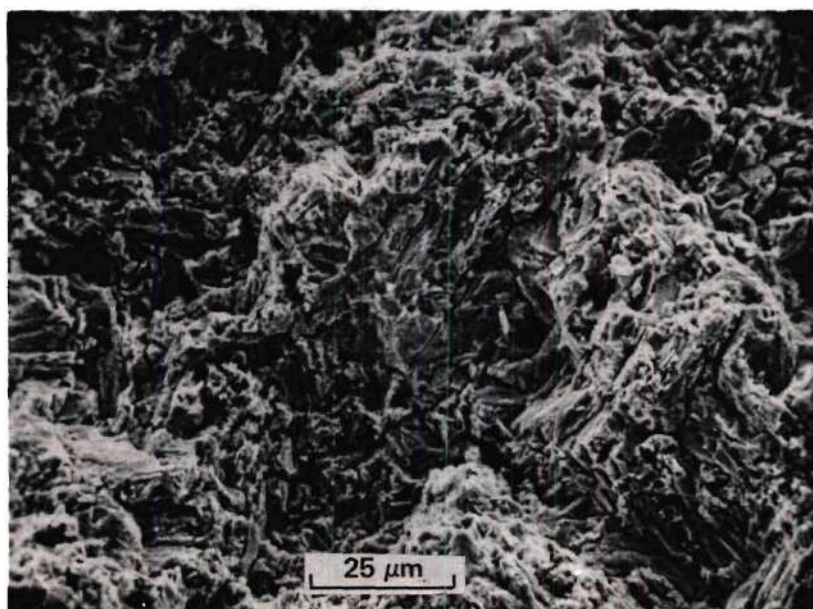


Figure 50. SCC Surface of Q Microstructure After Descaling.

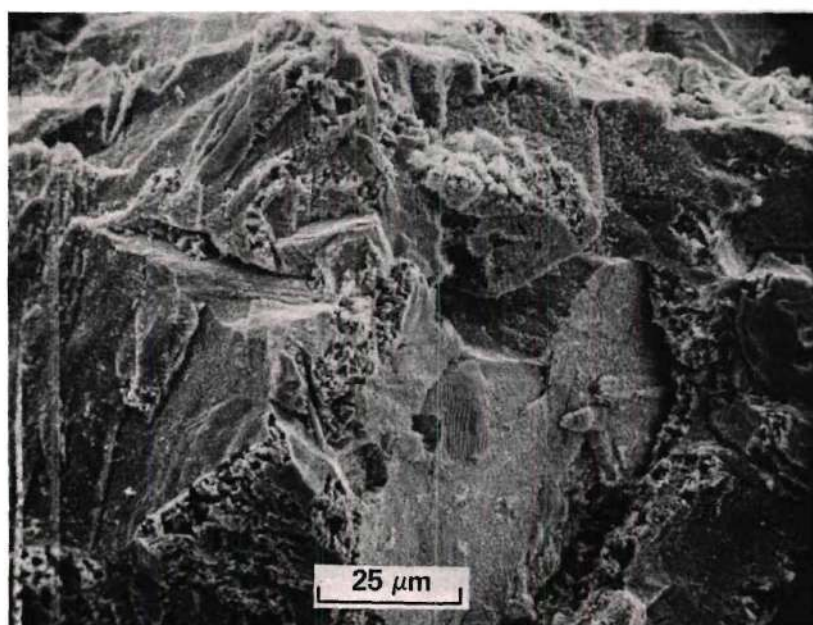


Figure 51. SCC Surface of HR Microstructure After Descaling.

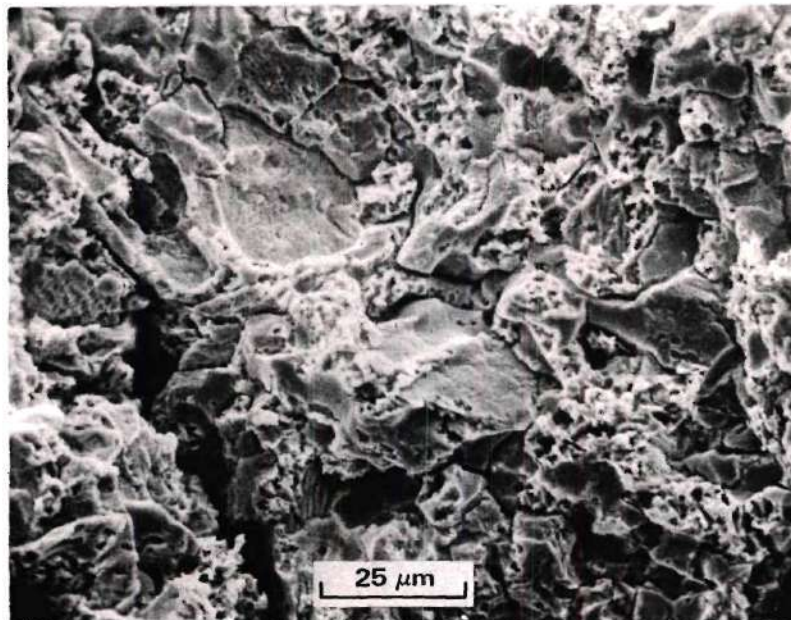


Figure 52. SCC Surface of N Microstructure After Descaling.

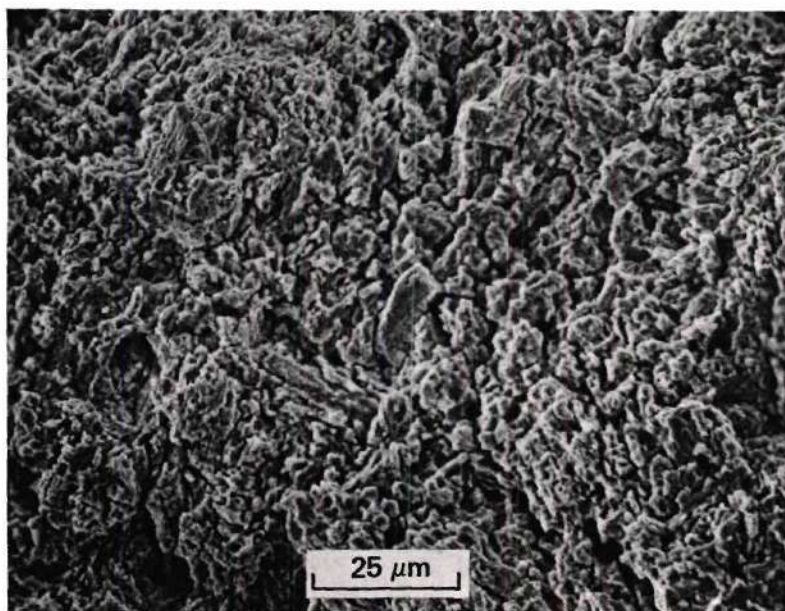


Figure 53. SCC Surface of S Microstructure After Descaling.

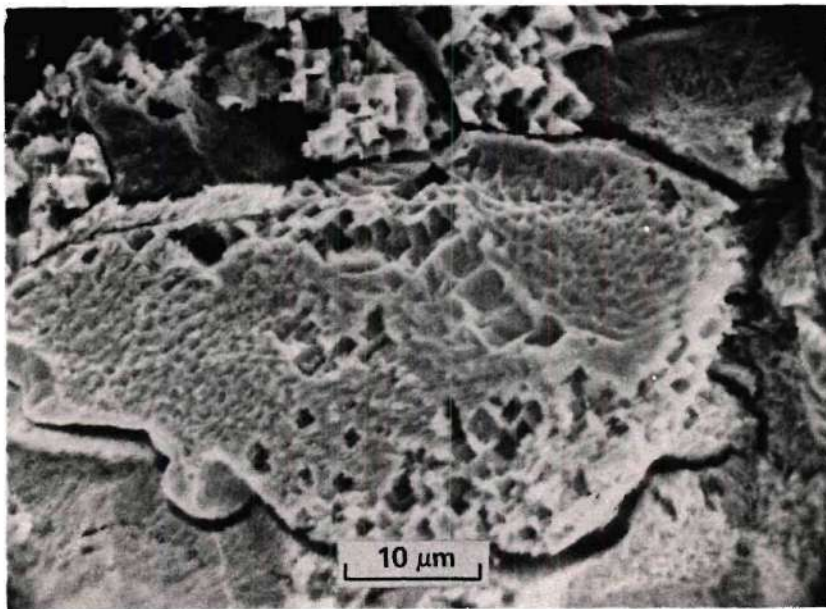


Figure 54. Pitting on Descaled SCC Fracture Surface.

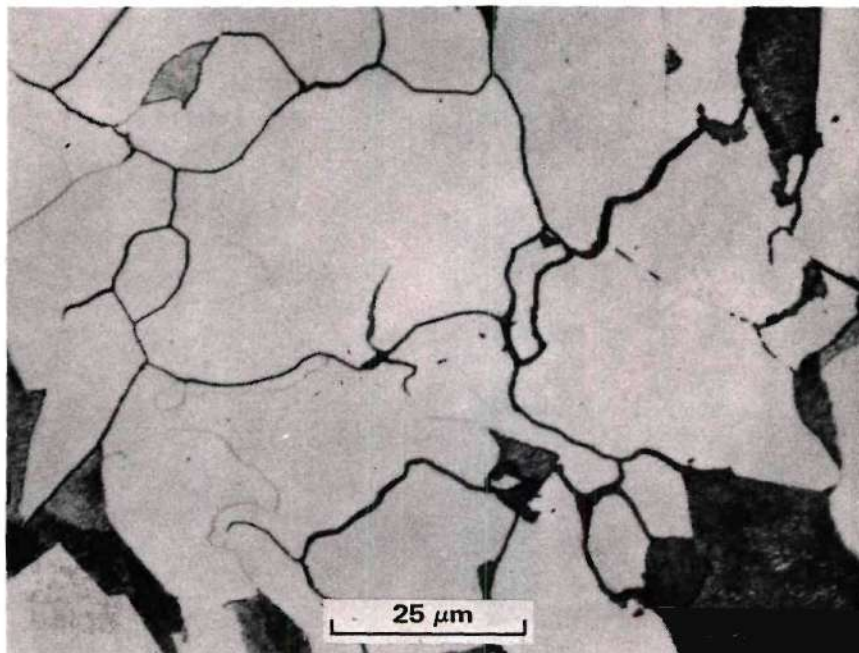


Figure 55. Cracks in Ferrite Grain Boundaries in HR Structure.

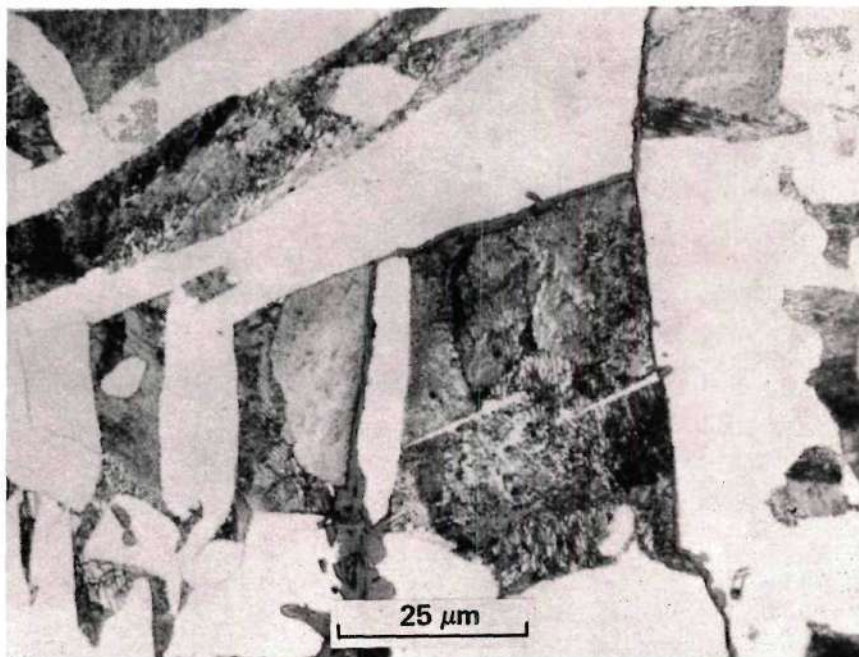


Figure 56. Cracks Outlining Pearlite Colonies in HR Structure.

interfaces and cracks seemed to outline pearlite colonies (Figure 56), in other areas there were cracks that propagated across individual pearlite colonies. However, most cracks seemed to propagate around pearlite rather than to penetrate it. Evidence of cubic etch pits could be seen in the grain boundary cracks (Figures 55, 56).

Stress corrosion cracks were reinitiated after a CT specimen reached overload. Upon failure of a CT specimen by ductile fracture, the load pan came to rest against a mechanical stop. Therefore, the applied load decreased. The residual load remaining on the specimen often caused stress corrosion to reinitiate. The reinitiated stress corrosion fracture surfaces appeared identical to the stress corrosion cracking that occurred before ductile failure. A similar grey-black surface film was formed (Figure 46). The appearance of this filmed region was much different than the shiny, ductile overload region that was intermediate between the two SCC regions (Figure 46). The ductile overload region apparently was exposed to bulk solution conditions that were noncorrosive. It appeared that conditions within a caustic-nitrate stress corrosion crack which were conducive to magnetite formation were decidedly different. Additionally, SCC reinitiation was accompanied by a progressive darkening of the ductile rupture surface and a change in film color from reddish gold to blue-black to grey-black, indicating a gradual thickening of oxide and a gradual change in surface conditions toward those favoring bulk magnetite formation.

Estimates of incubation time were made by plotting the measured reinitiated SCC length against the time between ductile overload and removal of load weights. Extrapolation of the data to the origin

indicated a two to five hour incubation time, about the same length of time that CT specimens remained in solution during warmup before initial loading was commenced. This indicated that very short initiation times occurred in the CT specimen tests.

Compact tension specimens were often cooled to room temperature in solution before removal and fracturing open. Such specimens frequently had bright yellow, orange and brown corrosion products clinging loosely to the surface of the magnetite film in the crack reinitiation zone. These materials were analyzed by X-ray diffraction and the crystalline constituent was found identified as goethite, a hydrated form of $\alpha\text{-Fe}_2\text{O}_3$ or FeO(OH) (Table 9).

Compact tension specimens were fractured open and crack lengths were measured. Crack length was divided by time to failure to calculate average crack velocity over the period of the test and results are tabulated in Table 8. Average crack velocities decreased as yield strengths increased, and this confirmed the analogous trend of time to failure. The trend in average crack velocity plotted against upper yield point (or proportional limit) is shown in Figure 57 and is consistent with the trend in time to failure (Figure 44). Since crack propagation rate is one direct measure of susceptibility to cracking, this correlation indicated that susceptibility to caustic-nitrate waste solution cracking was inversely proportional to yield strength. Yield strength was the only mechanical property that correlated with crack velocity (Tables 5 and 9). Neither ductility parameters nor strain hardening parameters matched the trend of average crack velocity.

To help justify use of an average crack velocity that was measured

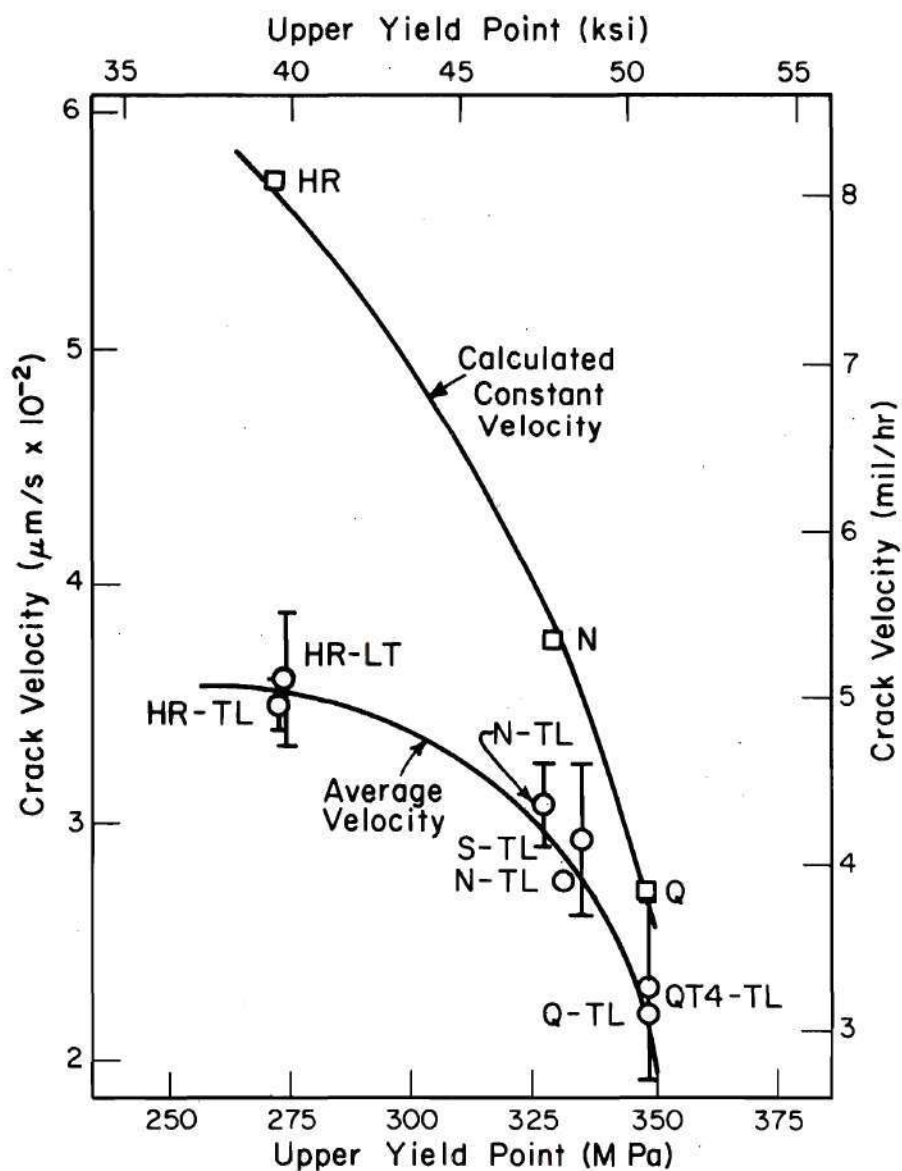


Figure 57. Crack Velocity of CT Specimens in H-Purex at 370°K, $K_I = 49.4 \text{ MPa(m)}^{1/2}$.

over a wide range of applied stress intensity (crack velocity is generally proportional to crack tip stress intensity in Stages I and III of SCC), approximate crack opening displacement-crack length calibrations were conducted in order to estimate instantaneous crack growth rates during SCC testing. The calibrations did not accurately account for the complicated effects of crack branching and plastic relaxation and were used only for reference purposes. HR and Q calibration specimens of three different fatigue crack lengths were loaded to the regular test load and crack opening displacements were measured. Additionally, crack opening displacement and crack length data from the start and end of CT specimen SCC tests were also utilized to calibrate CT specimens. An N microstructure calibration was also constructed on the basis of numerous SCC test data and the shapes of crack opening displacement-crack length calibration curves for the HR and Q microstructures. The displacement-crack length calibration data and constant load test displacement-time curves (Figure 43) were then used to construct approximate crack length-time plots for CT specimen SCC tests in H-Purex (Figure 58).

Calibrated crack growth rate increased rapidly with increasing crack length (stress intensity) near the start of constant load testing (Figure 58), however at longer crack lengths the crack growth rate became more constant. The relatively constant crack velocities measured in the "linear" regions of Figure 58 are listed in Table 8 as "Calculated Constant Velocity" and are also denoted by this title in Figure 57. Although the average velocity and constant calibrated velocity were different, they were of the same order of magnitude and showed the same relationship between yield strength and crack growth rate (Figure 57).

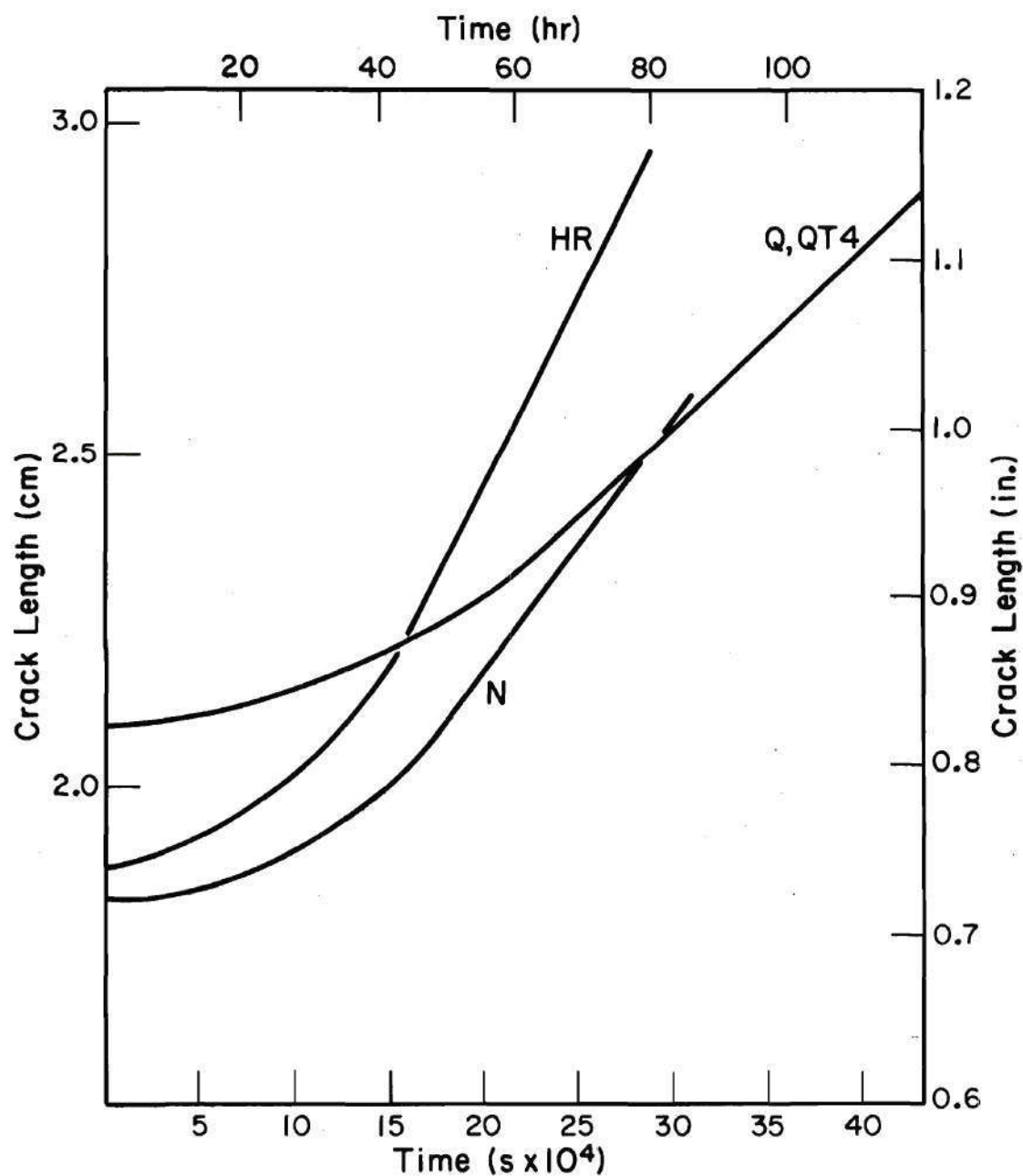


Figure 58. Calculated Crack Growth of CT Specimens in H-Purex at 370°K, $K_I = 49.4 \text{ MPa(m)}^{1/2}$.

The dependence of crack velocity upon yield strength could not be explained by purely mechanical, non-corrosion-related phenomena. The measured differences in crack velocities and times to failure were not simply due to high strength microstructures cracking farther and thus taking longer to reach ductile overload than low strength microstructures. Measured stress corrosion crack lengths in the high yield strength microstructures (Q, S) were not systematically larger than in the low yield strength structures (HR, N). Additionally, calculated instantaneous velocities were derived from actual specimen displacement-crack length data and would not be invalidated by differences in the crack length at ductile overload.

Constant Load Tests in 5M NaNO₃ Solution at pH 6.0

Compact tension specimens were also tested in 5M NaNO₃ at pH 6.0. The sodium nitrate solution was utilized in order to eliminate the many minor additives in H-Purex and to determine if the microstructural influence on cracking was the same in the presence of nitrate ion alone. Several microstructures were tested in addition to the structures which previously had been tested in H-Purex. Average displacement-time curves for duplicate TL oriented specimens of each microstructure are shown with the ranges in time to failure given by error bars (Figure 59). There was also an apparent correlation between yield strength and time to failure (Table 10 and Figure 60). This was compatible with the results in H-Purex solution (Figures 44 and 60).

A black, tenacious oxide film covered the entire surface of CT specimens exposed to the pH 6.0 solution of 5M NaNO₃. X-ray analysis showed that this film was magnetite. The same crack branching pattern

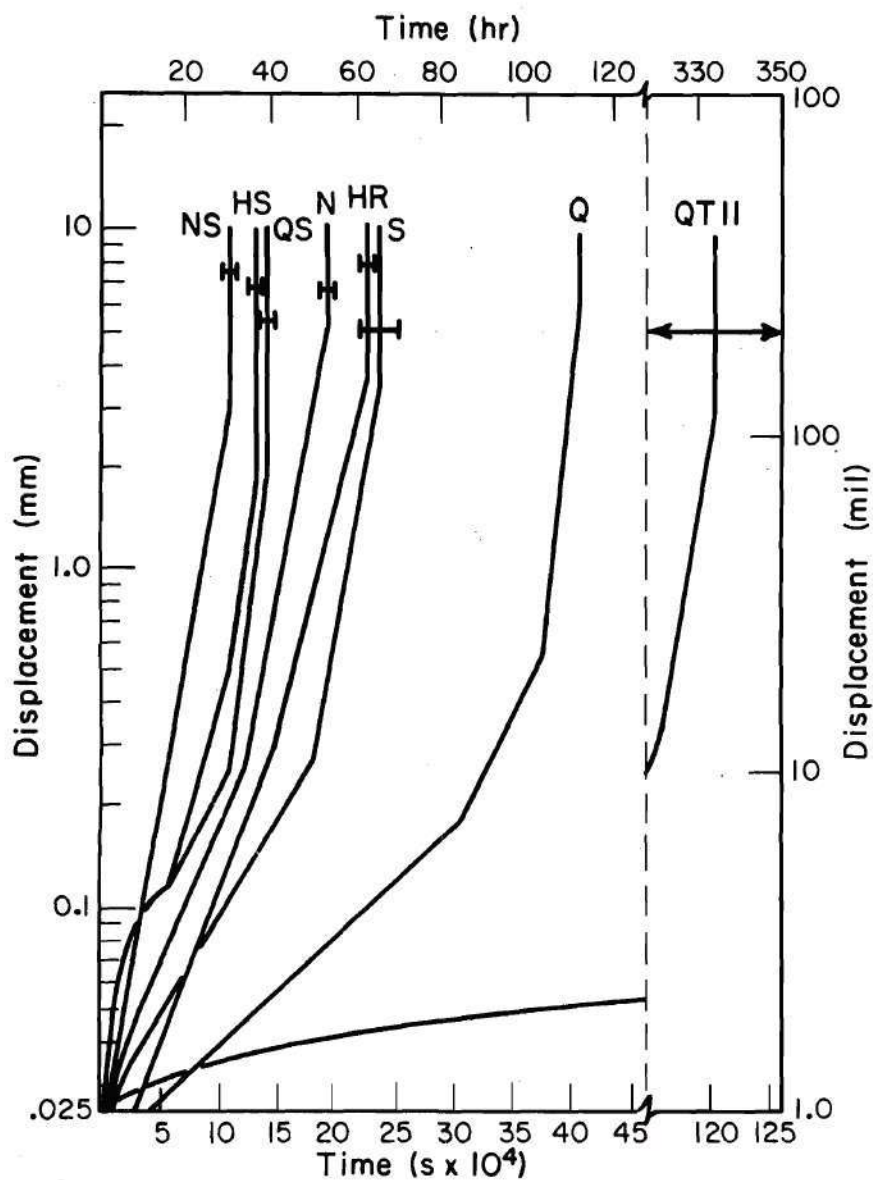


Figure 59. Crack Opening Displacement of CT Specimens in 5M NaNO_3 at pH 6.0, 370°K , $K_I = 49.4 \text{ MPa(m)}^{1/2}$.

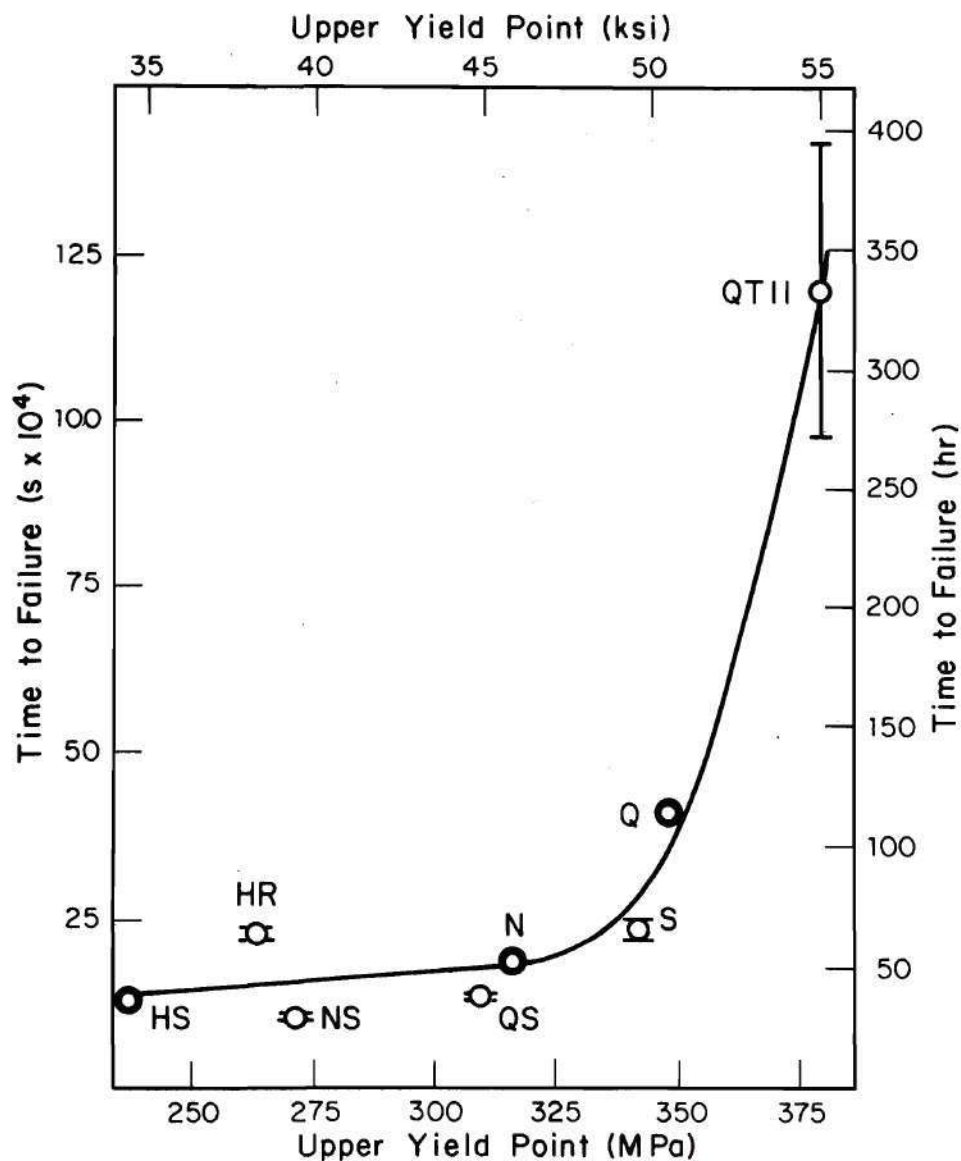


Figure 60. Time to Failure of CT Specimens in 5M NaNO_3 at pH 6.0, 370°K , $K_I = 49.4 \text{ MPa(m)}^{1/2}$.

as in H-Purex was found, however in the more aggressive 5M NaNO_3 solution there were numerous superficial cracks on the sides of the CT specimens which were confined to the plastically deforming zone around a crack tip.

The fracture surface was also covered with a black oxide film that seemed to be magnetite. Crack reinitiation also was seen, and a high magnification scanning electron micrograph of such a region with octahedral crystals (compatible with cubic magnetite) is shown in Figure 61.

Measurements of crack length and average crack velocity (Table 10) showed a correlation between average crack velocity and yield strength (Figure 62). The yield strength dependence of crack velocity was most pronounced at high yield strengths and diminished as the yield points decreased. The average crack velocities were 50-100% higher for each microstructure in the more aggressive 5M NaNO_3 solution than in H-Purex. Again, as in H-Purex solution, the average crack velocities did not correlate to any other mechanical property.

The temperature dependence of crack velocity was determined by testing a CT specimen at 357°K and at 345°K in addition to the duplicated test at 370°K. Crack velocities were measured both as average velocities (dividing crack lengths by the time to failure) and by as calculated instantaneous velocities (using approximate specimen calibrations). An Arrhenius plot of the logarithm of the crack velocity against reciprocal temperature at each of the three test temperatures gave an activation energy for average crack velocity of 69.5 ± 3.8 kJ/mole (16.6 ± 0.9 kcal/mole). The activation energy for a fairly constant calculated crack velocity at 2.5 cm (1 in.) crack length was somewhat lower: 61.9 ± 2.1 kJ/mole (14.8 ± 0.5 kcal/mole).

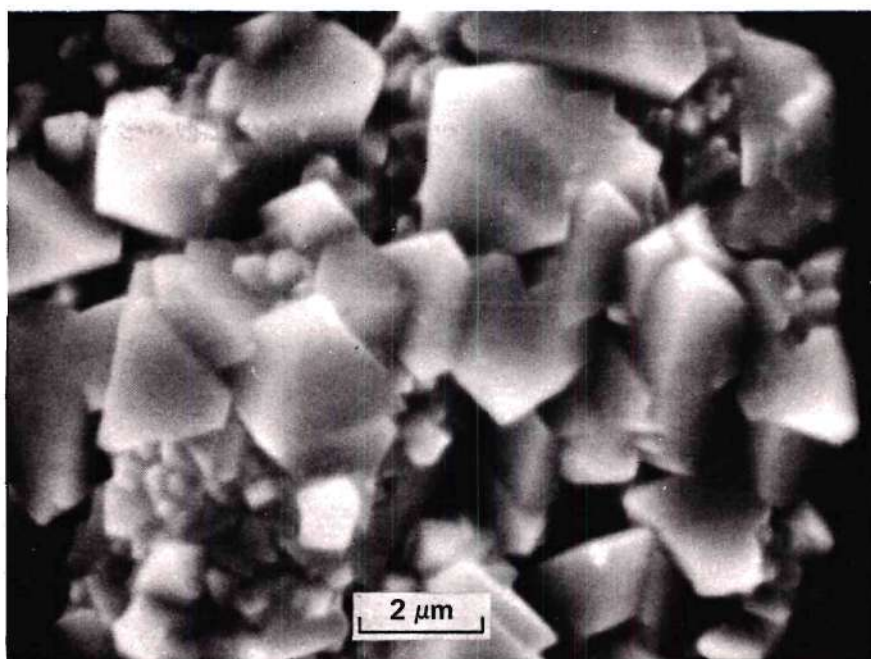


Figure 61. Crystalline Oxide on SCC Reinitiation Surface
in 5M NaNO_3 , pH 6.0.

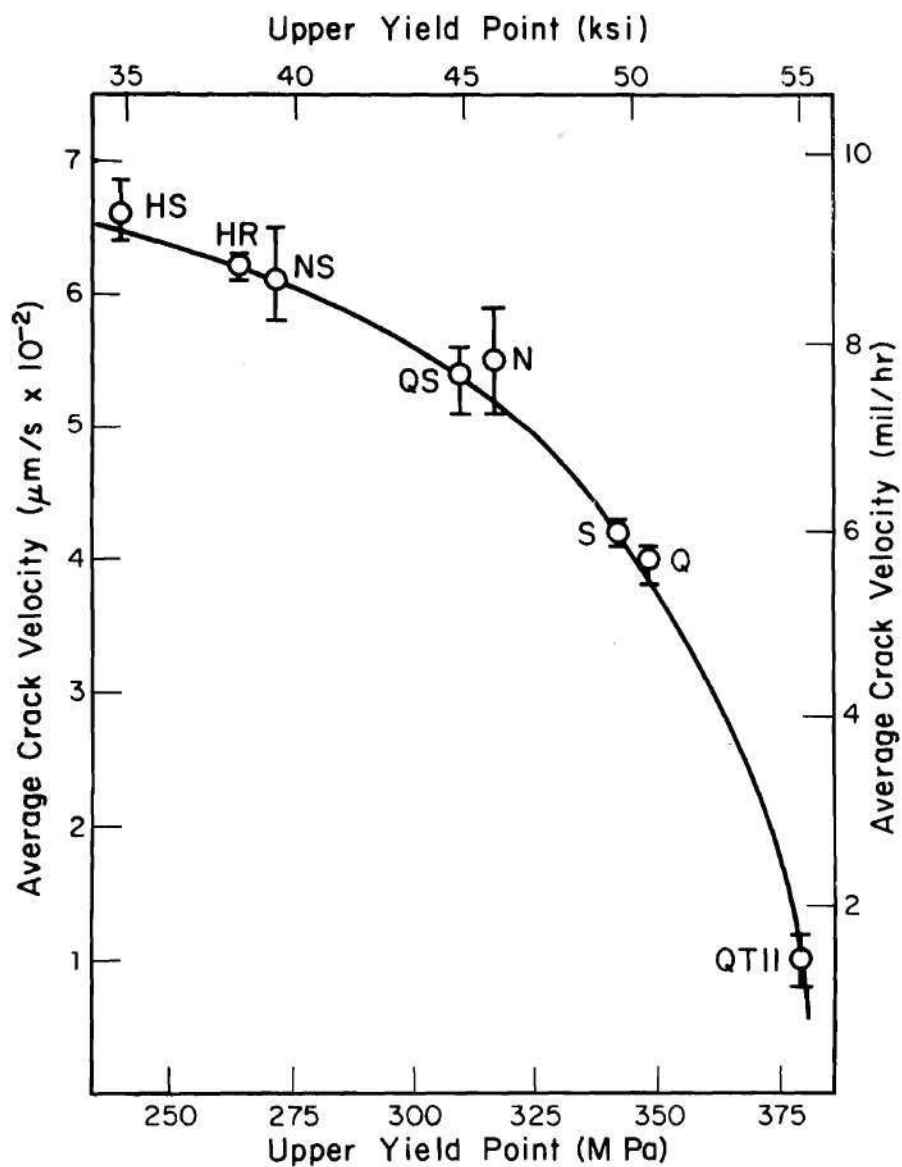


Figure 62. Average Crack Velocity of CT Specimens in 5M NaNO_3 at pH 6.0, 370°K , $K_I = 49.4 \text{ MPa(m)}^{1/2}$.

Constant Load Tests in 5M NaNO₃ Solution at pH 13.7

Compact tension specimens of the HR, N, S and Q microstructures were tested in 5M NaNO₃ solution at pH 13.7. This solution represented a composition similar to H-Purex but with a somewhat lower nitrate concentration (5M compared to 7.4M in H-Purex) and also a somewhat higher soluble hydroxide ion concentration (0.47M compared to 0.33M in H-Purex) due to the absence of hydroxide precipitation as found in H-Purex.

No microstructural dependence of time to failure or average crack velocity was seen in the pH 13.7 solution. Displacement-time curves for different microstructures overlapped extensively and did not indicate microstructural trends. Times to failure of individual specimens of a given microstructure varied by as much as 75%, and no significant trends could be detected beyond the data scatter. Crack velocities varied as much as 85% among specimens of a given microstructure and did not demonstrate a recognizable microstructural dependence. Average crack velocities were in the range $3.8\text{--}7.0 \times 10^{-2} \mu\text{m/s}$ (about the same as in pH 6 solution) for all microstructures. While a microstructural dependence of SCC susceptibility may have existed in the pH 13.7 solution, the data scatter prevented its measurement.

The external appearance of specimens exposed to the pH 13.7 solution was shiny and bright and showed that the caustic addition inhibited general corrosion. SCC fractures showed the same branching pattern as in other solutions, and the fracture surfaces likewise revealed a gray-black surface film that appeared to be magnetite.

Constant Displacement Tests in 5M NaNO₃ at pH 6.0 and pH 13.7

Wedge opening loaded specimens were tested in 5M NaNO₃ solution at

pH 6.0 and pH 13.7. WOL specimens of the HR, N, S and QT11 microstructures were tested with one specimen of each microstructure in pH 6.0 solution and another specimen in pH 13.7 solution. This was done to evaluate the effect of hydroxide ion and to determine the effect of microstructure on the crack arrest stress intensity, K_{scc} . Results are shown in Table 11 and Figure 63. There was a significant increase in K_{scc} of from 6% to 36% at the higher pH indicating an inhibitive effect of hydroxide. Additionally, the microstructural dependence of K_{scc} was the same in both solutions. This was compatible with earlier observations which indicated that SCC in waste solutions was due to the nitrate ion, and the hydroxide ion acted only as an inhibitor.⁹

The influence of hydroxide on K_{scc} did not indicate the reason for the large data scatter in CT specimen constant load tests in the pH 13.7 solution. The crack arrest stress intensities for specimens exposed in the caustic-nitrate solution, while somewhat higher than in pH 6.0 solution, were well below the initial stress intensity of CT tests for all but the QT11 microstructure. If K_{scc} and Stage I crack growth (Figure 2) had been elevated to near the initial stress intensity, then small variations in initial stress intensity (e.g., fatigue crack length) could have caused very large variations in initial crack growth rates and in measured average crack velocities. However, this did not appear to occur in the CT specimen tests.

The threshold stress intensities for cracking were generally proportional to yield strength (Figure 63). The trend in K_{scc} could not be correlated to any other mechanical property (Tables 5-6 and Figures 34-40). The relationship between K_{scc} and yield strength was

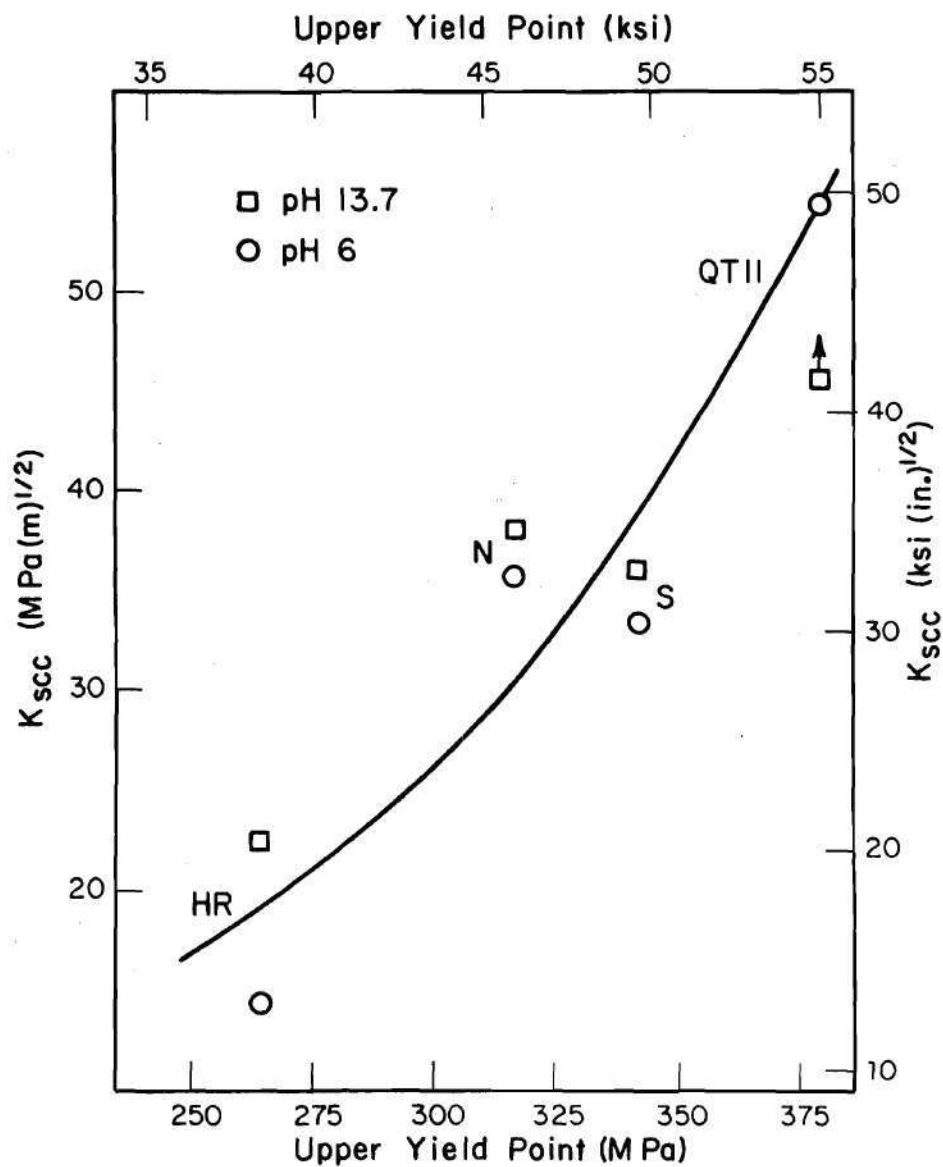


Figure 63. K_{SCC} of WOL Specimens in 5M $NaNO_3$ at pH 6.0 and pH 13.7, 368°K.

reproduced fairly consistently among the microstructures at both solution pH's. The QT11 specimens tested in pH 6.0 and pH 13.7 solutions showed no evidence of crack growth at an initial stress intensity of about $50 \text{ MPa(m)}^{1/2}$, but when the specimen in pH 6.0 solution was reloaded to a much higher initial loading it did produce cracking.

Yield strength was not the sole determining factor of K_{scc} in these tests. The N and S microstructures appeared reversed in order of yield strengths (Figure 63), indicating that other factors were involved. For this reason additional microstructures were tested in pH 6.0 solution and results are summarized in Figure 64 and Table 12. Results for the NS and QS microstructures were generally compatible with a yield point dependence of K_{scc} (Figure 64). The effect of long term spheroidization was to lower both yield strength and K_{scc} of the N and S microstructures. Although the yield points of the NS and QS microstructures were quite different, the K_{scc} values were virtually identical. This indicated an influence of microstructural properties in addition to yield point.

Tests conducted at the same initial stress intensity could be reproduced with high precision (NS specimens in Figure 64). However, an apparent K_{scc} dependence upon initial stress intensity was observed (Figure 64). Anomalously low K_{scc} values resulted from excessive initial loading that caused crack growth close to the back edge of the specimen (HR specimen loaded to $54 \text{ MPa(m)}^{1/2}$) or growth off at a steep angle from the specimen notch plane (QS specimen loaded to $50 \text{ MPa(m)}^{1/2}$). In such cases complicated geometry effects occurred which rendered the results inaccurate. These problems blocked attempts to measure K_{scc} in Q and SQ specimens and rendered the tests for these microstructures invalid.

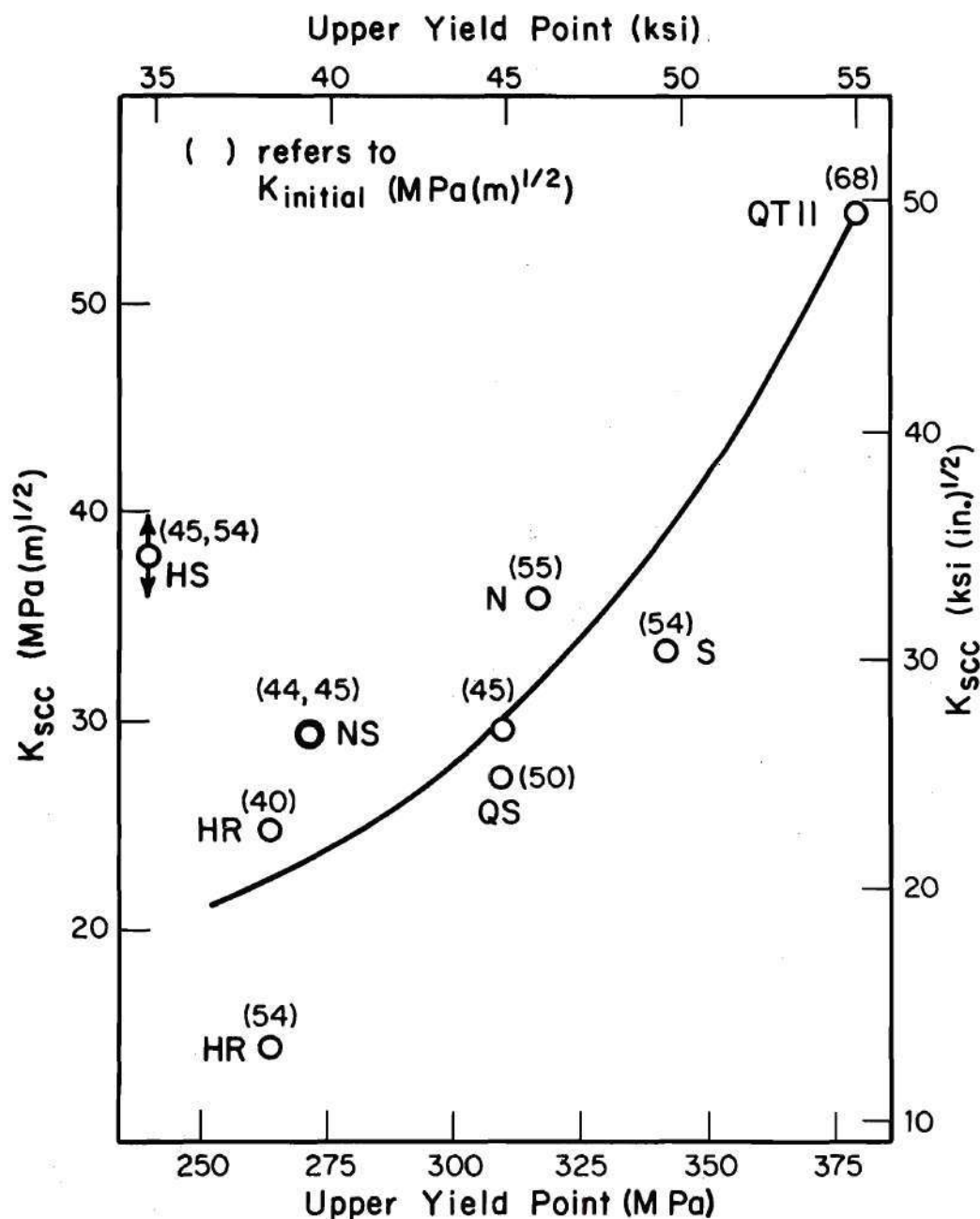


Figure 64. K_{scc} of WOL Specimens in 5M NaNO_3 at pH 6.0, 368°K.

HS specimen results were erratic. While in one HS specimen loaded to $45 \text{ MPa(m)}^{\frac{1}{2}}$ a very short crack formed with a K_{scc} of about $38 \text{ MPa(m)}^{\frac{1}{2}}$, another specimen loaded to about $54 \text{ MPa(m)}^{\frac{1}{2}}$ did not undergo significant crack growth. It is not known whether a reproducible K_{scc} for this microstructure would be greater or less than the calculated value for the short crack.

Crack growth rate measurements were conducted by monitoring crack length on the specimen sides at regular time intervals (usually every 100 hours). Crack growth rates decreased during the course of the experiments as crack length increased (stress intensity decreased). The crack length data usually indicated that 50 to 100 hours passed before measurable cracks could be detected on the specimen sides.

Specimens were fractured open at the completion of tests in order to measure final crack lengths, and it was observed that a magnetite film was present on SCC fracture surfaces (Figure 65). Although SCC surfaces were generally flat, delaminations perpendicular to the fracture surface (horizontal lines in Figures 65-66) could be seen, presumably at bands of sulfide stringers. Between the delaminations some surfaces had features that appeared similar to the chevron-like markings characteristic of brittle fracture in steel (Figure 66). These chevron-like markings are not generally known to occur in IG SCC. The appearance of the crack tip at crack arrest is shown in Figure 65. The crack front profile is much flatter and not as parabolic as the profile in CT specimens (Figure 46). The profile of the stress corrosion crack tip may be due to dynamic effects involving pH depletion and maintenance of occluded corrosion cell¹²⁵ crack tip chemistry. However, it is interesting to note that the crack tip

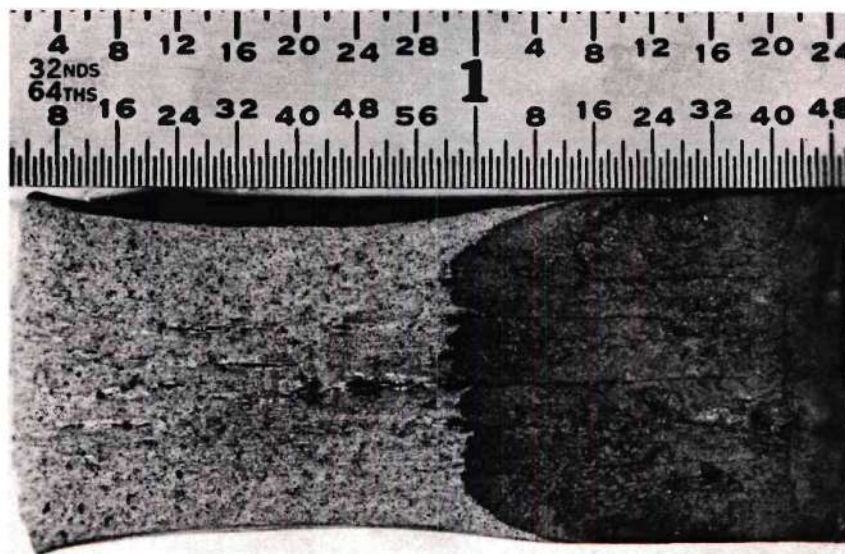


Figure 65. Fracture Surface of WOL Specimen.

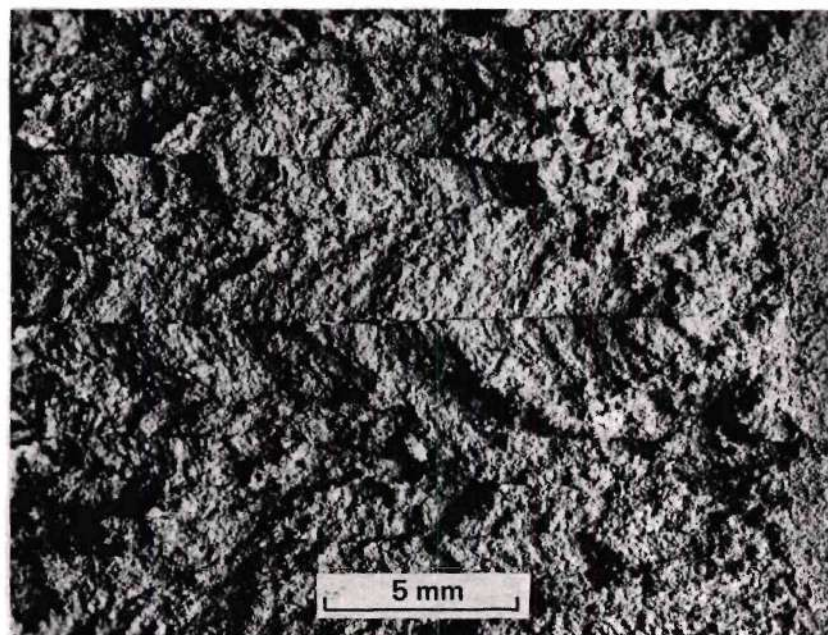


Figure 66. Closeup of Chevron-like Markings on SCC Fracture Surface.

profiles in CT and WOL specimens resemble the expected shapes of the plastic zone at a crack tip at high and low stress intensities respectively.¹⁴³

The relationship between crack velocity and stress intensity for various microstructures in 5M NaNO₃ at pH 6 is shown in Figure 68. For reference, calculated crack velocities from CT specimen tests for the HR microstructure are also plotted. These measurements indicated that stress independent crack growth, Stage II SCC,⁵¹ occurred for HR material in the vicinity of 30-46 MPa(m)^{1/2} (27-42 ksi(in)^{1/2}). They also indicated that the rise in crack velocity with stress intensity above this range, so-called Stage III cracking,⁵¹ was not as steep as in Stage I, the region near K_{scc}. Other microstructures had higher K_{scc} values than the HR material, and their Stage II cracking regions, if present, were at higher stress intensities (Figure 68).

Crack length measurements were used to determine the relationship between crack velocity and stress intensity in WOL specimen tests. WOL specimens tested in 5M NaNO₃ at pH 6.0 and pH 13.7 demonstrated that State II crack velocities in the two solutions were similar (Figure 67). Although the addition of 0.47M hydroxide ion to 5M NaNO₃ increased K_{scc} (Figures 63 and 67), there was not a substantial reduction in crack velocity at higher stress intensities near the Stage II cracking region. These measurements of similar Stage II crack velocities in the two solutions are compatible with the measurements of similar average crack velocities in CT specimen tests at pH 6.0 and pH 13.7.

Wedge opening loaded specimen tests of HR material were conducted at four different temperatures: 370°K, 357°K, 345°K and 333°K (97°, 84°, 84°, 84°).

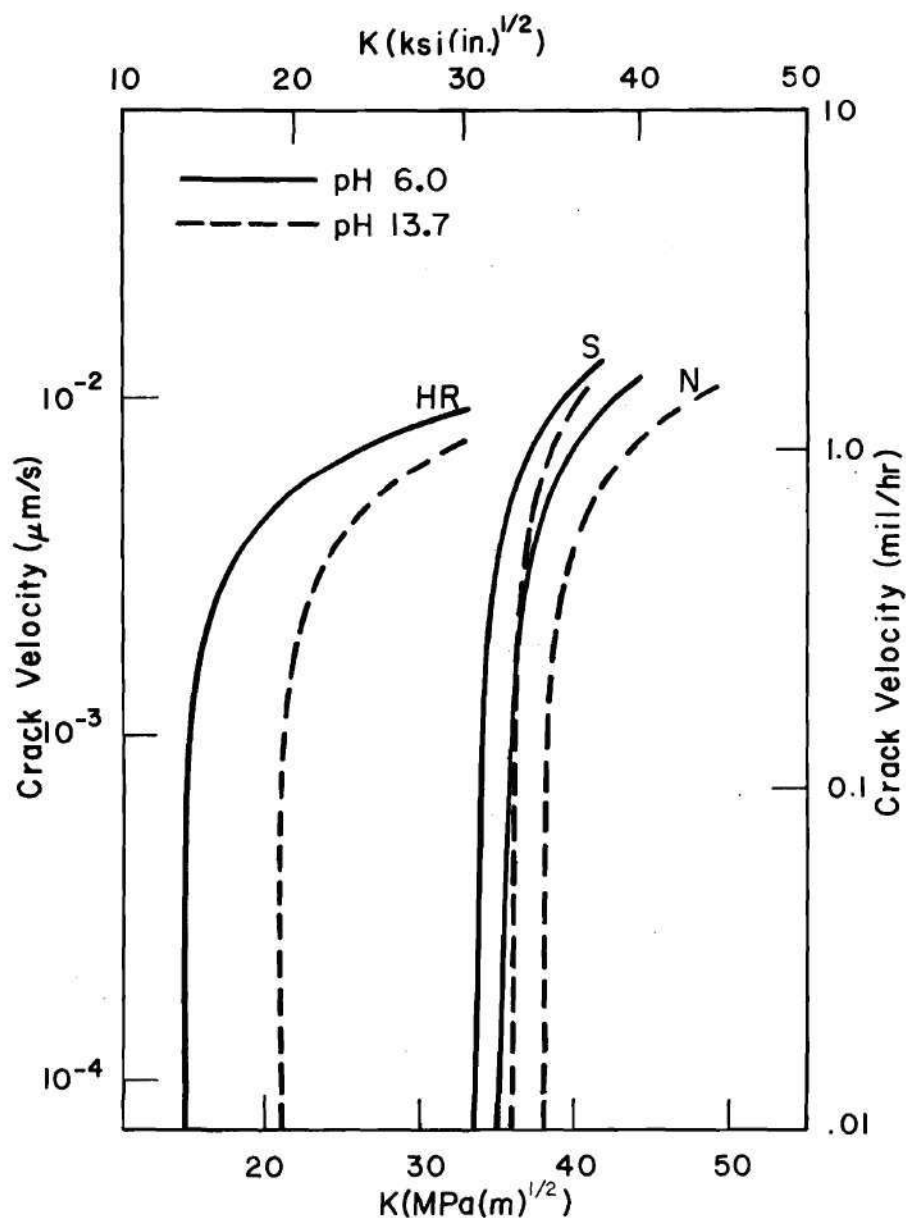


Figure 67. Crack Velocities of WOL Specimens in 5M NaNO_3 at pH 6.0 and pH 13.7, 368°K.

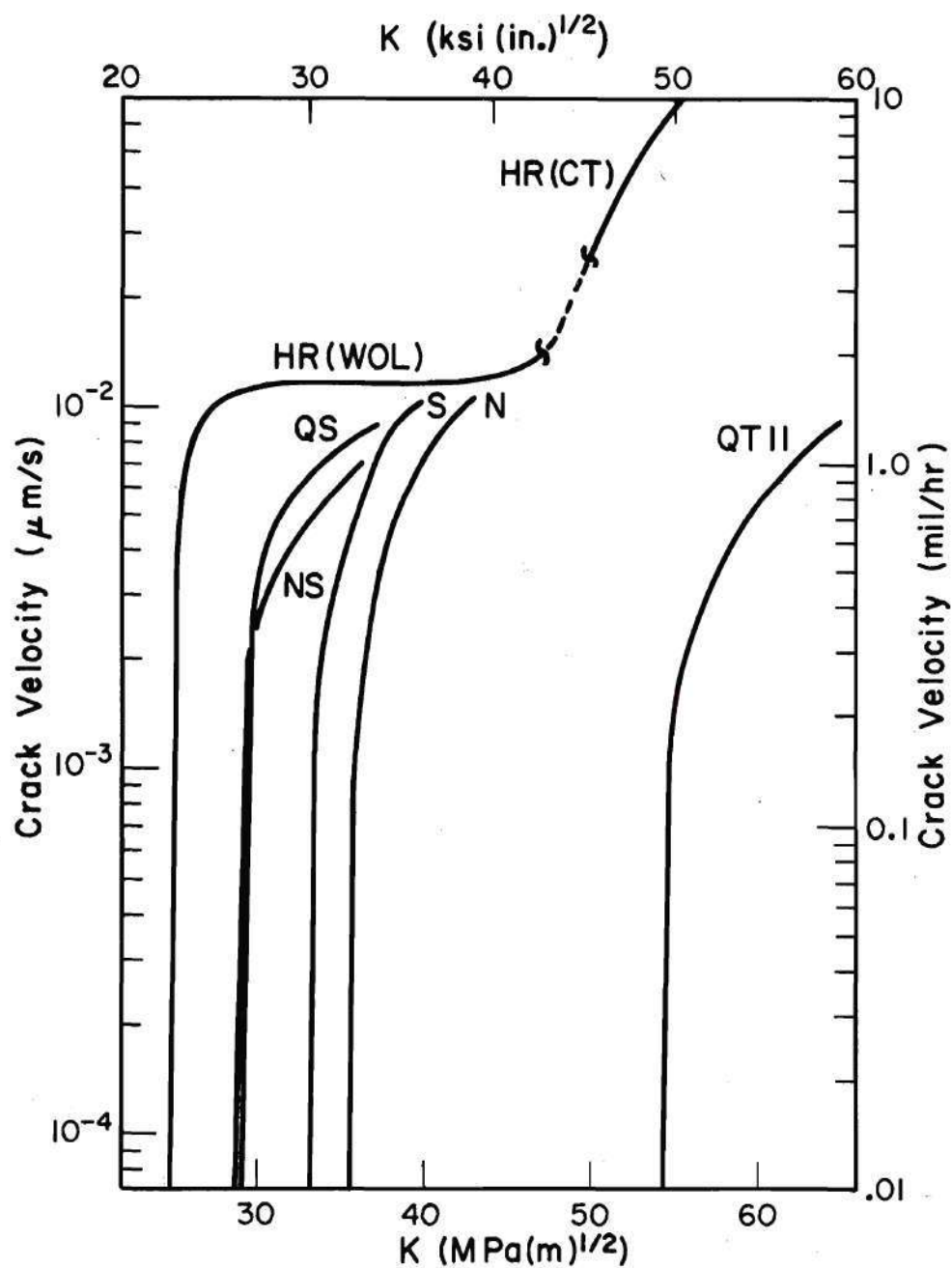


Figure 68. Crack Velocities of SCC Specimens in 5M NaNO₃ at pH 6.0, 368°-370°K.

72° and 60°C). Results are summarized in Figure 69. Instantaneous crack velocities were calculated from HR specimen calibrations, and displacement-time curves for CT specimens tested at 370°, 357° and 345°K (97°, 84° and 72°C) are also plotted for comparison. The data showed there was little effect of temperature on K_{scc} in the temperature range studied. However, there was a pronounced effect of temperature on crack velocity. The activation energy for crack growth at given stress intensity near K_{scc} was quite large. However, because of the rapid change in crack velocity with stress intensity, the activation energy could not be determined accurately. A large activation energy could account for apparent independence of K_{scc} upon temperature in Figure 69. The activation energy for crack growth decreased rapidly with increasing stress intensity from about 71 kJ/mole (17 kcal/mole) at a stress intensity slightly above K_{scc} to about 36 kJ/mole (8.7 kcal/mole) midway through the Stage I-Stage II transition region (the various stages of cracking are denoted on Figure 69). Extrapolated data between hot-rolled WOL specimen results and hot-rolled CT specimen results in the Stage II region of cracking gave an estimated activation energy for crack growth of about 15 kJ/mole (4 kcal/mole). While some of the calculated activation energies were only estimates based upon extrapolated data, they demonstrated significant variations in kinetic behavior across a wide range of stress intensities in nitrate SCC.

Corrosion Experiments

Corrosion Coupon Tests

Corrosion coupons of the HR, N, S and Q microstructures were exposed to 5M NaNO_3 at pH 6.0 for 500 hours at 368°K and showed no

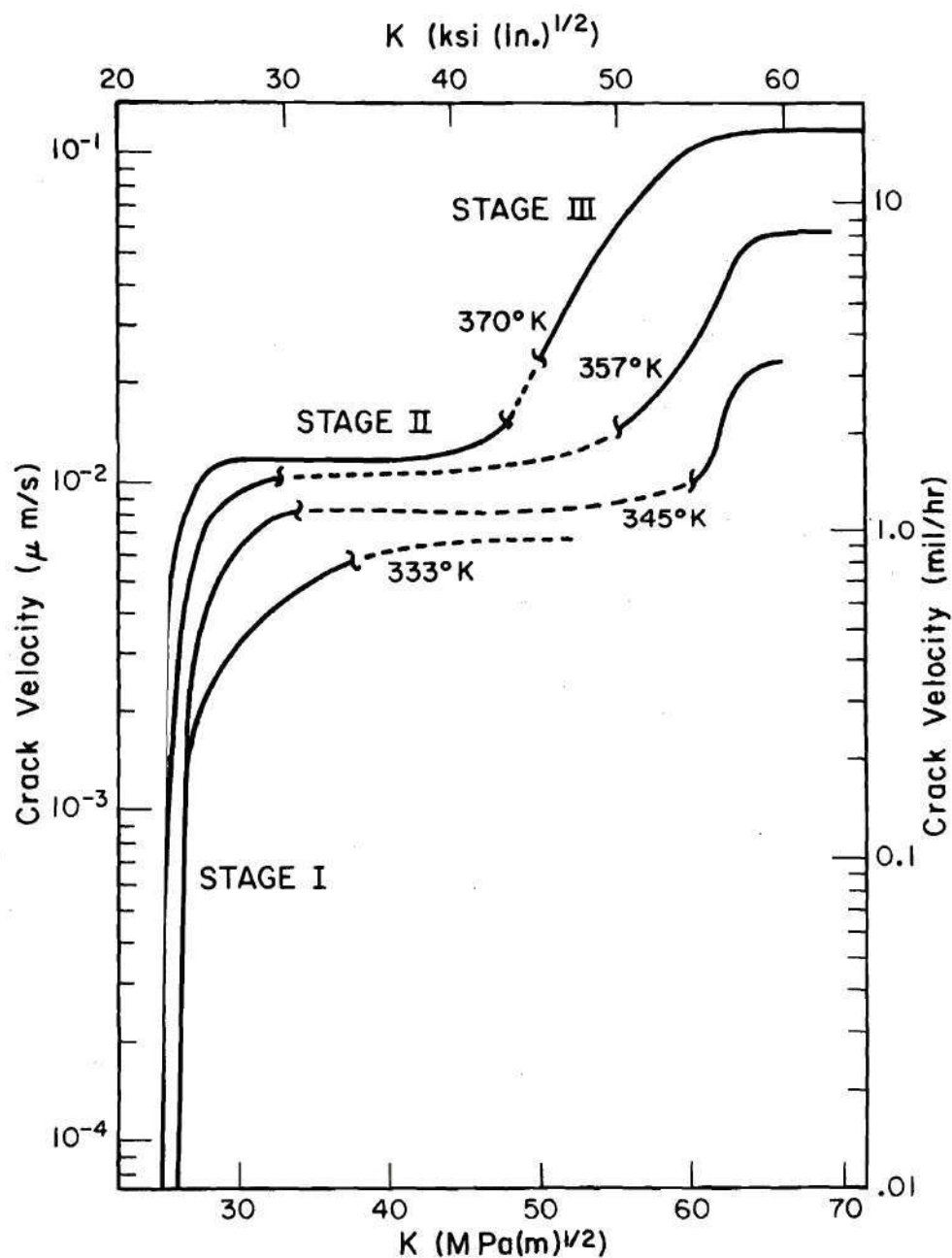


Figure 69. Crack Velocities of Hot-Rolled Steel in 5M NaNO₃ at pH 6.0, Various Temperatures.

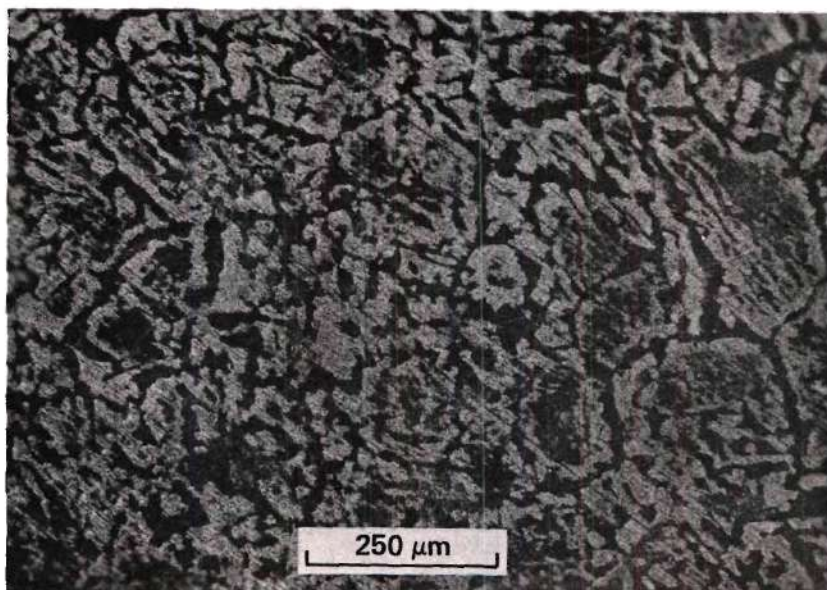


Figure 70. Oxide Pattern on HR Corrosion Coupon.

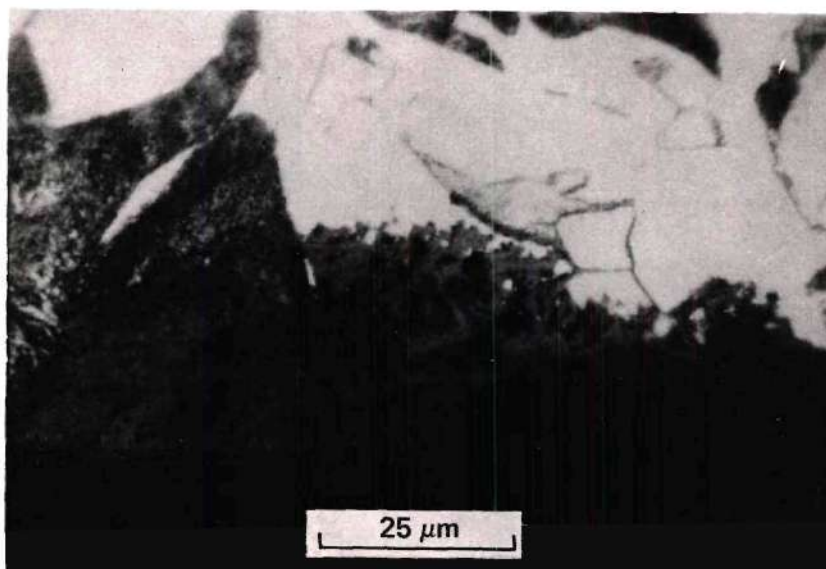


Figure 71. Pitting and IG Attack on HR Corrosion Coupon.

open circuit potentials more negative than -500 mV SCE when measured within the first minute of immersion. The open circuit potentials of the specimens rose rapidly with time initially but slowed and stabilized at equilibrium open circuit corrosion potentials in about one hour. Stabilized corrosion potentials were on the order of -350 mV SCE. Specimens generally remained tarnish-free during the one hour stabilization period.

Current density measurements for both anodic and cathodic polarization experiments are shown in Figure 72. A current-limited (constant current density) region was found during cathodic polarization (Figure 72), beyond which significant hydrogen gas evolution was noted on the specimens. Anodic polarization was characterized by rapidly rising current density and no evidence of passivity up to about 50 mA/cm^2 (Figure 72). During anodic polarization experiments the nitrate solution rapidly turned orange, then yellow-brown, then muddy brown and opaque and finally black. Vigorous gas evolution was also noted on the specimen surface. The gas was some species other than oxygen (which could only be generated at a much more positive potential¹²⁴ than the range of the tests). By the end of each anodic polarization experiment, the test cell was obviously full of insoluble corrosion products which made the solution quite opaque. The black color at the end of the experiments was due to magnetite or manganese corrosion products; considerable corrosion had occurred and pH had increased to the caustic range, about pH 9, by the end of the experiment. This would favor precipitation of both magnetite as well as manganese oxides and hydroxides.

The differences between the polarization characteristics of the

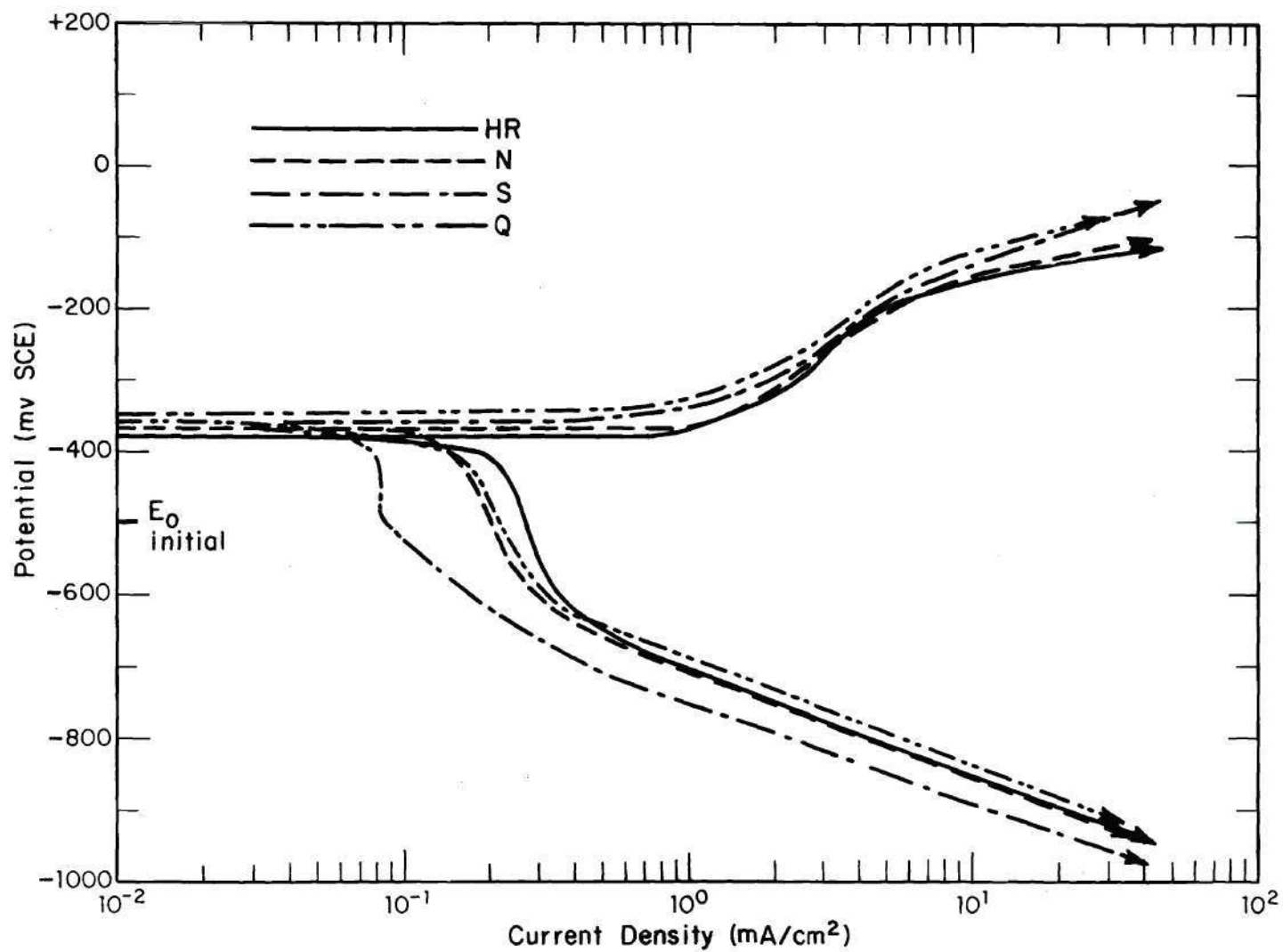


Figure 72. Polarization Curves in 5M NaNO₃ at pH 3.5, 370°K.

different microstructures were generally quite small. Hot rolled material had the most active corrosion potential and the highest anodic current density at a given potential of any of the microstructures tested (Figure 72). The Q material, conversely, had the lowest anodic current density.

Polarization specimens were deeply pitted after anodic polarization experiments, and pitting rendered the polarization data very irreproducible. The apparent relationship between microstructure and polarization behavior is thus subject to data scatter on the same order of magnitude as the relative current densities measured for the various microstructures. However, the data indicate that the microstructural dependence of crack velocity and the microstructural dependence of corrosion rate (in acidic nitrate) are similar.

Polarization Experiments at pH 6.0. In pH 6.0 solutions of 5M NaNO_3 the polarization specimens exhibited open circuit potentials of about -450 mV SCE when measured within one minute of immersion. Stabilized corrosion potentials after one hour of immersion were about -400 mV SCE. In pH 6.0 solution the specimens had a thin, dull film at the end of the stabilization period. Cathodic polarization experiments displayed less evidence of current limitation than in pH 3.5 solution and cathodic currents were generally somewhat lower (Figure 73). No correlation was seen between the microstructural dependence of cathodic current density and the microstructural dependence of crack velocity. Anodic polarization in pH 6.0 solution was characterized by the presence of passivation peaks at large densities of about 100 mA/cm^2 . The passivating potential and the critical current density at this peak do not seem to correlate to the microstructural dependence of crack velocity either.

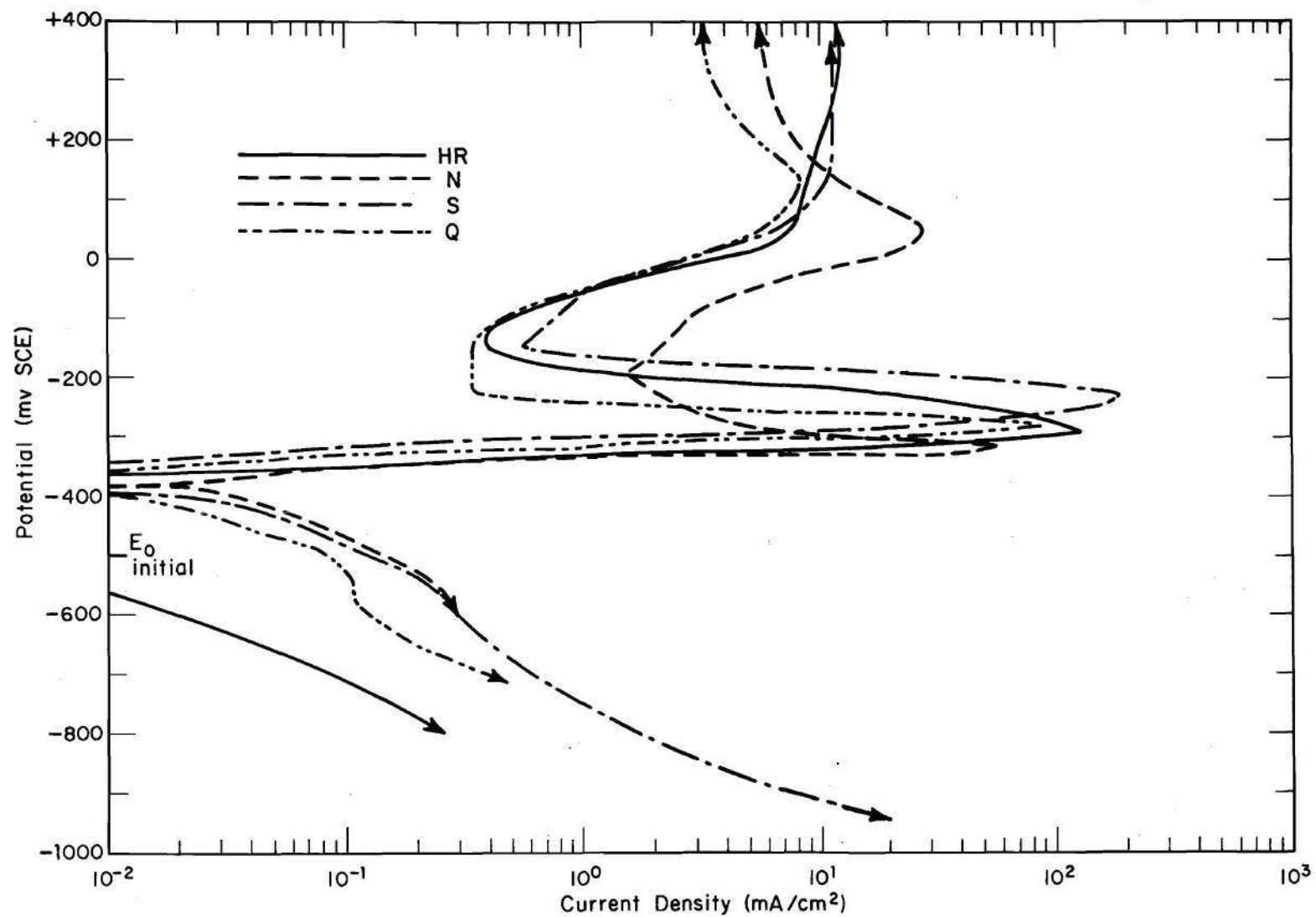


Figure 73. Polarization Curves in 5M NaNO₃ at pH 6.0, 370°K.

Anodic polarization experiment solutions initially at pH 6.0 turned a light blue-green color that indicated the presence of ferrous ions. As the potential and current were raised, increased gas evolution was noted, and the solution color darkened and became brownish green and indicated the presence of ferric ions. At potentials above the passivation peak the color became black and indicated the presence of the same suspended corrosion products as the tests in pH 3.5 solution. The final pH in these tests was also in the basic range and was slightly higher than for the pH 3.5 solution.

Polarization Experiments at pH 13.7. Polarization behavior of steel electrodes was also examined in pH 13.7 solution in order to demonstrate the effect of hydroxide ion. Polarization curves for the HR and Q microstructures demonstrated the inhibiting effect of hydroxide ion (Figure 74). Current densities ranged several orders of magnitude lower than in the other test solutions. Open circuit potentials as low as -700 mV SCE were measured within the first minute of immersion. After an hour of immersion the corrosion potential had stabilized at -300 to -400 mV SCE. The wide variation in corrosion potential from one experiment to the next seemed to indicate metastable passivation conditions.⁷⁶ After the potential stabilized the specimens were still bright and shiny as expected from CT specimen and WOL specimen tests.

Cathodic polarization curves did not demonstrate a pronounced current limited region in pH 13.7 solution (Figure 74). Anodic polarization curves showed a small increase in anodic current density for a few hundred millivolts. However in the vicinity of 0 mV SCE there were sudden jumps in anodic current density associated with pit formation.

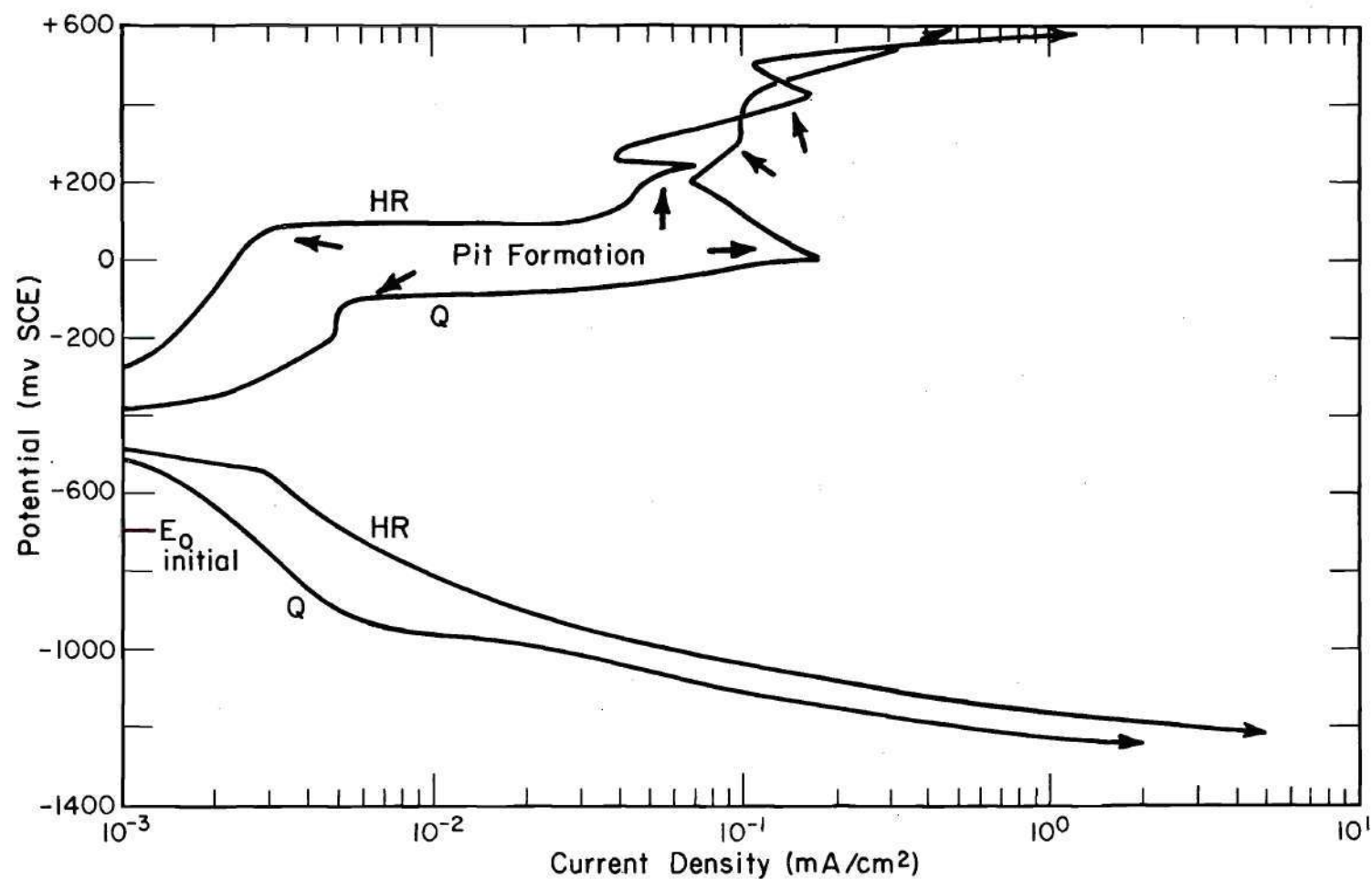


Figure 74. Polarization Curves in 5M NaNO₃ at pH 13.7, 370°K.

For each current density jump a new pit was detected on the surface of test specimens. As the pits grew it was observed that their surfaces were covered with a brown oxide. Additionally, copious quantities of gas bubbles were seen issuing from the pits, usually at the outer periphery of the growing oxide film on the pit. Specimen surfaces were otherwise shiny and uncorroded; this also seemed to indicate a condition of metastable passivation in pH 13.7 solution.

Essentially all of the anodic current that was passed through a specimen in pH 13.7 solution was associated with anodic processes within the pits. Since most of the specimen surface area remained bright and uncorroded, these areas did not contribute substantially to the anodic current flow. The large quantities of gas which issued from pits, however, indicated that significant current flow and reaction rates occurred inside the pits. Upon completion of the test and removal of the applied potential, pits were observed to continue issuing gas bubbles for some three or more minutes. It seemed that either immense gas pressures had been accumulated under the oxide or that electrochemical reactions within the pits continued to occur for some time, independent of the externally applied potential.

Summary of Results

Effect of Microstructure on Cracking in Nitrate Solutions

Yield strength influenced the cracking susceptibility of A 516 Grade 70 steel at both high and low stress intensities in nitrate and caustic-nitrate solutions (Figures 57 and 62-64). The influence of yield strength overrode other microstructural considerations at high stress intensities. At low stress intensities other microstructural effects

(e.g., grain boundary corrosion susceptibility) also appeared to be important; while there was a general correlation between yield strength and K_{sc} , specific microstructures deviated from a strict yield point dependence (Figures 63 and 64).

The carbide morphology of A 516 Grade 70 steel was not of primary importance in determining susceptibility to cracking in nitrate and caustic-nitrate solutions. Pearlitic microstructures HR and N had different susceptibilities to cracking (Figures 57 and 62-64); coarsely spheroidized microstructures HS, NS and QS likewise had different susceptibilities to cracking (Figures 62 and 64).

Effect of Microstructure on Corrosion in Nitrate Solutions

Corrosion rates in nitrate and caustic-nitrate solutions were not related to microstructure in a manner that would readily explain the results of the cracking experiments (Figures 72-74). The relative anodic current densities of various microstructures in acidic (pH 3.5) nitrate solution were similar to the relative susceptibilities of the microstructures to nitrate cracking, however the differences in open circuit potential and anodic current density were quite small and not highly reproducible (Figure 72). The relative corrosion rates in pH 6.0 and pH 13.7 solutions were not similar to the relative cracking susceptibilities of various microstructures (Figures 73 and 74).

Effect of Hydroxide Ion on Corrosion and Cracking in Nitrate Solutions

Addition of 0.47M hydroxide ion to 5M NaNO_3 inhibited cracking at low stress intensities by raising K_{sc} (Figure 63). However the addition of hydroxide ion did not significantly change Stage II crack velocities (Figure 67) nor did the addition of hydroxide significantly change average

crack velocities in constant load CT specimen tests. The addition of 0.47M hydroxide ion did not change the microstructural trend of cracking susceptibilities in nitrate solution at low stress intensities (Figure 63), but at high stress intensities the microstructural trend in nitrate solution was obscured by data scatter. Thus hydroxide ion seemed to act only as an inhibitor of nitrate cracking in the nitrate solution studied. Addition of 0.47M hydroxide ion to 5M NaNO_3 inhibited general corrosion of the outer surfaces of SCC specimens and polarization electordes, but the inhibition was not stable. Pitting and high anodic currents at pits were found on polarization electrodes.

Effect of Temperature on Cracking in Nitrate Solutions

Increasing temperature increased crack growth rate in nitrate solution but did not significantly change K_{scc} (Figure 69). The measured activation energy for crack growth in Stage I cracking decreased with increasing stress intensity from at least 71 kJ/mole (17 kcal/mole) near K_{scc} to 36 kJ/mole (8.7 kcal/mole) at a stress intensity midway through the Stage I-Stage II transition region. Based on extrapolated data between WOL specimen tests and CT specimen tests (Figure 69), the apparent activation energy for Stage II crack growth was about 15 kJ/mole (4 kcal/mole). The measured activation energy for Stage III crack growth was much larger than in Stage II and was 62-70 kJ/mole (15-17 kcal/mole).

Fractographic Characteristics of Cracking in Nitrate Solutions

Fractographic analysis indicated that cracking in caustic-nitrate solutions was accompanied by a localized change in solution chemistry in cracks. SCC fracture surfaces always demonstrated magnetite formation, even in solutions that passivated specimen outer surfaces (Figures 46 and 65).

Nitrate solutions of acidic or near-neutral pH caused increased corrosion and magnetite formation on all specimen surfaces. Crack initiation after ductile overload of SCC specimens in caustic-nitrate solutions was accompanied by gradual change in localized solution conditions (Figure 46). This appeared as a gradual buildup of a bulk magnetite film with various interference colors at the tip of the ductile overload fracture. Corrosion coupons of unstressed steel in nitrate solution revealed grain boundary trenches, cubic etch pits and thus localized acidification at the bases of magnetite-filled pits at surfaces (Figure 71). The etch pits appeared similar to fractographic features on SCC surfaces (Figures 54-56). Corrosion of polarization electrodes in caustic-nitrate solution was accompanied by localized breakdown of passivity (Figure 74). Pitting, localized oxide features and vigorous gas evolution from pits indicated anodic and cathodic processes concentrated at pits accompanied by localized changes in solution chemistry.

CHAPTER IV

DISCUSSION OF RESULTS

Cracking in Nitrate and Caustic-Nitrate SolutionsNitrate Cracking in Synthetic Nuclear Waste Solution

The stress corrosion cracking of mild steel in synthetic H-Purex nuclear waste and similar solutions appeared to be due to the nitrate ion alone. The microstructural trend of cracking susceptibilities was the same in H-Purex and pure sodium nitrate solutions (Figures 57 and 62). The microstructural trend of cracking susceptibilities was also the same in 5M NaNO_3 at pH 6.0 and at pH 13.7 (Figure 63). Furthermore, average crack velocities were higher in 5M NaNO_3 at pH 6.0 than in synthetic H-Purex (Figures 57 and 62), but the sodium nitrate solution had lower nitrate ion concentration (5M compared to 7.4M in H-Purex) and lower hydroxide ion concentration (10^{-8}M compared to 0.33M in H-Purex). If hydroxide ion were a significant cracking agent in synthetic H-Purex, then lower crack velocities should have been observed in the sodium nitrate solution than in synthetic H-Purex. In addition, earlier studies showed that open circuit steel electrode potentials in waste solutions were in the expected range for nitrate cracking.⁹ Open circuit electrode potentials measured in this study were relatively unchanged when 0.47M hydroxide ion was added to a 5M NaNO_3 solution at pH 6.0.

Fractographic evidence suggested that synthetic nuclear waste, caustic-nitrate and nitrate solution cracking occurred under acidic and nearly neutral pH solution chemistry conditions within the crack. This

also indicated that cracks grew in environments that were predominantly nitrate ion (rather than hydroxide ion). Shiny specimens that had been exposed to caustic-nitrate solutions (Figure 45) had magnetite-covered SCC fracture surfaces (Figure 46-47). Magnetite is stable in a narrow potential range at testing temperatures between pH 6 and 15 (measured at room temperature).¹²⁴ However, for a thick magnetite film to form there must be a high corrosion rate. Thus one would expect the solution adjacent to the growing magnetite in the crack to be at the lower end of the pH range for magnetite stability. Specimens exposed to sodium nitrate at pH 6.0 did have a thick magnetite film over all surfaces.

The solution pH not far from the tip of growing cracks appeared to be less than pH 9, the highest pH at which ferrous ion can be stable.¹²⁴ Fracture specimens that were cooled to room temperature before removal from solution had loosely adherent goethite ($\text{FeO}(\text{OH})$), especially in the crack reinitiation zone. The goethite appeared to have precipitated from solution upon the adherent magnetite film; because of the goethite's powdery nature, it did not appear to have epitaxially grown upon the steel substrate as did the magnetite. The deposition of goethite from solution indicated that ferrous ions had been present which had precipitated onto the magnetite as an insoluble hydroxide and then reacted with additional hydroxide ion to form goethite.¹⁰⁹

The solution chemistry at the very tip of growing nitrate cracks appeared to be acidic. A narrow region at the tip of growing cracks was film-free, and apparently the grain boundaries were subjected to free dissolution conditions (Figure 49). Cubic etch pits on SCC fracture surfaces (Figure 54) and adjacent to narrow grain boundary cracks

(Figures 55-56) also suggested acidic conditions. Similarly, etch pitting at the base of large nitrate solution pits suggested localized acidification; pitting in aqueous solutions is commonly associated with localized acidification and occluded corrosion cell formation.¹²⁵ Free dissolution would be expected at typical nitrate cracking potentials^{24,26,34} in acidic solutions.¹²⁴

Stage I Cracking

Crack Initiation. For a nitrate crack to measurably grow in steel there seemed to be a critical combination of solution chemistry, temperature and stress intensity needed at the tip of a surface flaw (Figures 2 and 69). Removal of any single factor (reduction of stress intensity during WOL specimen tests) caused a crack to arrest. Conversely, introduction of a final, missing factor (crack tip chemistry during CT specimen crack reinitiation) initiated cracking.

The reinitiation of cracks in CT specimens that were exposed to caustic-nitrate solutions was preceeded by a gradual change in crack tip solution chemistry from high pH, passive conditions to low pH, bulk magnetite formation (Figure 46). The spectrum of interference colors that remained after cracks had reinitiated showed that chemical changes preceeding reinitiation took place near the tip of ductile overload fractures, some distance before the actual onset of IG SCC and formation of bulk magnetite. This indicated that a substantial reduction in pH occurred over a measurable distance. It is reasonable to assume that the proper crack tip chemistry conditions were a requirement for IG SCC initiation.

The elevation of K_{scc} by addition of 0.47M hydroxide ion to 5M NaNO_3 showed that hydroxide promoted crack arrest (and presumably inhibited

crack initiation) at low stress intensities (Figure 63). Apparently, the necessary crack tip solution chemistry conditions for cracking were more difficult to maintain in the higher pH solution. This is not surprising, since fractographic evidence suggested that a growing crack tip was acidic, and the pH gradient from the bulk solution to the crack tip would be larger in the more caustic solution.

The effect of temperature on crack initiation and growth in Stage I nitrate cracking was quite different than the effect of hydroxide ion. Temperature changes from 370°-333°K had no appreciable effect on K_{scc} (Figure 69). Measured activation energies for Stage I crack growth decreased with increasing stress intensity. An activation energy could not be measured at K_{scc} accurately; the increase in crack velocity with increasing stress intensity was too rapid. However, at a stress intensity just above K_{scc} the measured activation energy was about 71 kJ/mole (17 kcal/mole). Thus the activation energy for crack growth must be at least as large at K_{scc} .

The apparent activation energy for crack growth at K_{scc} indicated that oxide rupture or some other plastic deformation-related event¹⁴⁴ controlled crack initiation. The activation energies for carbon and nitrogen diffusion in ferrite are 75-90 kJ/mole (18-22 kcal/mole), in fair agreement with the measured value. The importance of interstitial atom diffusion in deformation processes in steels is emphasized by the involvement of dislocation-interstitial interactions in Portevin-le Chatelier effect (discontinuous yielding), temper embrittlement, aging and microcreep effects.¹³⁷ On the other hand, Stage I crack velocities might be controlled by refilming rates after oxide rupture. The activation energy for magnetite

growth has been reported as 63-88 kJ/mole (15-21 kcal/mole) in aqueous media,^{145,146} also in fair agreement with the measured activation energy.

Crack velocities increased with increasing temperature in Stage I cracking (Figure 69). Thus refilming of the crack tip itself could not be rate controlling. Such a process would be faster at higher temperature, and this would decrease crack propagation rate at higher temperatures. An alternative explanation is that refilming of crack walls behind the crack tip would restrict dissolution to the extreme tip of the growing crack so that cracking rather than wide spread dissolution and crack blunting would occur. It is well known that restriction of dissolution to small anodic areas by insufficient addition of corrosion inhibitors can intensify pitting and intergranular trenching.¹⁴⁷

Effect of Microstructure. Wedge opening loaded specimen stress corrosion tests indicated that K_{scc} was generally proportional to yield strength (Figures 63-64). This relationship agrees with the theory that plastic deformation can control crack initiation and Stage I cracking¹⁴⁴ in nitrate solutions; it is also compatible with an apparent activation energy for Stage I crack growth that is similar to either the activation energy for oxide growth or the activation energy for interstitial atom diffusion (and the effect of interstitials on plasticity in steels). Thus the relationship between K_{scc} and yield strength supports a strain-assisted dissolution mechanism of nitrate cracking with crack initiation controlled by oxide rupture. Plasticity appears to promote crack initiation in nitrate solutions, and this agrees with the observed incidence of IG cracking beneath strain-induced cracks in a magnetite surface film.⁸⁸ Oxide rupture would be easier in low yield strength microstructures than

in high yield strength microstructures.

The relationship between K_{scc} and yield strength in Stage I nitrate cracking in the present study (Figures 63-64), agrees with the results of Henthorne and Parkins.⁵⁶ They found that in constant strain rate tensile tests a so-called crack initiation stress was proportional to the yield stress of various grain sizes of steel produced by heat treatment.

The yield strength dependence of K_{scc} is compatible with the relationship of both K_{scc} and yield strength with temperature. Both K_{scc} and yield strength were nearly constant in the range of testing temperature (Figure 69, Table 7). If cracks were initiated by oxide rupture, then the effect of temperature on both K_{scc} and yield strength should have been similar, as observed in this study.

While the relationship between K_{scc} and yield strength supports a strain-assisted anodic dissolution mechanism, hydrogen embrittlement cannot be ruled out entirely. The increase in K_{scc} with increasing yield strength in mild steel does not agree with the relationship between susceptibility to or severity of hydrogen embrittlement and yield strength in high strength steels. In the aqueous SCC of a large number of alloy steels, generally thought to occur by a hydrogen-induced mechanism, K_{scc} is inversely proportional to yield strength.¹¹¹ However, the relationship between yield strength and susceptibility to hydrogen embrittlement in low strength steels has not been well documented, and others have suggested that SCC in such alloys might be due to hydrogen.¹⁴⁸ For instance, while increasing temperature would increase the corrosion rate and the rate of cathodic generation of hydrogen, increasing temperature in the range of the present tests would also diminish the severity of gaseous hydrogen

embrittlement of mild steel.¹⁴⁹ Thus the opposing effects of increased temperature might have cancelled each other and led to a constant K_{scc} in the temperature range of testing, as observed in the present study (Figure 69).

The primary influence of microstructure on cracking seemed to be due to yield point rather than carbide morphology. The HR and N microstructures were both pearlitic but had very different yield points and very different K_{scc} values (Figures 63-64). Similarly, the finely spheroidized S structure and coarsely spheroidized QS structure had identical grain size but widely different yield points and K_{scc} values (Figure 64).

Microstructural influences other than yield point also had an effect in K_{scc} and over-rode the yield point effect in specific cases (Figures 63-64). From a yield point consideration one would expect the HS structure to exhibit the lowest K_{scc} , but evidently it did not (Figure 64). The resistance of the HS microstructure to IG corrosion and cracking appeared to be much higher than for other microstructures of similar phase morphology but smaller grain size and higher yield strength (i.e., NS and QS structures). The importance of anodic dissolution, especially in Stage II cracking, indicated that the corrosion susceptibility of the various microstructures also was of importance in determining cracking susceptibility at low stress intensities.

Attempts were made to determine the reason for HS cracking resistance by analyzing grain boundaries in both HR and HS material using an electron microprobe at Savannah River Laboratory and at the Georgia Engineering Experiment Station (located at Georgia Institute of Technology).

These studies were intended to establish concentration profiles for carbon or other interstitial and substitutional trace elements such as nitrogen, oxygen and sulfur by slow scanning across grain boundaries. Electron microprobe studies of quenched steel by Eichen, et al., showed that carbon concentrations increased as one approached a grain boundary at the edge of a transformed austenite (martensite) grain.¹⁵⁰ Carbon levels dropped off below the limit of detectability as the electron beam crossed the grain boundary into a grain of ferrite. Unfortunately, no such concentration profiles could be obtained by the microprobe techniques utilized in this study due to insufficient sensitivity or absence of a large gradient. Thus explanation of the apparent resistance of HS material to cracking at low stresses remained unknown.

The NS and QS microstructures had identical prior austenite grain sizes and differed primarily in ferrite grain size and volume fraction. QS specimens had somewhat smaller ferrite grains than NS specimens, but both microstructures had identical phase structures and nearly identical K_{scc} 's (Figure 64). One would expect the carbon distributions in these materials to be nearly at equilibrium for 977°K and thus very similar.¹⁵¹ This may account for the nearly identical K_{scc} 's despite the substantial difference in yield points.

Comparison of the K_{scc} values for the NS and QS microstructures with the N and S microstructures (Figure 64) indicates that long term spheroidization reduced both the yield point and K_{scc} . However, the lack of a clear yield point dependence of K_{scc} between either the N and S or the NS and QS structures further supports the contention that grain boundary chemistry effects are also important at low stress. The results

of spheroidization agreed with Parkins observation that spheroidization worsened susceptibility to nitrate cracking.²⁷

The WOL tests of quenched and tempered steel, QT11, indicated that the primary effect of this heat treatment was to raise K_{sc} . The primary effect of quenching and tempering at 866°K was to shift the crack velocity-stress intensity curve to higher stress intensities rather than to shift the curves lower in crack velocity (Figure 68). The WOL specimen tests agreed with results of Uhlig and Sava⁶² and Houdrement, et. al.,⁶⁹ who studied tempering effects on susceptibility to nitrate cracking. Both of those investigations showed that fairly short term tempering at temperatures between about 300° and 700°C were beneficial. Increased tempering times, as represented by the S and QS microstructures decreased K_{sc} (Figure 64). This was compatible with Uhlig and Sava's work which showed the same deleterious effect of prolonging tempering time.⁶²

The exact mechanism by which tempering affected susceptibility to nitrate cracking in steel is not clear. Certain observations made in the present study, however, pointed to a phenomenon that behaved similar to aging effects. Tensile tests revealed there was an increase in upper yield point (proportional limit) of the QT11 microstructure compared to the Q and QT4 structures (Tables 5-6 and Figures 34-38). With longer (and higher temperature) tempering as represented by the S and QS structures the yield point diminished. This behavior was paralleled by the increase and then decrease in cracking resistance as measured by K_{sc} of the QT11 and the S and QS structures with respect to the original Q microstructure. (The Q microstructure K_{sc} was well below that of QT11

but could not be accurately determined relative to the S and QS structures.) The parallel in yield point and SCC behavior emphasized the importance of yield point and plasticity in IG cracking. The trends in yield point and SCC resistance resembled the type of property changes that result from strain aging or quench aging of steel, however in quench aging the kinetics of the process are much faster.¹³⁷ Interestingly, maximum susceptibility to cracking occurs at a carbon content in the range of maximum carbon solubility in ferrite,^{32,37} and this range of carbon contents also corresponds to the composition range for maximum aging effects. Aging effects are generally associated with interstitial atoms (carbon or nitrogen) locking dislocations,¹³⁷ and the activation energy measured for the onset or loss of susceptibility to nitrate cracking with tempering time has been reported at 92-109 kJ/mole (22-26 kcal/mole).⁶⁴ This is compatible with carbon and nitrogen atom diffusion in ferrite and underscores the importance of interstitial atom influences on mechanical properties and cracking.

According to studies cited by McLean,¹⁵¹ a large concentration of carbon forms in ferrite grain boundaries if the cooling velocity is slow enough to allow a buildup toward the equilibrium grain boundary concentration. The equilibrium carbon concentration in ferrite grain boundaries is inversely proportional to temperature,¹⁵¹ and quick cooling can suppress diffusion and result in low grain boundary carbon concentrations. Thus rapid quenching of the Q microstructure trapped considerable carbon in solution within grains (as in the entrapment detected by electron microprobe¹⁵⁰), but such quenching caused low concentrations of carbon in grain boundaries. Short-term heat treatment at intermediate temperatures (QT11)

resulted in higher grain boundary concentrations of carbon as the carbon entrapped in grains adjacent to the boundary diffused into the disordered boundary region and relaxed the elastic strain in both the adjacent grains and the grain boundary. Such relaxation of strain reduced dissolution of the steel near the boundary. This would explain the resistance of QT11 material to cracking, and it agrees with the results of Flis who claimed that the beneficial effects of slow cooling or low temperature heat treatments are due to increased accumulation of carbon at grain boundaries.³⁷ With prolonged tempering at higher temperature, as in the S and QS microstructures, the grain boundary concentration was reduced to the lower equilibrium value for this temperature.¹⁵¹ This effect and the reduction in yield point acted to increase susceptibility to cracking progressively in the S and QS microstructures (Figure 64).

This view of the effect of heat treatment on quenched structure SCC properties agrees with the results of Uhlig, et. al., who showed a difference in nitrate cracking behavior of quenched and of slowly cooled or spheroidized steel with varying carbon content.¹²³ While increasing carbon content was beneficial in the case of slowly cooled and spheroidized steels, quenched steel became quite susceptible with increasing carbon content and remained this way up to 0.2% C. The detrimental effect of carbon in quenched material seems to result from the large amount lattice strain induced by quenching and the freezing-in of nonequilibrium carbon distributions and resulting effect on grain boundary dissolution. The beneficial effects of carbon in slowly cooled and spheroidized steels, especially at concentrations over 0.0294% C^{37,59} seem due to increasing yield point with carbon content. Carbon additions above the

point of maximum carbon solubility would have little effect on grain boundary chemistry of slowly cooled steels since ferrite grains would remain at their saturation concentration of carbon. Additional carbon would only increase the volume fraction of pearlite grains.

Stage II Cracking

Effect of Temperature. Since crack velocity was virtually independent of stress intensity in Stage II cracking (Figure 68-69), the rate controlling process in Stage II cracking would be expected to be corrosion controlled rather than stress controlled. This is compatible with the estimated activation energy for Stage II cracking of 15 kJ/mole (4 kcal/mole) measured in this study. The measured value agrees fairly well with activation energies for dissolution of iron and steel in nitrate solutions of 21-25 kJ/mole (5-6 kcal/mole)³¹ and 22 kJ/mole (5.2 kcal/mole).¹⁵² Thus the kinetics of Stage II nitrate cracking of mild steel support a dissolution mechanism rather than hydrogen-assisted cracking, which has measured activation energies of the order of 33-38 kJ/mole (8-9 kcal/mole).¹⁵³

Interestingly, the activation energy for crack growth rate in aluminum alloy-chloride solution SCC also has been reported as 15 kJ/mole in Stage II cracking, and the activation energy for Stage I cracking is also much higher than for Stage II cracking.¹⁵⁴ These similarities in the kinetics of SCC of both aluminum alloys in chlorides and mild steels in nitrates suggest a common mechanism, strain-assisted anodic dissolution,¹⁴⁴ and increase the measure of confidence in the activation energies measured in the present study.

Relationship to Anodic Dissolution. Crack velocity can be related

to anodic current density by use of a simple mass balance that equates the rate of metal dissolution to the rate of current flow. From such a relationship one can obtain the equation:

$$\frac{dl}{dt} = \frac{A i}{\rho n F} \quad (10)$$

where " dl/dt " is the crack velocity, " A " is the atomic weight of the dissolving metal, " i " is the current density, " ρ " is the metal density, " n " is the charge of the cation produced and " F " is Faraday's constant. For typical Stage II crack velocities on the order of $0.01 \mu\text{m/s}$ (Figure 68), the corresponding current density from Equation (10) would be on the order of 2.6 mA/cm^2 , well within the range of current densities obtained in anodic polarization experiments conducted at pH 3.5 or pH 6.0 (Figures 72-73). In fact, the maximum crack velocities seen in Stage III cracking of CT specimens (about $0.1 \mu\text{m/s}$ in Figure 69) are equivalent to a current density of 26 mA/cm^2 , far below the critical passivating current density in a pH 6 nitrate solution (Figure 73). One would expect acidic nitrate at a crack tip to give even higher maximum current densities than a pH 6.0 solution. Such arguments, along with the apparent activation energy for Stage II cracking of 15 kJ/mole (4 kcal/mole) support an anodic dissolution mechanism and indicate that it is theoretically feasible. This does not even account for the stimulating effect of straining on metal dissolution which could increase the maximum attainable anodic current densities,^{98,99} nor does it account for the inhibiting effect of gradually increasing solution pH during the course of polarization tests. The results of the present study agreed with conclusions of Hoar and Galvele

that anodic dissolution was the most probable cause of cracking based upon such current density considerations.¹²⁸ Hoar and Galvele related the increase in current density on tensile specimens to breaks in the surface film, and they related measurements of the depth of microcracks to the anodic current density. In this manner they accounted for crack depth entirely on the basis of anodic dissolution.

There were certain inconsistencies between a purely anodic dissolution mechanism or a mechano-anodic (activated dissolution) model of nitrate cracking and the observed Stage I-Stage II cracking behavior. First, a mechano-anodic model would not explain the observed Stage II cracking in which increasing stress intensity appeared to have little effect upon crack velocity. Also, a purely dissolution or activated dissolution model would not predict the apparent lack of effect of temperature on K_{scc} . Other phenomena must enter into the overall process. For instance, crack initiation and the rapid initial rise of crack velocity with stress in Stage I cracking may be due to both film rupture and activation of dissolution by applied stress. Pits on corrosion coupon (Figure 71) were filled with oxide, and this oxide would block solution replenishment and corrosion propagation. Any outside influence such as stress which would rupture the oxide film would also aid continuance of the corrosion penetration process. The stable velocity in Stage II cracking appears to result from opposing processes such as anodic dissolution and crack tip solution replenishment from the bulk solution. While stress may increase the dissolution rate, the straining would also stimulate flow of bulk solution into the growing crack. The crack velocity that results seems to be a dynamic balance that includes anodic dissolution, which

depletes crack tip pH, and solution replenishment, which tends to raise crack tip pH.

Stage III Cracking

Effect of Temperature. The activation energy for crack growth rate measured in the Stage III cracking region by use of CT specimens also suggests that the mechanism of cracking is strain-assisted anodic dissolution. The value of 60-70 kJ/mole (15-17 kcal/mole) obtained in the present study is compatible with rate control at high stress intensities by solid state diffusion of interstitial atoms that have similar activation energies as discussed previously. Not only might interstitial atoms produce chemically susceptible paths for corrosion at grain boundaries,³⁸ but such species might control the micromechanical behavior of the metal at the crack tip.¹³⁷ Although it is not known at this time precisely what the critical rate determining process is at the crack tip, it seems reasonable that at high stress intensities it is a mechanical or solid-state-diffusion-controlled process.¹⁴⁴ In the limiting case of raising the stress intensity to the ductile overload point, of course, fracture kinetics become entirely mechanically controlled.

Effect of Microstructure. Crack velocities measured in constant load CT specimen tests were inversely proportional to the yield strengths of the various microstructures (Figures 57 and 62). Such a relationship between crack growth rate and yield strength indicated an enhancement of crack growth by plastic deformation; this effect caused low strength heat treatments to propagate cracks more rapidly than higher strength heat treatments. Enhancement of crack growth by plasticity occurred in both synthetic nuclear waste and pure nitrate solutions. These results

are compatible with the activation energy measured for Stage III cracking and also indicate a strain-assisted anodic dissolution mechanism of nitrate cracking. Enhancement of cracking by plasticity (strain) could be controlled by diffusion of interstitial C or N atoms.¹³⁷

The increase in crack velocity with increasing stress intensity seemed to saturate in Stage III cracking; that is, the crack velocity seemed to become nearly constant at high stress intensities (Figure 69). A possible explanation for the apparent saturation of crack velocity is the multiple crack branching near the ductile overload point (Figure 45). The formation of two crack branches would reduce the effective stress intensity to approximately $(2)^{-1/2}$ times the original crack tip stress intensity.¹⁵⁵ The reduction in stress intensity would reduce crack velocity as well.

The crack branching observed in this study seemed to follow the experimental observations of Syrett and Trudeau.¹⁵⁶ Their experiments showed that crack branches in the SCC of high strength steels started at an initial included angle of $2\pi/3$ radians (120°) and tapered off to $\pi/3$ radians (60°) further from the origin of branching. This matches the measurements made in the present study (Figure 45). The explanation offered by Syrett and Trudeau was that SCC tended to propagate along zero isoclinic planes, i.e., planes of zero shear stress. Using linear elastic fracture mechanics it was shown that such planes were at angles of $\pm\pi/3$ radians from the plane of a large, sharp crack, and these angles diminished with distance from the crack tip to about $\pm\pi/6$. These propagation paths were proposed for plane stress conditions as well as plane strain conditions.

Another model for crack branching is found in a computer simulation of cracks under plane stress loading by Yamada, et al., who predicted large branch-like plastic zones at the crack tip.¹⁵⁷ Their results, based on plasticity theory, showed plastically deformed lobes that were at angles not unlike those measured by Syrett and Trudeau¹⁵⁶ and those observed in the present study. One could rationalize in a qualitative fashion that if cracks propagated along planes of maximum effective stress rather than planes of zero shear stress, then they would propagate along the centerlines of the plastic zone lobes. In other words, in a strain-hardening material like mild steel the maximum stress would occur at the locations which had undergone the maximum amount of strain, i.e., at the centerlines of the plastic lobes.

Another possible reason for the apparent saturation of Stage III crack velocity might have been small, stepwise increases in crack opening displacement that became more accentuated near the end of CT specimen tests (not shown in Figures 43 or 59). These discontinuities seemed to be related to localized ductile fracture of corrosion-undermined ligaments seen on SCC fracture surfaces (perhaps accentuated by Portevin-le Chatelier effect¹³⁷), and they might have caused a retarding effect on subsequent crack growth. Each time the specimen suddenly yawned open, fresh solution would have been drawn into the yawning crack, and crack tip chemistry conditions would have been disturbed. This could have slowed crack growth until the optimum crack tip chemistry conditions for cracking were reestablished. Displacement-time curve slopes from the chart recorder system were, in fact, smaller between the stepwise increases in crack opening displacement than were the overall slopes of the curves as

represented by Figures 43 and 59. The apparent slowing of crack growth between the stepwise increases in displacement indicated that the discontinuous process was not responsible for the enhancement of crack growth by plasticity. It appeared that discontinuous increases in crack opening displacement would have slowed crack propagation in low yield strength microstructures where the discontinuities were more numerous.

A Mechanism of Caustic-Nitrate Cracking of Steel

Based upon the results of this study and the data in the literature, the following general description of caustic-nitrate cracking of steel has been formulated. Many of the important atomic scale processes are yet imperfectly understood and subject to controversy.

Role of Nitrate Ion

The nitrate ion appears to be particularly damaging because of its imperfect passivation of steel. At low pH concentrated nitrate solutions corroded steel surfaces and allowed very high anodic current densities to flow from the metal (Figure 72). At nearly neutral pH, very high anodic currents could flow, but some evidence of passivity was seen at high current densities (Figure 73). At high pH passivation occurred, but such passivation was metastable. Localized breakdown of the passive film caused pitting, and accelerated dissolution occurred in the pits (Figure 74).

The imperfect passivation ability of the nitrate ion is demonstrated by other findings as well. Tribo-ellipsometry studies showed that nitrate ion was much less able to passivate steel than nitrite ion.¹⁵⁷ Much more anodic current flowed after film disruption in nitrate solutions than in nitrite solutions. Additionally, it is well known that dilute nitric acid

will attack steel, but concentrated nitric acid will passivate steel.¹⁵⁸

In a similar fashion, additions of nitrate ion up to about one molar in aerated solutions will accelerate steel corrosion, but at higher concentrations the nitrate ion begins to inhibit corrosion.¹⁵⁹

The chemical reactions in the iron-nitrate water system are extremely complicated.¹⁶⁰ Dissolution of iron in dilute nitric acid is an obscure process that is not well understood.¹⁶¹ The vigorousness of the reaction indicates an autocatalytic dissolution mechanism involving intermediate species such as NO, NO₂, HNO₂ and Fe(NO)·(NO₃)₂.^{158,161} The production of NH₃ and NH₂OH are also involved.¹⁶¹

Role of Hydroxide Ion

The hydroxide ion acted as an inhibitor of nitrate solution corrosion and nitrate SCC in synthetic caustic-nitrate nuclear waste and similar nitrate solutions. Hydroxide ion both passivated steel corrosion in nitrate solutions (Figures 73-74) and inhibited cracking by raising K_{scc} (Figure 63).

In general, the amount of passivating ion that must be added to nitrate to inhibit cracking follows the so-called Freundlich isotherm,¹⁶² found by Matsuda and Uhlig¹⁶³ and by Legault, et al.,¹⁶⁴ to govern inhibition of general corrosion. That is, the concentration of passivating ion required to prevent attack increases with the concentration of aggressive ion according to the relationship

$$\log [M_p] = a - b \log [M_a], \quad (11)$$

where "[M_p]" is the concentration of passivating (hydroxide) ion, "[M_a]"

is the concentration of aggressive (nitrate) ion and "a" and "b" are constants. It is not known if such a relationship adequately describes nitrate cracking of precracked fracture specimens in which the solution chemistry in the crack appears to be quite different than in the bulk solution (Figure 46). However, since addition of 0.47M hydroxide ion to 5M NaNO_3 at 370°K did not prevent cracking of CT specimens at an initial stress intensity below the ductile overload point, it would appear that this concentration of hydroxide was below a possible $[M_p]$ for the test conditions.

Role of Microstructure

Assuming that nitrate ion promotes imperfect passivation of steel, one must examine the preference of nitrate cracking for grain boundaries and the effect of heat treatment and microstructure upon this preference. The results of the present study indicated that annealing or tempering heat treatments increased the resistance of a structure to nitrate cracking, especially when they achieved an increase in yield point as well (Figures 57 and 62-64). For example, the N and QT11 heat treatments represented such annealing and tempering operations on the HR and Q structures respectively. Long term tempering was detrimental as seen in the case of the S and QS and the NS heat treatments (Figures 62 and 64), presumably due to depletion of soluble grain boundary carbon.¹⁵¹

However, in general grain boundary regions remain anodic to the steel lattice as evidenced by grain boundary trenching (Figure 71), narrow grain boundary cracks (Figures 55-56) and the active potential measured at grain boundaries in steel.³⁸ This suggested that cracking was primarily due to anodic dissolution of grain boundaries.

Since interstitial elements such as carbon have a profound influence on nitrate cracking, they are generally cited as the reason for grain boundary susceptibility to cracking.^{32,37} The activation energies for crack growth rate in Stage I and Stage III nitrate cracking measured in this study are very similar to the activation energies for interstitial atom diffusion in ferrite. This also supports the role of interstitial atoms in promoting grain boundary susceptibility to nitrate cracking.

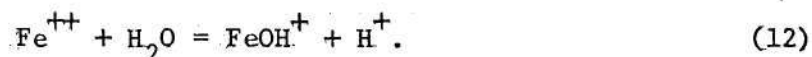
The influence of yield strength on susceptibility to nitrate cracking (Figures 57 and 62-64) demonstrates that yielding assists cracking. Such a yield point effect is opposite to the effect of yield point on aqueous cracking of high strength steels. This suggests that nitrate cracking is not due to hydrogen-assisted cracking as is the cracking of high strength steel.¹¹¹ Thus strain-assisted anodic dissolution seems to be a more plausible mechanism.

Role of Crack Tip Solution Chemistry

Fractographic evidence revealed apparent low pH solution conditions in cracks with etch pitting and free dissolution conditions near the crack tip (Figures 49, 55-56 and 71) and also magnetite formation in cracks (Figures 46-48, 61 and 65-66). Such features resembled occluded corrosion cell formation.¹²⁵ A low pH in a crack in steel is not surprising but has been verified only rather recently.^{111,115} It is well known that an anodic site in aqueous corrosion generates locally acidic solution conditions by hydroxide precipitation, and a cathodic site generates locally caustic conditions by hydrogen gas evolution.

The dissolution of iron in water¹⁶⁵ is probably the general anodic reaction during nitrate cracking of steel. Intermediate species and

nitrogen-bearing gaseous products may be involved in the complicated chemical reactions,^{158,160,161} but the overall reaction still appears to be iron dissolution and subsequent hydroxide and oxide formation (Table 9). Iron, except at very high impressed potentials, dissolves initially in the divalent state. Ferrous ions hydrolyze and establish acidic conditions as in:



The pH at the very tip of a propagating stress corrosion crack or pit in steel appears to be governed by the equilibrium represented by Equation (12)¹⁶⁶ in which the hydrolysis constant for the equilibrium (at 293°K)¹⁶⁷ is:

$$\frac{[\text{FeOH}^+][\text{H}^+]}{[\text{Fe}^{+2}]} = 10^{-7}. \quad (13)$$

Assuming that equal concentrations of FeOH^+ and H^+ ions are produced by the hydrolyzing ferrous ions, one arrives at the equilibrium:

$$\frac{[\text{H}^+]^2}{[\text{Fe}^{+2}]} = 10^{-7}, \quad (14)$$

or in other words

$$\text{pH} = 3.5 - \frac{1}{2} \log [\text{Fe}^{+2}]. \quad (15)$$

It has been found that stress corrosion cracks in steels in chloride solutions contain roughly $1\text{M } [\text{Fe}^{+2}]$.¹¹⁵ This corresponds to a pH of 3.5 using Equation (15), a value quite close to the measured pH of 3.7 to 3.9 in cracks and pits.¹¹⁵ This is the pH obtained upon dissolving $1\text{M } \text{FeCl}_2$, FeSO_4 or $\text{Fe}(\text{NO}_3)_2$ in water, although in the case of ferrous nitrate there will be some oxidation of ferrous to ferric ion and a somewhat more acidic pH with time. However, even substantial changes in the ferrous ion concentration, for instance from $0.1\text{M } [\text{Fe}^{+2}]$ to $10\text{M } [\text{Fe}^{+2}]$, will only change the equilibrium pH from 4.0 to 3.0. Furthermore, formation of $\text{Fe}(\text{NH}_3)_x$ complexes and a drastically reduced ferrous ion concentration would not be favored by acidic crack tip conditions. The first two stability constants for the complex $\text{Fe}(\text{NH}_3)_x^{+2}$ are $K_1 = 10^{1.4}$ and $K_2 = 10^{0.8}$.¹⁶⁷ This indicates that very little ferrous ion will be complexed. In fact, substantial complexing can only occur in a concentrated ammonia solution of high pH.^{160,167} Thus in the case of nitrate cracking we might expect establishment of a crack tip pH on the order of pH 3.5 at room temperature. The temperature of the solution will affect the crack tip pH somewhat, and extrapolation of hydrolysis constant data¹⁶⁷ for the equilibrium in Equation (12) indicates that the equilibrium pH is reduced by one pH unit from 293°K to 373°K ($20^\circ\text{--}100^\circ\text{C}$).

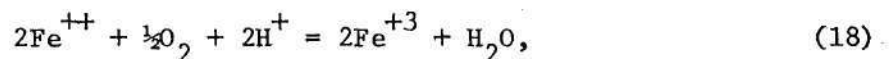
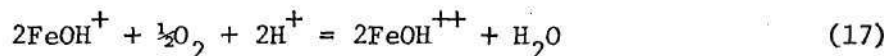
An acidic crack tip pH in a nitrate solution favors free dissolution of iron.^{124,160} Polarization experiments in such solutions verified free dissolution, a blue-green color in solution (ferrous ion) and very high anodic current densities (Figure 72). The current densities obtained in the polarization experiments could account for observed crack velocities solely on the basis of anodic dissolution. These factors, and

the clean, freely corroding appearance of a narrow region at a propagating crack tip (Figure 49), all support anodic dissolution as the mechanism of nitrate cracking.

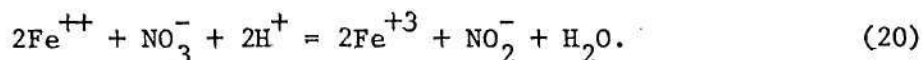
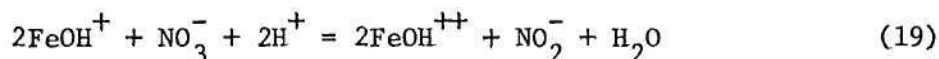
Other chemical reactions occur that maintain the crack tip acidic and produce magnetite some distance away. Precipitation of ferrous hydroxide also consumes hydroxyl ions and helps to maintain acidification at the crack tip:



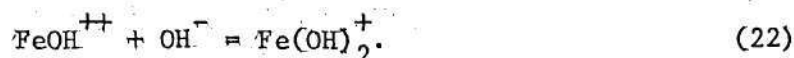
Dissolved ferrous species diffuse away from the crack tip and are oxidized by dissolved oxygen or nitrate ions:



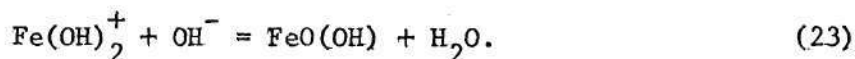
or alternatively:



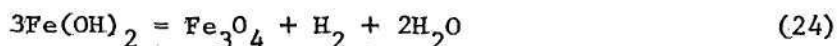
Ferric ions subsequently hydrolyze and thus consume hydroxyl ions also:



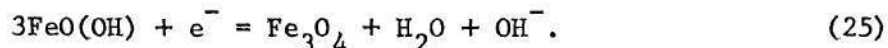
Diffusion of the soluble iron products to regions of increasing hydroxide concentration results in formation of precipitates such as goethite. The exact mechanism, as in rust formation, is complex and not completely understood,¹⁶⁸ however these reactions may include¹⁰⁹



Also in intermediate pH regions such reactions as the well-known Schikorr reaction



or some similar reaction produces magnetite on crack surfaces behind the advancing crack tip. The possibility also exists for magnetite growth by goethite precipitation at the oxide-solution interface:¹⁰⁹



Recall in the present study that hydrated $\text{FeO}(\text{OH})$ was found overlaying magnetite in newly initiated nitrate cracks which were subsequently fractured open (Table 9). The goethite was loose and powdery, apparently precipitated out of solution onto the adherent magnetite film as expected from Equation (23). It was also found in this study that cracks which arrested themselves under decreasing load showed no goethite, only magnetite on crack surfaces. Apparently crack arrest was accompanied by depletion of ferrous and ferric ions through magnetite formation.

Several cathodic reactions might occur during nitrate cracking.

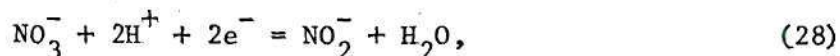
These include hydrogen ion reduction:



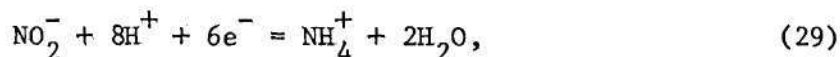
oxygen gas reduction:



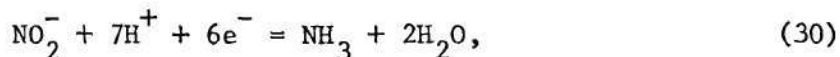
nitrate ion reduction to nitrite ion:



nitrite ion reduction to ammonium ion



nitrite ion reduction to ammonia



and various gas evolution reactions involving N_2 , N_2O , NO , NO_2 and N_2O_4 .¹⁶¹ All such reactions involve depletion of hydrogen ions and thus an increase in local pH. If the anodic and cathodic reactions occurred in close proximity or if mixing occurred, crack tip acidity could not be sustained. The bulk of these cathodic reactions would then, by necessity, occur some distance from an anodic crack tip.¹⁶⁹ It is

not known whether the gas evolved from pits in polarization electrodes in 5M NaNO_3 at pH 13.7 was one such cathodically generated species. In models of pitting, cathodic gas evolution is thought to occur at the oxide-bulk solution interface at the mouth of pits.¹⁰⁹ In fact, even at an anodic potentials, hydrogen evolution has been seen during pitting of steel.¹⁷⁰ The applied potential seemed much too low, however, to allow oxygen evolution by oxidation of water.¹²⁴

In the present study the open circuit potentials of polarization specimens initially immersed in nitrate solutions at low pH were sufficiently negative to cathodically reduce hydrogen.¹²⁴ However, hydrogen evolution in close proximity to the crack tip would increase the pH and would tend to diminish anodic dissolution. It is not known whether the pH and potential in cracks could sustain hydrogen evolution and hydrogen-assisted cracking in mild steels in nitrate solutions. The suggestion has been made that anodic dissolution and hydrogen embrittlement could act synergistically.¹⁴⁸ However, it is difficult to conceive of sustained anodic and cathodic reactions occurring in extreme proximity.

Role of Oxide Film

The role of the magnetite film present on crack surfaces appears to be twofold. Magnetite buildup impedes bulk solution ingress to a crack tip and allows an occluded corrosion cell to form. In the absence of a significant driving force such as stress, magnetite will block solution replenishment and impede corrosion as seen in unstressed corrosion coupon pits (Figure 71). The other effect of magnetite is to polarize filmed surfaces and allow them to become noble (local cathodes) with respect to the unfilmed metal at a propagating crack tip. This

would restrict corrosion to the most active locations and intensify the rate of intergranular penetration. Disruption of such a magnetite film would provide sites for preferential cracking.⁸⁸ The stimulating effect of anodic polarization in causing complete IG failure of unstressed specimens might be explained by the vigorous gas evolution observed in the present study. Gas pressure would force through the magnetite film, and such a disruption could prevent stifling of the anodic reaction.

Crack arrest (and presumably initiation) in nitrate solutions seemed to be controlled by oxide rupture. The activation energy for crack growth rate measured near K_{scc} was similar to the activation energy for magnetite formation on steel.^{145,146} The elevation of K_{scc} by increasing yield strength (Figures 63-64) also supported such a concept.

Role of Stress

The role of stress appears to be twofold as well. First straining is necessary to disrupt the impeding effect of magnetite on corrosion in a narrow crack.⁸⁸ The second role of stress is to stimulate anodic dissolution.^{98,99} With regard to the latter role, the large defect density generated by stress at the crack tip will cause a large increase in the number of preferred sites for dissolution. Although no evidence of preferential attack of static dislocations has been found in nitrate solutions,^{55,113} a mechano-anodic effect may arise from dynamic processes.

The oxide rupture role of stress appeared to predominate at crack arrest as discussed previously. At higher stress intensities in Stage III cracking one would expect the crack tip to be deforming sufficiently to cause extensive oxide rupture. Rate control at such high stress intensities

might involve activated dissolution of the straining crack tip in an acidic environment. Theoretical calculations and experimental measurements have shown activated dissolution of metals in acids to occur with activation energies of about 42-84 kJ/mole,¹⁷¹ compatible with the Stage III activation energy of 62-70 kJ/mole measured in this study.

CHAPTER V

CONCLUSIONS

1. The microstructure of mild steel affects caustic-nitrate cracking principally by variation of yield strength and corrosion susceptibility of grain boundaries.

2. Caustic-nitrate cracking is stimulated by plasticity and is generally worse in low yield strength microstructures.

3. Tempering heat treatments such as those used in stress relief may produce inherently crack-resistant microstructures in mild steel.

4. Caustic-nitrate cracking seems to be due to strain-assisted anodic dissolution because of considerations such as apparent crack tip solution chemistry, cracking kinetics and the effect of plasticity on cracking; hydrogen embrittlement is also a possibility.

5. Caustic-nitrate cracking appears to occur under "occluded corrosion cell" acidic crack tip chemistry conditions which are compatible with a dissolution or hydrogen embrittlement mechanism.

6. Observed crack velocities are compatible with anodic dissolution rates.

7. Caustic-nitrate cracking of mild steels in synthetic nuclear waste solutions is essentially nitrate cracking.

CHAPTER VI

RECOMMENDATIONS

1. Future SCC studies should concentrate upon crack initiation and crack arrest data, the only true measures of complete elimination of SCC. As was seen in the present study, a shiny, uncorroded outer surface is no indication of immunity to cracking. Dead weight loaded CT specimen tests may complement crack arrest data as in the present study, but tapered (constant stress intensity) double cantilever beam specimens⁵¹ would provide more quantitative crack velocity information than do compact tension specimens.

2. The effect of tempering should be examined with respect to fine structure not resolved by the techniques used in this study. Specifically, transmission electron microscopy could be utilized along with microhardness measurement to verify grain boundary carbon content and ridging due to such effects.⁵⁴

3. Pure iron-carbon alloys of high purity should be heat treated to give coarse grain sizes that can be examined for the effect of heat treatment on carbon distribution by electron microprobe. It is recommended that discrete stepwise scanning be used instead of the constant speed scan techniques attempted in this study.

4. The interesting effect of temperature on K_{SCC} and crack velocity should be pursued through a wider temperature range. It should also be related to mechanical, hydrogen embrittlement and chemical dissolution behavior of the same alloy in the extended temperature range.

This would help to distinguish the cracking mechanism.

5. Experimental pH-potential measurements in nitrate cracks should be attempted by use of microelectrodes or other techniques to verify occluded corrosion cell conditions.

6. Nitrate cracking behavior should be related to plasticity theory. Especially useful would be a parameter to replace stress intensity factor that would be valid in the transition between plane stress and plane strain conditions.

7. The gas evolved from pits in anodically polarized steel electrodes in caustic-nitrate solutions should be analyzed. This might clarify the reactions occurring during cracking.

8. Further fundamental studies into the nature of nitrate ion and nitric acid dissolution and passivation of iron are needed before any detailed explanation of nitrate cracking can be achieved.

APPENDIX A

TABLES

Table 1. ASTM Specification A 516 Grade 70 (Reference 129).

A. Max. Plate Thickness for Fusion Welding:	8 inches
B. Method of Production:	Open Hearth, Basic Oxygen, Electric Furnace, Vacuum Arc Remelt, Electroslag Remelt
C. Austenite Grain Size:	5 or Finer
D. Chemical Requirements:	<u>%</u>
1. Max. C	
a. $\frac{1}{2}$ inch thickness & under	0.27
b. Over $\frac{1}{2}$ -2 inches thickness, incl	0.28
c. Over 2-4 inches thickness, incl	0.30
d. Over 4-8 inches thickness, incl	0.31
e. Over 8 inches thickness	0.31
2. Manganese	
a. Heat Analysis	0.85-1.20
b. Product Analysis	0.80-1.25
3. Max. Phosphorus	0.035
4. Max. Sulfur	0.04
5. Silicon	
a. Heat Analysis	0.15-0.30
b. Product Analysis	0.13-0.33
E. Tensile Requirements:	
1. Tensile Strength (ksi)	70.0-90.0
2. Min. Yield Strength (ksi)	38.0
3. Min. Elongation in 8 inches (%)	17
4. Min. Elongation in 2 inches (%)	21
F. Fabrication:	
1. $1\frac{1}{2}$ inches thickness & under	As Rolled
2. Over $1\frac{1}{2}$ inches thickness	Normalized

Table 2. Bethlehem Steel Corp. Test and Analyses of A 516 Grade 70.

A. Heat Number	518X0796
B. Yield Strength (ksi)	47.6
C. Tensile Strength (ksi)	76.2
D. Elongation in 8 inches (%)	28
E. Composition (%)	
1. Carbon	0.21
2. Manganese	1.09
3. Silicon	0.24
4. Phosphorus	0.010
5. Sulfur	0.029
F. Austenite Grain Size (ASTM)	6 to 8

Table 3. Heat Treatment Schedule.

<u>Specimen Designation</u>	<u>Heat Treatment Name: Schedule</u>
HR	Hot Rolled: As-received
N	Normalized: 1108°K (1535°F) for 1 hr + air cooled.
Q	Quenched: 1108°K (1535°F) for 1 hr + brine quench.
QT11	Quenched & Tempered: Q + 866°K (1100°F) for 1 hr + air cooled.
QT4	Quenched & Tempered: Q + 478°K (400°F) for 1 hr + air cooled.
S	Spheroidized: Q + 977°K (1300°F) for 4 hr + air cooled.
SQ	Spheroidized & Quenched: Q + 977°K (1300°F) for 4 hr + brine quench.
HS	Hot Rolled & Spheroidized: HR + 977°K (1300°F) for 72 hr + air cooled.
NS	Normalized & Spheroidized: N + 977°K (1300°F) for 72 hr + air cooled.
QS	Quenched & Spheroidized: Q + 977°K (1300°F) for 72 hr + air cooled.

Table 4. Composition of H-Area Purex Waste (Reference 5).

<u>Component</u>	<u>Concentration (w/o)</u>
NaNO_3	36.6
NaOH	1.1
Na_2SO_4	2.3
MnO_2	0.6
$\text{Fe}(\text{OH})_3$	0.5
KNO_3	0.3
H_2O	58.5

Table 5a. Tensile Properties of A 516 Grade 70 at 370°K, $\dot{\epsilon}_0 = 8.3 \times 10^{-5} \text{ s}^{-1}$.

Heat Treatment	Orientation	Upper Yield Stress MPa (ksi)	Lower Yield Stress MPa (ksi)	Ultimate Tensile Stress MPa (ksi)
Q	TL	456, [†] 457 [†] (66.1, 66.3)	345, ^{††} 348 ^{††} (50.0, 50.5)	710, 716 (103.0, 103.9)
QT4	TL	421, [†] 441 [†] (61.0, 64.0)	345, ^{††} 352 ^{††} (50.0, 51.0)	657, 696 (95.3, 100.9)
S	TL	334, 336 (48.4, 48.7)	322, 325 (46.7, 47.1)	445, 446 (64.5, 64.7)
N	TL [*]	331 (48.0)	315 (45.7)	471 (68.3)
N	LT	318, 336 (46.1, 48.7)	311, 323 (45.1, 46.9)	474, 481 (68.7, 69.8)
HR	TL [*]	272 (39.5)	269 (39.0)	484 (70.2)
HR	LT	274, [†] 275 (39.7, 39.9)	270, ^{††} 274 (39.2, 39.7)	485, 502 (70.4, 72.8)

* Single specimen data

† 0.2% Offset yield stress

†† Proportional limit

Table 5b. Tensile Properties of A 516 Grade 70 at 370°K, $\dot{\epsilon}_0 = 8.3 \times 10^{-5} \text{ s}^{-1}$.

Heat Treatment	Orientation	Elongation (%)	Reduction in Area (%)	Strength [†] Coefficient MPa (ksi)	Strain [†] Hardening Exponent
Q	TL	12.8, 16.0	48.9, 49.1	1489 (216)	0.252
QT4	TL	12.8, 12.8	53.1, 57.3	1241 (180)	0.208
S	TL	22.2, 23.0	72.5, 77.1	786 (114)	0.210
N	TL [*]	24.4	67.5	903 (131)	0.249
N	LT	21.8, 23.0	60.5, 64.2	903 (131)	0.242
HR	TL [*]	17.8	56.9	965 (140)	0.258
HR	LT	18.2, 18.2	53.7, 56.2	1027 (149)	0.279

* Single specimen data

† Average value determined graphically

Table 6a. Tensile Properties of A 516 Grade 70 at 370°K, $\dot{\epsilon}_0 = 8.3 \times 10^{-6} \text{ s}^{-1}$.

Heat Treatment	Orientation	Upper Yield Stress MPa (ksi)	Lower Yield Stress MPa (ksi)	Ultimate Tensile Stress MPa (ksi)
QT11	TL	374, 384 (54.3, 55.7)	372, 376 (54.0, 54.5)	554, 561 (80.3, 81.4)
SQ	TL	350, 366 (50.8, 53.1)	343, 363 (49.8, 52.7)	501, 521 (72.6, 75.5)
S	TL	346, [†] 351 (50.2, 50.9)	332, ^{††} 347 (48.2, 50.4)	483, 499 (70.1, 72.4)
N	TL [*]	316 (45.9)	296 (43.0)	@
QS	TL	312, 314 [†] (45.2, 45.6)	301, 308 ^{††} (43.6, 44.6)	433, 438 (62.8, 63.5)
NS	TL	265, [†] 278 (38.5, 40.3)	265, ^{††} 275 (38.5, 39.9)	403, 403 (58.4, 58.4)
HR	TL [*]	269 [†] (39.0)	264 ^{††} (38.3)	507 (73.5)
HS	TL	239, 242 [†] (34.6, 35.1)	238, 241 ^{††} (34.5, 34.9)	401, 407 (58.2, 59.1)

* Single specimen data

† 0.2% Offset yield stress

†† Proportional limit

@ No data due to equipment malfunction

Table 6b. Tensile Properties of A 516 Grade 70 at 370°K, $\dot{\epsilon}_0 = 8.3 \times 10^{-6} \text{ s}^{-1}$.

Heat Treatment	Orientation	Elongation (%)	Reduction in Area (%)	Strength [†] Coefficient MPa (ksi)	Strain [†] Hardening Exponent
QT11	TL	17.5, 18.8	68.6, 68.8	1062 (154)	0.225
SQ	TL	18.8, 19.8	69.9, 70.0	889 (129)	0.199
S	TL	19.3, 21.2	72.4, 72.7	896 (130)	0.222
N	TL [*]	@	64.6	945 (137)	0.268
QS	TL	24.3, 25.4	73.0, 73.8	800 (116)	0.224
NS	TL	25.4, 26.3,	71.2, 71.5	793 (115)	0.261
HR	TL [*]	16.5	57.7	1151 (167)	0.299
HS	TL	22.8, 24.3	67.3, 67.4	786 (114)	0.249

* Single specimen data

@ No data due to equipment malfunction

† Average value determined graphically

Table 7a. Temperature Dependence of Tensile Properties of Hot Rolled
A 516 Grade 70 at $\dot{\epsilon}_0 = 8.3 \times 10^{-6} \text{ s}^{-1}$.

Temperature °K (°C)	Proportional Limit MPa (ksi)	0.2% Offset Yield Stress MPa (ksi)	Ultimate Tensile Stress MPa (ksi)
370* (97)	264 (38.3)	269 (39.0)	507 (73.5)
357* (84)	256 (37.1)	270 (39.1)	498 (72.3)
345* (72)	219 (31.8)	272 (39.4)	510 (73.9)
333* (60)	260 (37.7)	282 (40.9)	512 (74.3)
323* (50)	263 (38.2)	286 (41.5)	509 (73.8)

* Single specimen data, TL orientation

Table 7b. Temperature Dependence of Tensile Properties of Hot Rolled
A 516 Grade 70 at $\dot{\epsilon}_0 = 8.3 \times 10^{-6} \text{ s}^{-1}$.

Temperature °K (°C)	Elongation (%)	Reduction in Area (%)	Strength Coefficient MPa (ksi)	Strain Hardening Exponent
370* (97)	16.5	57.7	1151 (167)	0.299
357* (84)	16.0	58.2	1048 (152)	0.277
345* (72)	21.2	60.4	1131 (164)	0.308
333* (60)	21.7	63.3	1034 (150)	0.267
323* (50)	23.4	63.3	1034 (150)	0.269

* Single specimen data

Table 8. CT Specimen SCC Properties in H-Purex at 370°K, $K_{I1}=49.4 \text{ MPa(m)}^{\frac{1}{2}}$.

Heat Treatment	Orientation	Time to Failure $s \times 10^4$ (hr)	Average Crack Velocity $\mu\text{m/s}$ (mil/hr)	Calculated Constant Velocity $\mu\text{m/s}$ (mil/hr)
HR	TL	25, 29 (70, 80)	0.034, 0.036 (4.8, 5.1)	0.057 (8.1)
HR	LT	27, 34 (75, 95)	0.033, 0.039 (4.7, 5.5)	
N	TL*	32 (89)	0.0275 (3.9)	0.038 (5.35)
N	LT	26, 30 (72, 83)	0.029, 0.032 (4.1, 4.6)	
S	TL	35.6, 36 (99, 100.5)	0.026, 0.032 (3.7, 4.6)	
Q	TL	45, 52 (125, 145)	0.020, 0.023 (2.9, 3.3)	0.027 (3.85)
QT4	TL	41, 42 (115, 117)	0.019, 0.027 (2.7, 3.8)	

* Single specimen data

Table 9. Powder X-ray Diffraction of SCC Surface Oxides.

Black Oxide		α -Fe		Fe_3O_4	
$d(\text{\AA})$	I	$d(\text{\AA})$	I	$d(\text{\AA})$	I
2.52	W			2.532	100
2.065	VVW			2.099	20
2.025	VS	2.027	100		
1.61	VW			1.616	30
1.475	W			1.485	40
1.433	S	1.433	19		
1.17	S	1.17	30		

Loose Oxides		α -Fe		Fe_3O_4		α -FeO(OH)	
$d(\text{\AA})$	I	$d(\text{\AA})$	I	$d(\text{\AA})$	I	$d(\text{\AA})$	I
4.17	W					4.18	100
2.67	VVW					2.69	30
2.53	W			2.532	100		
2.44	W					2.45	25
2.24	VVW					2.25	10
2.18	VVW					2.19	20
2.02	VS	2.027	100				
1.47	M			1.485	40		
1.43	M	1.433	19				
1.17	VS	1.17	30				

Table 10. CT Specimen SCC Properties in 5M NaNO₃ at pH 6, 370°K,
 $K_{I1} = 49.4 \text{ MPa(m)}^{1/2}$, TL Orientation.

Heat Treatment	Time to Failure $s \times 10^4$ (hr)	Average Crack Velocity $\mu\text{m/s}$ (mil/hr)
HS	13, 13 (35, 37)	0.064, 0.0685 (9.1, 9.7)
HR	22, 24 (61.5, 65.5)	0.061, 0.063 (8.7, 9.0)
NS	10, 11 (28.5, 31)	0.058, 0.065 (8.2, 9.2)
QS	13, 14 (37, 40)	0.051, 0.056 (7.2, 8.0)
N	19, 19 (52, 54)	0.051, 0.059 (7.2, 8.4)
S	22, 25 (61, 70)	0.041, 0.043 (5.9, 6.1)
Q	41, 41 (113, 113)	0.038, 0.041 (5.4, 5.85)
QT11	98, 142 (273, 396)	0.0082, 0.012 (1.2, 1.6)

Table 11. K_{scc} of WOL Specimens in 5M NaNO_3 at pH 6.0 and pH 13.7, 368°K.

Heat Treatment	Initial Stress Intensity $\text{MPa(m)}^{1/2}$ $(\text{ksi(in)}^{1/2})$	K_{scc} in pH 6 Solution $\text{MPa(m)}^{1/2}$ $(\text{ksi(in)}^{1/2})$	K_{scc} in pH 13.7 Solution $\text{MPa(m)}^{1/2}$ $(\text{ksi(in)}^{1/2})$
HR	53.9 (49.0)	14.4 (13.1)	
HR	54.0 (49.1)		22.4 (19.5)
N	54.7 (49.8)	35.8 (32.6)	
N	55.2 (50.3)		38.0 (34.6)
S	54.0 (49.2)	33.3 (30.3)	
S	54.5 (49.6)		36.0 (32.8)
QT11	67.5 (61.5)	54.4 (49.5)	
QT11	50.2 (45.7)		>50.2 (>45.7)

Table 12. K_{scc} of WOL Specimens in 5M NaNO_3 at pH 6, 368°K.

Heat Treatment	Initial Stress Intensity $\text{MPa(m)}^{1/2}$ $(\text{ksi(in)}^{1/2})$	K_{scc} $\text{MPa(m)}^{1/2}$ $(\text{ksi(in)}^{1/2})$
HS	45.1 (41.1)	<37.8 (<34.4)
HR	39.6 (36.1)	24.8 (22.6)
HR	53.9 (49.0)	14.4 (13.1)
NS	43.6 (39.7)	29.4 (26.8)
NS	44.9 (40.9)	29.5 (26.9)
N	54.7 (49.8)	35.8 (32.6)
QS	45.1 (41.1)	29.6 (27.0)
QS	50.4 (45.9)	27.3 (24.9)
S	54.0 (49.2)	33.3 (30.3)
QT11	67.5 (61.5)	54.4 (49.5)

GLOSSARY OF TERMS AND ABBREVIATIONS*

austenite	high temperature, FCC (α) iron phase.
CT	compact tension; fracture specimen tested in constant load arrangement (ASTM E 399).
ferrite	low temperature, BCC (γ) iron phase.
IG	intergranular; fracture path along grain boundaries.
J	joule; SI unit of energy.
ksi	psi x 1000; English system unit of pressure or stress.
MPa	megapascal; SI unit of pressure or stress.
N	newton; SI unit of force.
platinized platinum	high surface area platinum deposit produced by electroplating (ASTM G 5).
SCC	stress corrosion cracking; definition on page 1.
SCE	saturated calomel electrode; voltage scale using zero volts for the saturated calomel electrode.
TG	transgranular; fracture path through individual metal grains.
WOL	wedge opening loaded; fracture specimen tested in constant crack opening displacement arrangement (Reference 131).

* Unless otherwise noted data is presented in the International System of Units, SI (ASTM E 360).

BIBLIOGRAPHY*

1. R. M. Girdler, USAEC Report DP-990, Savannah River Laboratory, Aiken, SC, December 1965.
2. U. S. News & World Report, 75(11): 30 (1973).
3. T. P. Hoar, Second International Congress on Metallic Corrosion, NACE, Houston, 1966, p. 14.
4. C. D. Beachem, Met. Trans., 3, 437 (1972).
5. J. C. Scully, "The Stress Corrosion Cracking of α -Titanium Alloys in Aqueous and Methanolic Environments," paper presented at the International Symposium on Stress Corrosion Mechanisms in Titanium Alloys, Georgia Institute of Technology, January 1971.
6. R. N. Parkins, Metallurgical Reviews, 9, 201 (1964).
7. T. W. Greene, A. A. Holzbauer, Welding J., Res. Suppl., 25(3): 171-S (1946).
8. M. L. Holzworth, R. M. Girdler, L. P. Costas, W. C. Rion, Materials Protection, 7, 36 (1968).
9. R. S. Ondrejcin, USAEC Report DP-1347, Savannah River Laboratory, Aiken, SC, August 1974.
10. J. H. Andrew, Trans. Faraday Soc., 9, 318 (1914).
11. S. W. Parr, Univ. Illinois Bull., 94 (1917).
12. R. N. Parkins, Chem. Ind., 180 (1953).
13. R. N. Parkins, R. Usher, First International Congress on Metallic Corrosion, Butterworths, London, 1962, p. 289.
14. W. P. Lees, Symposium on Internal Stresses in Metals, Inst. of Metals, London, 1948, p. 333.
15. U. R. Evans, Corrosion Technology, 1, 136 (1954).
16. H. M. Welton, Met. Progr., 52, 803 (1947).

* Abbreviations where possible are in accordance with Nuclear Science Abstracts and Metals Abstracts.

17. R. Weck, Inst. Gas Engineers Publication 517 (1947).
18. W. C. Schroeder, A. A. Berk, U. S. Dept. of Interior, Bureau of Mines Bull. 443, 1941.
19. A. W. Loginaw, E. H. Phelps, Corrosion, 18, 299t (1962).
20. R. E. Pollard, Symposium on SCC of Metals, ASTM-AIME, Phila., 1945, p. 437.
21. J. M. Sutcliffe, R. R. Fesseler, W. K. Boyd, R. N. Parkins, Corrosion, 28, 313 (1972).
22. R. W. Staehle, in Fundamental Aspects of Stress Corrosion Cracking, R. W. Staehle et al. eds., NACE, Houston, 1969, p. 3.
23. H. H. Uhlig, in Fundamental Aspects of Stress Corrosion Cracking, R. W. Staehle et al. eds., NACE, Houston, 1969, p. 86.
24. H. Mazille, H. H. Uhlig, Corrosion, 28, 427 (1972).
25. J. D. Gilchrist, R. Narayan, Corrosion Sci., 11, 281 (1971).
26. Z. Szklarska-Smialowska, Corrosion, 20, 198t (1964).
27. R. N. Parkins, in Stress Corrosion Cracking and Embrittlement, W. D. Robertson ed., Wiley, N. Y., 1956, p. 140.
28. D. Gherandi, et al., Second International Congress on Metallic Corrosion, NACE, Houston, 1966, p. 605.
29. M. Smialowski, T. Ostrowska, Corrosion et Anti-Corrosion, 5, 76 (1957).
30. E. Herzog, A. Portevin, Métaux et Corrosion, 24, 40 (1949).
31. M. Smialowski, First International Congress on Metallic Corrosion, Butterworths, London, 1962, p. 296.
32. R. N. Parkins, in Fundamental Aspects of Stress Corrosion Cracking, R. W. Staehle et al. eds., NACE, Houston, 1969, p. 361.
33. M. Smialowski, First International Congress on Metallic Corrosion, Butterworths, London, 1962, p. 295.
34. M. J. Humphries, R. N. Parkins, in Fundamental Aspects of Stress Corrosion Cracking, R. W. Staehle et al. eds., NACE, Houston, 1969, p. 384.

35. H. Grafen, Corrosion Sci., 7, 177 (1967).
36. M. Pourbaix, Atlas of Electrochemical Equilibria in Aqueous Solutions, Pergamon Press, NY, 1966.
37. J. Flis, Corrosion, 29, 37 (1973).
38. H. J. Engell, A. Bäumel, in Physical Metallurgy of Stress Corrosion Fracture, T. N. Rhodin ed., Interscience, NY, 1959, p. 341.
39. H. L. Logan, J. Res. Nat. Bur. Stand., 48, 99 (1952).
40. R. B. Mears, R. H. Brown, E. H. Dix, Jr., Symposium on Stress Corrosion Cracking of Metals, ASTM-AIME, Phila., 1945, p. 323.
41. H. L. Logan, in Physical Metallurgy of Stress Corrosion Fracture, T. N. Rhodin ed., Interscience, NY, 1959, p. 295.
42. C. G. Dunn, F. W. Daniels, M. J. Bolton, Trans. AIME, 188, 245 (1950).
43. J. Flis, M. Smialowski, J. Mieluch, Second International Congress on Metallic Corrosion, NACE, Houston, 1966, p. 925.
44. J. A. S. Green, R. N. Parkins, Corrosion, 24, 66 (1968).
45. E. H. Dix, Symposium on Stress Corrosion Cracking of Metals, ASTM-AIME, Phila., 1945, p. 1.
46. F. R. N. Nabarro, Symposium on Internal Stresses in Metals, Inst. of Metals, London, 1948, p. 61.
47. R. N. Parkins, Brit. Welding J., 2, 495 (1955).
48. R. N. Parkins, Brit. Welding J., 8, 24 (1961).
49. M. Henthorne, R. N. Parkins, Corrosion Sci., 6, 357 (1966).
50. W. Zabik, Third International Congress on Metallic Corrosion, Mir, Moscow, 1969, Vol. II, p. 319.
51. B. F. Brown, in Stress Corrosion Cracking in High Strength Steels and in Aluminum and Titanium Alloys, B. F. Brown ed., Naval Research Lab, Wash., DC, 1972, Chapt. 1.
52. R. N. Parkins, JISI, 172, 149 (1952).
53. W. Radeker, H. Grafen, Stahl Eisen, 76, 1616 (1956).

54. M. J. Humphries, R. N. Parkins, Fourth International Congress on Metallic Corrosion, NACE, Houston, 1972, p. 151.
55. M. Henthorne, R. N. Parkins, Brit. Corrosion J., 2, 186 (1967).
56. M. Henthorne, R. N. Parkins, Third International Congress on Metallic Corrosion, Mir, Moscow, 1969, Vol. II., p. 309.
57. J. Flis, J. C. Scully, Corrosion, 24, 326 (1968).
58. L. M. Long, H. H. Uhlig, J. Electrochem. Soc., 112, 964 (1965).
59. N. Von Franz, W. Werner, Stahl Eisen, 59, 1155 (1939) [AEC-tr-6394].
60. R. P. Elliott, Constitution of Binary Alloys, First Supplement, McGraw-Hill, NY, 1965.
61. G. Bombara, Corrosion Sci., 9, 519 (1959).
62. H. H. Uhlig, J. Sava, Trans. ASM, 56, 361 (1963).
63. H. Mazille, H. H. Uhlig, Corrosion, 28, 427 (1972).
64. L. M. Long, N. A. Lockington, Corrosion Sci., 11, 853 (1971).
65. J. Flis, Corrosion Sci., 10, 745 (1970).
66. J. T. Waber, H. J. McDonald, Stress Corrosion Cracking of Mild Steel, Corrosion Publ. Co., Pittsburgh, PA, 1947.
67. L. M. Long, H. H. Uhlig, J. Electrochem. Soc., 112, 964 (1965).
68. H. L. Logan, H. T. Yolken, Second International Congress on Metallic Corrosion, NACE, Houston, 1966, p. 109.
69. E. Houdrement, H. Bennek, H. Wentrup, Stahl Eisen, 60, 575 (1940).
70. R. Munster, H. Grafen, Arch. Eisenhüttenwesen, 36, 277 (1965).
71. C. E. Pearson, R. N. Parkins, Welding Research, 3, 95r (1949).
72. R. N. Parkins, A. Brown, JISI, 193, 45 (1959).
73. E. G. Coleman, D. Weinstein, W. Rostoker, Acta Met., 9, 491 (1961).
74. A. A. Berk, W. F. Waldeck, Chem. Eng., 57, 235 (1950).

75. F. P. A. Robinson, L. G. Nel, Second International Congress on Metallic Corrosion, NACE, Houston, 1966, p. 172.
76. J. E. Reinoehl, W. E. Berry, Corrosion, 28, 151 (1972).
77. S. W. Parr, F. G. Straub, Univ. Illinois E. E. S. Bull. No. 177, 67 (1928).
78. H. Grafen, D. Kuron, Arch. Eisenhüttenwesen, 36, 285 (1965).
79. W. C. Schroeder, A. A. Berk, R. A. O'Brien, Metals & Alloys, 8, 320 (1937).
80. C. D. Weir, P. Hamer, Chem. Ind., 1040 (1952).
81. W. C. Schroeder, A. A. Berk, A. A. O'Brien, Trans. ASME, 60, 35 (1938).
82. C. D. Weir, Trans. ASME, 70, 253 (1948).
83. M. J. Humphries, R. N. Parkins, Corrosion Sci., 7, 747 (1967).
84. K. Bohnenkamp, E. Rieke, Third International Congress on Metallic Corrosion, Mir, Moscow, 1969, Vol. II, p. 333.
85. J. E. D. Mayne, J. W. Menter, M. J. Pryor, J. Chem. Soc., 3229 (1950).
86. I. N. Sherstobitova, D. I. Leikis, B. N. Kabanov, Soviet Electrochem., 5, 241 (1969).
87. K. Bohnenkamp, in Fundamental Aspects of Stress Corrosion Cracking, R. W. Staehle et al. eds., NACE, Houston, 1969, p. 374.
88. H. A. McCarthy, P. L. Harrison, Corrosion Sci., 14, 469 (1974).
89. F. H. Keating, Symposium on Internal Stresses in Metals, Institute of Metals, London, 1948, p. 311.
90. N. A. Nielson, in The Physical Metallurgy of Stress Corrosion Fracture, T. N. Rhodin ed., Interscience, NY, 1959, p. 121.
91. H. W. Pickering, F. H. Beck, M. G. Fontana, Corrosion, 18, 23t (1962).
92. E. H. Dix, Trans. AIME, 137, 11 (1940).
93. H. W. Pickering, P. R. Swann, Corrosion, 19, 373t (1963).
94. A. J. Forty, P. Humble, Phil. Mag., 8, 247 (1963).

95. A. J. McEvily, A. P. Bond, J. Electrochem. Soc., 112, 131 (1965).
96. P. R. Swann, J. Nutting, J. Inst. Metals, 88, 478 (1959-60).
97. D. Tromans, J. Nutting, Corrosion, 21, 143 (1965).
98. T. P. Hoar, J. G. Hines, JISI, 182, 124 (1956).
99. T. P. Hoar, J. M. West, Proc. Roy. Soc. (London), A268, 304 (1962).
100. H. H. Uhlig, in The Physical Metallurgy of Stress Corrosion Fracture, T. N. Rhodin ed., Interscience, NY, 1959, p. 1.
101. C. A. Zapffe, Materials and Methods, 32, 58 (1950).
102. C. A. Zapffe, C. Sims, Trans. Met. Soc. AIME, 145, 225 (1941).
103. A. S. Tetelman, W. D. Robertson, Trans. Met. Soc. AIME, 224, 775 (1962).
104. N. J. Petch, P. Staples, Nature, 169, 842 (1952).
105. J. G. Morlet, H. H. Johnson, A. R. Troiano, Trans. Met. Soc. AIME, 212, 528 (1958).
106. D. G. Westlake, Trans. ASM, 62, 1000 (1969).
107. D. A. Vaughan, D. I. Phalen, C. L. Peterson, W. K. Boyd, Corrosion, 19, 315t (1963).
108. H. G. Vaughan, M. E. DeMorton, JISI, 182, 389 (1956).
109. G. Wranglen, in Localized Corrosion, R. W. Staehle et al. eds., NACE, Houston, 1974, p. 462.
110. W. R. Middleton, Brit. Corrosion J., 8, 62 (1973).
111. G. Sandoz, in Stress Corrosion Cracking in High Strength Steels and In Aluminum and Titanium Alloys, B. F. Brown ed., Naval Research Lab, Wash., DC, 1972, Chapt. 3.
112. J. G. Parker, M. A. Sadler, Corrosion Sci., 15, 57 (1975).
113. J. Flis, Brit. Corrosion J., 3, 182 (1968).
114. F. H. Cocks, J. Bradspies, Corrosion, 28, 192 (1972).
115. G. Sandoz, C. T. Fujii, B. F. Brown, Corrosion Sci., 10, 839 (1970).

116. H. W. Pickering, R. P. Frankenthal, in Localized Corrosion, R. W. Staehle et al. eds., NACE, Houston, 1974, p. 261.
117. P. Coterill, in Progress in Materials Science, Vol. 9, B. Chalmers ed., Pergamon Press, Oxford, 1961, p. 201.
118. R. A. Oriani, in Fundamental Aspects of Stress Corrosion Cracking, R. W. Staehle et al. eds., NACE, Houston, 1969, p. 32.
119. J. P. Fidelle, M. Rapin eds., L'Hydrogène Dans Les Métaux, Proceedings of Colloquium, Centre d'Etudes de Bruyères-le-Châtel, Valduc, 1967.
120. P. G. Bastien ed., L'Hydrogène Dans Les Métaux, Proceedings of Colloquium, Editions Science et Industrie, Paris, 1972.
121. J. Mieluch, M. Smialowski, Corrosion Sci., 4, 237 (1964).
122. M. Hansen, Constitution of Binary Alloys, McGraw-Hill, NY, 1958.
123. H. Uhlig, K. E. Perumal, M. Talerman, Corrosion, 30, 229 (1974).
124. V. Ashworth, P. J. Boden, Corrosion Sci., 10, 343 (1970).
125. J. Kruger, in Localized Corrosion, R. W. Staehle, et al. eds., NACE, Houston, 1974, p. 1.
126. B. G. Ateya, H. W. Pickering, in Hydrogen in Metals, I. M. Bernstein, A. W. Thompson eds., ASM, Metals Park, OH, 1974, p. 207.
127. M. R. Louthan, Jr., in Hydrogen in Metals, I. M. Bernstein, A. W. Thompson eds., ASM, Metals Park, OH, 1974, p. 53.
128. T. P. Hoar, J. R. Galvele, Corrosion Sci., 10, 211 (1970).
129. ASTM Standard A 516, ASTM Annual Book of Standards, Part 4, ASTM, Philadelphia, 1975.
130. ASTM Standard E 399, ASTM Annual Book of Standards, Part 10, ASTM, Philadelphia, 1975.
131. S. R. Novak, S. T. Rolfe, Journal of Materials, 4, 701 (1969).
132. J. P. Hickerson, USAEC Report SLA-73-0424, Sandia Laboratories, Albuquerque, NM, 1973, p. 62-117.
133. E. W. Baumann, Anal. Chim. Acta, 64, 284 (1973).
134. ASTM Standard G 5, Annual Book of ASTM Standards, Part 10, ASTM, Philadelphia, 1975.

135. N. D. Greene, Experimental Electrode Kinetics, Rensselaer Polytechnic Institute, Troy, NY, 1965.
136. ASTM Standard G 3, Annual Book of ASTM Standards, Part 10, ASTM Philadelphia, 1975.
137. E. O. Hall, Yield Point Phenomenon in Metals and Alloys, Plenum Press, NY, 1970.
138. C. W. Richards, Engineering Materials Science, Wadsworth Pub. Co., Belmont, CA, 1961, p. 109-111.
139. Z. D. Jastrzebski, Nature and Properties of Engineering Materials, Wiley & Sons, NY, 1959, Chapt. 4.
140. R. S. Ondrejcin, Savannah River Laboratory, unpublished results.
141. M. A. Streicher, Corrosion, 28, 143 (1972).
142. B. D. Cullity, Elements of X-Ray Diffraction, Addison-Wesley, Reading, MA, 1956, Chapt. 3.
143. V. Weiss, S. Yukawa, ASTM Special Technical Publication No. 381, ASTM, Philadelphia, 1965, p. 13-14.
144. J. M. West, Metal Sci. J., 7, 169 (1973).
145. E. C. Potter, G. M. W. Mann, First International Congress on Metallic Corrosion, Butterworths, London, 1962, p. 417.
146. A. B. Carlson, in Decontamination of Nuclear Reactors and Equipment, J. A. Ayres, ed., Ronald Press, NY, 1970, Chapt. 4.
147. U. R. Evans, The Corrosion and Oxidation of Metals, Arnold, London, 1960, p. 145.
148. I. M. Bernstein, A. W. Thompson, Carnegie-Mellon University Report 036-099-3, Carnegie-Mellon University, Pittsburgh, November 1974.
149. T. Toh, W. M. Baldwin, Jr., in Stress Corrosion Cracking and Embrittlement, W. D. Robertson ed., Wiley, NY, 1956, p. 176.
150. E. Eichen, K. R. Kinsman, J. Tabock, Proc. Fifth International Conference on Electron Microprobe Analysis, NY, July 22-24, 1970.
151. D. McLean, Grain Boundaries in Metals, Clarendon Press, Oxford, 1957, Chapt. 5.
152. B. J. Alexander, R. T. Foley, Corrosion, 31, 148 (1975).

153. H. H. Johnson, in Fundamental Aspects of Stress Corrosion Cracking, R. W. Staehle et al. eds., NACE, Houston, 1969, p. 439.
154. M. V. Hyatt, M. O. Speidel, in Stress Corrosion Cracking in High Strength Steels and in Aluminum and Titanium Alloys, B. F. Brown ed., Naval Research Lab, Washington, DC, 1972, Chapt. 4.
155. M. O. Speidel, L'Hydrogène Dans Les Métaux, Proceedings of Colloquium, P. G. Bastien ed., Editions Science et Industrie, Paris, 1972, p. 358.
156. B. C. Syrett, L. P. Trudeau, Corrosion, 27, 217 (1971).
157. J. R. Ambrose, J. Kruger, Corrosion, 28, 30 (1972).
158. A. M. Shams El Din, M. Y. Fakhr, Corrosion Sci., 14, 635 (1974).
159. D. M. Brasher, Brit. Corrosion J., 4, 122 (1969).
160. M. Pourbaix, Thermodynamics of Dilute Aqueous Solutions, Arnold, London, 1949, Section VI.D.
161. U. R. Evans, op. cit., p. 324-330.
162. H. R. Baker, C. R. Singletary, Corrosion, 28, 385 (1972).
163. S. Matsuda, H. H. Uhlig, J. Electrochem. Soc., 111, 156 (1964).
164. R. A. Legault, S. Mori, H. P. Leckie, Corrosion, 26, 121 (1970).
165. A. L. Bacarella, A. L. Sutton, J. Electrochem. Soc., 122, 11 (1975).
166. G. Faïta, F. Mazza, G. Bianchi, in Localized Corrosion, R. W. Staehle et al. eds., NACE, Houston, 1974, p. 34.
167. L. G. Sillén, A. E. Martell eds., Stability Constants of Metal-Ion Complexes, The Chemical Society, London, 1964.
168. T. Misawa, K. Asami, K. Hashimoto, S. Shimodaira, Corrosion Sci., 14, 279 (1974).
169. G. R. Wallwork, B. Harris, in Localized Corrosion, R. W. Staehle et al. eds., NACE, Houston, 1974, p. 292.
170. C. F. Barth, E. A. Steigerwald, A. R. Troiano, Corrosion, 25, 353 (1969).
171. M. Schorr, J. Yalom, Corrosion Sci., 12, 867 (1972).

VITA

Peter Gregory Sarafian was born on November 12, 1942 in Albany, N.Y. He is the son of Ms. Margo Sarafian of Coral Gables, Florida. He graduated from Duke University (BS - Chemistry, 1964) and Georgia Institute of Technology (MS - Nuclear Engineering, 1970). He is a former submarine officer in the Naval Nuclear Propulsion Program and has two children by a former marriage: Andrea Marie Sarafian and Andrew Theodore Sarafian.